This is to certify that the
dissertation entitled

POLYCRYSTALLINE DIAMOND THIN-FILM FABRY-PEROT
OPTICAL RESONATORS ON SILICON

presented by

Roger Allen Booth, Jr.

has been accepted towards fulfillment
of the requirements for the

Ph.D. Electrical Engineering

Donnie K Reinhard
Major Professor's Signature

December 12, 2003
Date

DATE DUE	DATE DUE	DATE DUE
MAY 16 2006		
092209		

POLYCRYSTALLINE DIAMOND THIN-FILM FABRY-PEROT OPTICAL RESONATORS ON SILICON

By

Roger Allen Booth, Jr.

A DISSERTATION

Submitted to
Michigan State University
in partial fulfillment of the requirements
for the degree of

DOCTOR OF PHILOSOPHY

Department of Electrical and Computer Engineering

2003

ABSTRACT

POLYCRYSTALLINE DIAMOND THIN-FILM FABRY-PEROT OPTICAL RESONATORS ON SILICON

By

Roger Allen Booth, Jr.

Micro-optical devices have applications ranging from gas detection to optical computing. Michigan State University has the capability to deposit high optical quality diamond thin films on silicon substrates using microwave cavity plasma reactors. Diamond is of interest for optical applications due to its high index of refraction and wide spectral transmission range. Combining polycrystalline diamond thin film deposition techniques and MEMS fabrication techniques, an array of optical wavelength Fabry-Perot resonators on a silicon wafer has been constructed and accurately modeled.

This thesis describes the first fabrication of diamond thin-film Fabry-Perot resonators on silicon wafers. Standard fabrication techniques are employed, including thermal oxidation, photolithography, PECVD diamond deposition, anisotropic wet etching, and sputtering. The optical performance of the resonators is investigated by measuring the through-transmission of the device as a function of wavelength. Performance is correlated with the physical properties of the device, including surface roughness.

Tran

of in

the t

film

valu

Atom

The f

skew

simu

distr

Transmission of the device is simulated with multi-layer optics theory. A novel method of incorporating surface roughness into standard multi-layer optics theory is developed in the thesis, and applied to the resonators considering the surface roughness of the diamond film to be modeled by Gaussian and non-Gaussian distributions. The models provide valuable guidance into the design of the resonators.

Atomic Force Microscopy is employed to characterize the surface roughness of the films. The films are found to be approximately Gaussian, but with non-negligible amounts of skewness and kurtosis measured. A Pearson Type-IV distribution is used in the optical simulation to represent non-Gaussian roughness in the diamond film. Use of this distribution improves the fit between theory and experimental measurements.

To my parents and my wife.

ACKNOWLEDGEMENTS

I would like to acknowledge my committee members: Dr. Reinhard, Dr. Hogan, Dr. Grotjohn, Dr. Golding and Dr. Birge. Special thanks is due to Dr. Reinhard for guiding me through this research and being a patient and excellent teacher.

TABLE OF CONTENTS

LIST OF TABLES

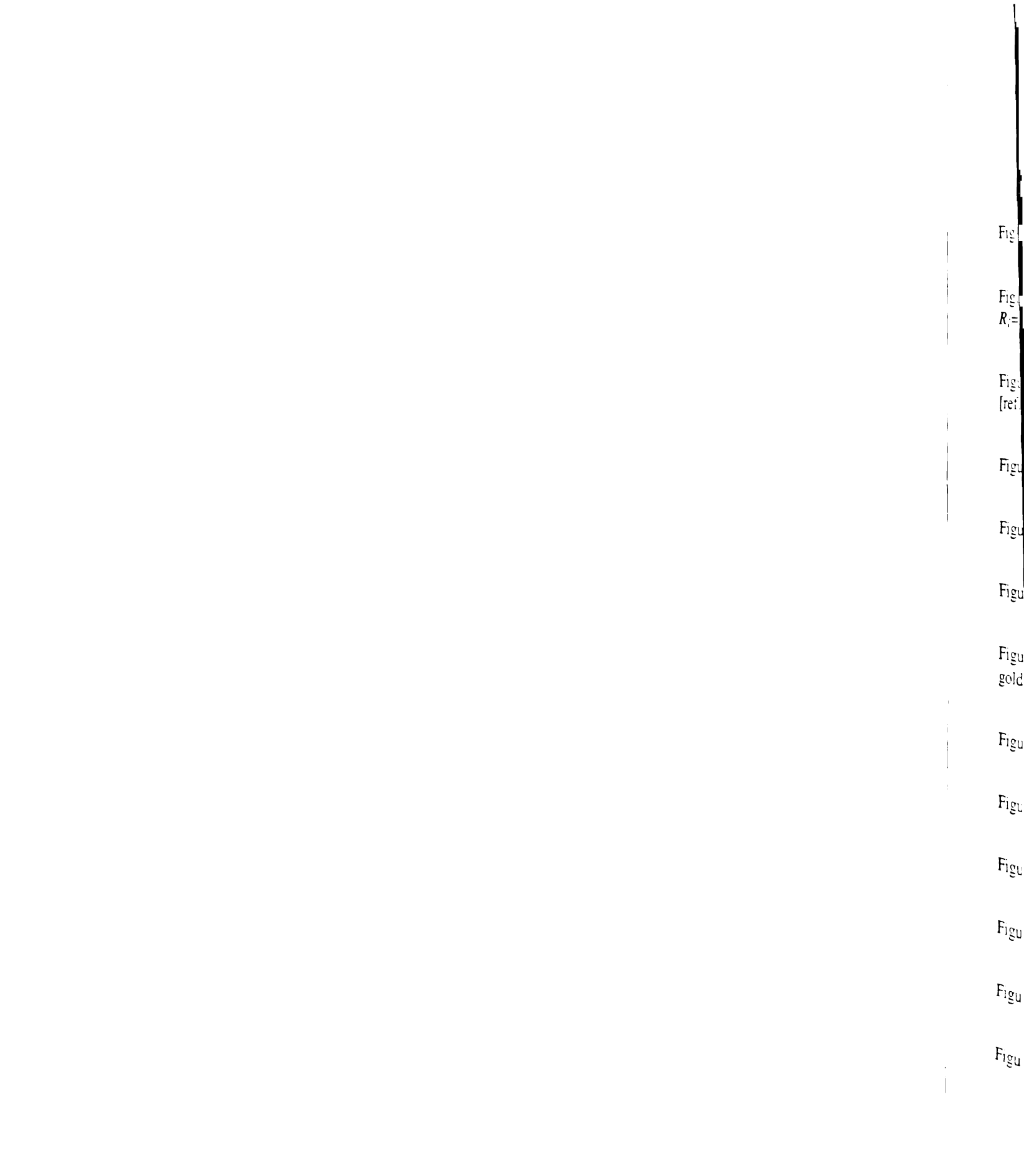

LIST OF FIGURES

Fig

Fig
Co
po

Fig

Fig

Fig
Th

Fig
1, b

Fig
RB

Figu
RB

Figu
RB

Figu
RB

Figur
RB

Figur
RB

Figur

Fi

Fi

Fi

Fi

Fig

Fig

Figu

Figu

Figu

Fig
[6.6

Fig
Typ

Fig
inc

Fig
rou

Fig
dis

Chapter 1: Introduction

1.1 Introduction and Motivation

This thesis is written on the subject of a polycrystalline diamond optical device, integrated onto a silicon wafer using microfabrication techniques. It describes and reports on the fabrication of diamond Fabry-Perot resonators on silicon, and uses multilayer optics theory to model the optical performance of the device with respect to the physical parameters of the device.

The general area of on-chip optics is of interest for a variety of applications. From simple optical detectors to full-scale optical interconnects for devices, on-chip optics is a broad area promising many applications and continued research interest. Because of the semiconductor process engineer's general affinity for applying thin films to silicon and other semiconductor substrates, the area of multi-layer thin-film optics seems almost a natural partner for on-chip optics. Indeed, this is the case for the devices constructed in this research.

Diamond is of particular interest for optical applications because of its uniquely broad window of transmission in the electromagnetic spectrum. Moreover, except for high temperatures in oxygen rich atmospheres, it may be used in a variety of hostile environments. A contribution of this research is the integration of diamond optical

devices, specifically Fabry-Perot resonators, onto a silicon wafer. This is accomplished by combining MEMS fabrication technology with diamond deposition techniques.

1.2 Objectives

The first objective of this work is to establish a repeatable fabrication procedure for the optical resonators. Secondly, a method of optically characterizing the samples shall be established.

Next, a mathematical model of the optical performance of the device must be constructed. This model is to be based on physically measureable properties of the device. Finally, the mathematical simulation should be capable of guiding the future direction of this work.

1.3 Preview of the Thesis

Chapter 2 presents a review of background material relevant to two main parts of this thesis, the optical properties of the diamond film used in the device, and the modeling of the optical performance of the device. The optical properties of diamond are discussed briefly, mainly relating to the polycrystalline diamond films used in this research. The modeling material includes sections on ideal Fabry-Perot resonators, two sections on multi-layer optics theory, and a discussion of surface roughness and its impact on a single interface with respect to optical reflection and transmission at that interface.

Chapter 3 presents a detailed explanation of the experimental procedures used for this work, including the device fabrication and characterization. The fabrication of the device uses some MEMS style fabrication sequences to create thin, free-standing diamond windows on the silicon wafer. These windows form the basis of the Fabry-Perot resonators investigated in this research. The device is characterized optically by passing light through the diamond windows and observing the transmission characteristics of the film. Chapter 3 discusses how these measurements are performed. Additional characterization techniques are employed, namely SEM and AFM to evaluate the properties of the diamond film depositions. These techniques are also briefly introduced.

Chapter 4 presents the model developed for this work, and explains a numerical implementation of the model used extensively in this thesis. The model combines the multi-layer optics theory and the surface roughness modeling presented in Chapter 2. This allows improved modeling of the optical transmission of the device.

Chapter 5 compares optical transmission measurements to simulations based on the model presented in Chapter 4. The measurements and simulations in Chapter 5 show good correspondence, but lead to some conclusions not expected at the outset of this research.

Chapter 6 takes a detailed look at surface roughness of the diamond films grown for this work, and investigates their deviation from the Gaussian distribution used in Chapters 4

and 5, and discusses how this deviation impacts the simulation. It is found that the inclusion of a more sophisticated distribution can improve the performance of the model.

Chapter 7 outlines the conclusions drawn in the preceding chapters, and discusses some possible future directions for this work.

Chapter 2: Background Fundamentals

2.1 Introduction

This chapter presents background material that is essential to various aspects of the research performed in this dissertation. First, the operating principles of Fabry-Perot resonators are described, as well as several performance measures of resonators. Examples of previous investigations of on-chip Fabry-Perot resonators are described. Next, the optical properties of diamond are reviewed, particularly in the context of thin film polycrystalline diamond formed by chemical vapor deposition (CVD). The optical structures in this research are analyzed by a matrix method, and the background mathematical formulation of this method is described, beginning with Maxwell's equations. Finally, the effects of a rough surface on reflection and transmission are reviewed, primarily in the context of a superposition of plane waves and for normal incidence.

2.2 Fabry-Perot Resonators

The Fabry-Perot resonant cavity is an important device for a variety of optical and microwave applications, including highly selective band-pass filters. As shown in Figure 2.1, an ideal optical Fabry-Perot cavity consists of a non-absorbing optical medium with partially reflective, non-absorbing mirrors on either side with perfectly smooth interfaces

be

tr

El

ex

of

wa

cal

wh

ref

der

tran

between the optical medium and the mirrors. The ideal cavity will allow up to 100% transmission of certain wavelengths of light, while heavily attenuating other wavelengths.

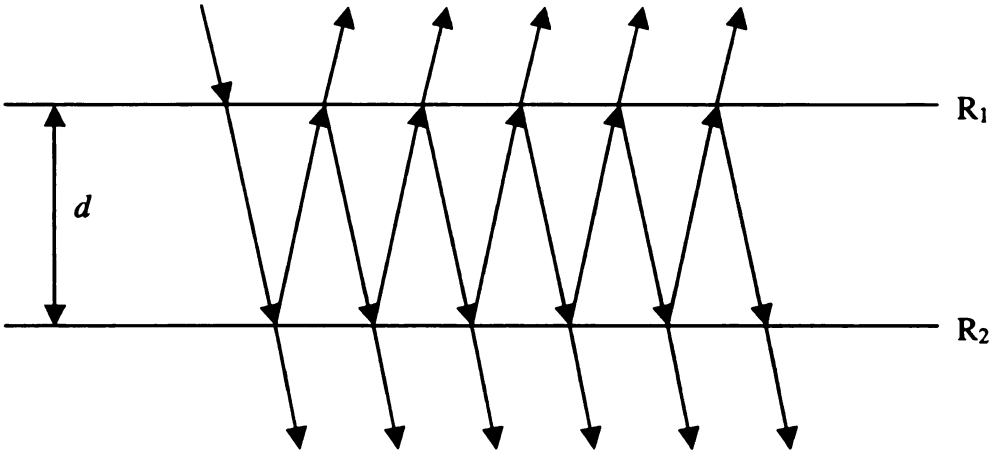

Figure 2.1 Diagram of an ideal Fabry-Perot resonator

Elaboration on the following review of the Fabry-Perot resonator can be found for example in Verdeyor[1]. Resonance of the cavity occurs when there is an integral number of half-wavelengths between the two mirrors. This resonance corresponds to the wavelength of peak transmission. The transmission of a Fabry-Perot resonator can be calculated as a function of the freespace wavelength, λ_0, to be:

$$T = \frac{(1-R_1)\cdot(1-R_2)}{\left(1-\sqrt{R_1R_2}\right)^2 + 4\sqrt{R_1R_2}\sin^2\left(\frac{2\pi dn}{\lambda_0}\right)} \qquad [2.1]$$

where n is the refractive index of the optical medium, R_1 and R_2 are the power reflectivities of the lossless mirrors and d is the distance between the mirrors. The derivation of an equation equivalent to [2.1] is shown in Chapter 4. The maximum transmission as a function of the mirror reflectivities is given by:

$$T_{\max} = \frac{(1-R_1)\cdot(1-R_2)}{\left(1-\sqrt{R_1 R_2}\right)^2} \qquad [2.2]$$

Therefore when R_1 and R_2 are equal, the cavity will transmit 100% of the incident power at the resonant wavelengths, λ_m, where

$$d = m\frac{\lambda_m}{2} \qquad [2.3]$$

and m is an integer which identifies the resonant mode. In equation [2.3], the wavelength, λ_m, refers to the wavelength in the optical medium, i.e. the free space wavelength divided by n. Figure 2.2 shows the result of equation [2.1] plotted for R_1=R_2=0.9, d=1μm and air (n=1) as the medium between the mirrors.

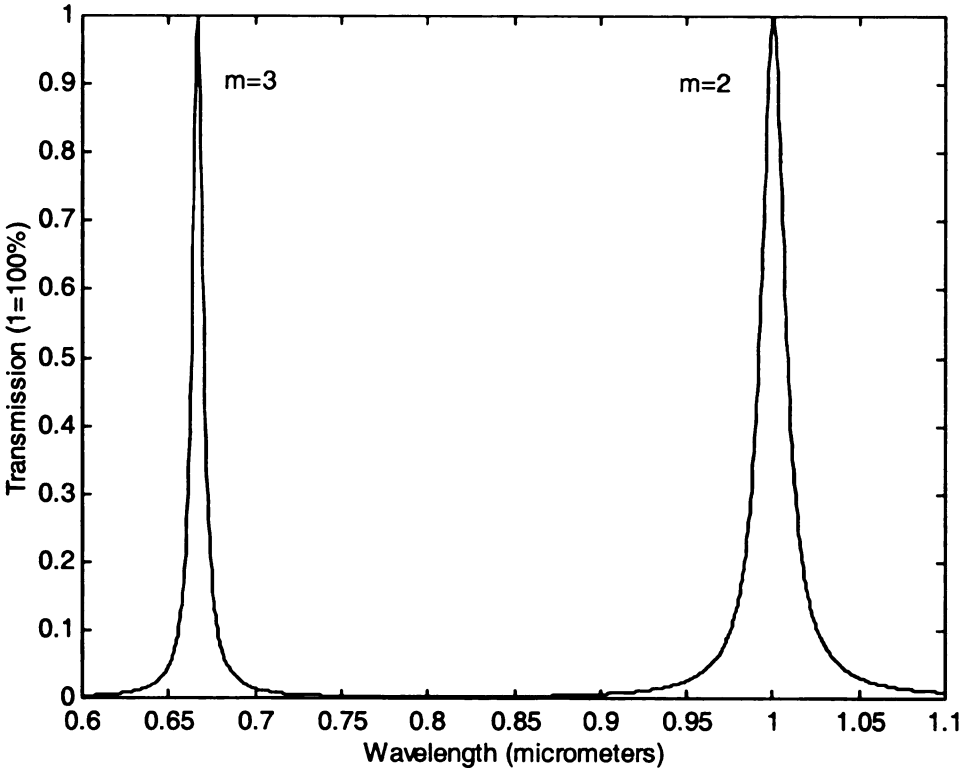

Figure 2.2 Transmission of an ideal Fabry-Perot resonator with n=1, d=1μm, and R_1=R_2=0.9

There are several useful figures of merit for Fabry-Perot resonators. One is the *quality factor*, Q, which is related to the sharpness of the transmission peaks by:

$$Q = \frac{\nu_m}{\Delta \nu_m} \qquad [2.4]$$

where ν_m is the resonance frequency of the m^{th} mode and $\Delta\nu_m$ is the spectral width, or full width at half maximum of the peak at ν_m.

Using equation [2.1], Q can be expressed in an analytical form as a function of cavity parameters and resonance wavelength as:

$$Q = \frac{2\pi d}{\lambda_m} \frac{(R_1 R_2)^{\frac{1}{4}}}{1-(R_1 R_2)^{\frac{1}{2}}} \qquad [2.5]$$

The *photon lifetime* inside the cavity, τ_p, is the time for a round trip divided by the fraction of photons lost to the cavity per round trip. It is related to Q by:

$$\tau_p = \frac{Q}{\omega_m} \qquad [2.6]$$

where ω_m is the angular frequency of the peak of m^{th} mode. τ_p for an ideal cavity can be expressed in terms of cavity parameters by:

$$\tau_p = \frac{2nd/c}{1-R_1 R_2} \qquad [2.7]$$

where the numerator of this expression is the time it takes a photon to make a round trip in the cavity, and the denominator is the fraction of photons lost per round trip. Other loss mechanisms in a non-ideal cavity would lead to an expression of the form:

$$\tau_p = \frac{2nd/c}{1-R_1 R_2 + (\text{other losses})} \qquad [2.8]$$

Another measure of resonator performance is the separation between neighboring resonant peaks. It is known as the *free spectral range* and is expressed as:

$$\nu_f = \frac{c/n}{2d} \qquad [2.9]$$

Finally, the *finesse* is defined as the ratio of the free spectral range to the *spectral width*, which can also be related to Q:

$$F = \frac{\nu_f}{\Delta\nu_m} = \frac{\pi(R_1 R_2)^{\frac{1}{4}}}{1-\sqrt{R_1 R_2}} = \frac{\lambda_0}{2nd} Q \qquad [2.10]$$

For the ideal cavity illustrated in Figure 2, the free spectral range is equal to $1.5*10^{14}$ Hz and the spectral width of the m=2 mode is approximately $5*10^{12}$ Hz. By equation [2.10], this corresponds to a finesse of 30 for this peak. Using equation [2.5], Q is approximately 60 for the same peak.

As discussed at the beginning of this section, Fabry-Perot resonators form wavelength-selective band-pass filters. Such a filter in and of itself can be useful in certain applications, such as detecting an optical signal broadcast at a certain wavelength. In this case, the resonator would serve to filter out other wavelengths, so that only the wavelength carrying the signal would reach the detector. Another interesting application is an array of resonators on the same substrate, each tuned to a different wavelength, such that an on-chip spectrometer could be formed. Such a device could be used, for example, to investigate the chemical composition of a gas based on the optical wavelengths absorbed and transmitted through the gas. Another application of an on-chip Fabry-Perot resonator is a pressure transducer[2].

Ahmadi[3] *et al* have reported on integrating Fabry-Perot resonators onto semiconductor substrates, using CMOS and MEMS technology. Booth[4] *et al* have reported on the first diamond film Fabry-Perot resonator using standard Plasma-Enhanced CVD and MEMS processes.

Correia[5,6,7] *et al*, and Bartek[8,9] *et al* have reported on constructing an array of 16 Fabry-Perot resonators and have produced working on-chip spectrometers. Their devices use

S
n
I
a
h
c

In
d
n

2.

W
re
ex
go
w
sp
Di
be
sp

SiO_2 as the medium between the mirrors. Partially transparent silver is used to form the mirror coatings. The results achieved are good with reported measured finesse values of 12, although surface roughness of the oxide film can become an issue with this technique, as simulations give finesse values of 40 for ideal structures. Additionally, if the distance between the reflective surfaces of the Fabry-Perot resonator can be adjusted, the cavity can be tuned. Several groups[10,11,12,13] are using MEMS technology to achieve this.

In addition to using Fabry-Perot resonators to create a spectrometer, it is possible to use a diffraction grating to separate an optical signal into its constituent wavelengths. This will not be discussed here, but it will be noted that some groups are working on this[14].

2.3 Optical Properties of Diamond

When constructing an optical resonator, absorption in the optical medium between reflectors can affect resonator performance as implied by the previous section 2.1. For example, SiO_2, which absorbs heavily in portions of the infrared (IR), would not be a good Fabry-Perot medium if the device were needed to operate over a wide span of IR wavelengths. Likewise, silicon would not work well in the visible portion of the spectrum, due to its small band gap and accompanying absorption of visible light. Diamond is a particularly attractive material for broad-based Fabry-Perot applications, because it is transparent from the ultra violet (UV) into the microwave portion of the spectrum with very slight absorption in the IR.

Diamond is considered to have the widest optical spectral transmission range of any known solid material[15]. Figure 2.3, from Harris, shows the optical transmission of single crystalline diamond plotted with the transmission of high quality CVD diamond. This spectral range can ideally span from around the band gap energy of 5.47eV to the mm portion of the electromagnetic spectrum.

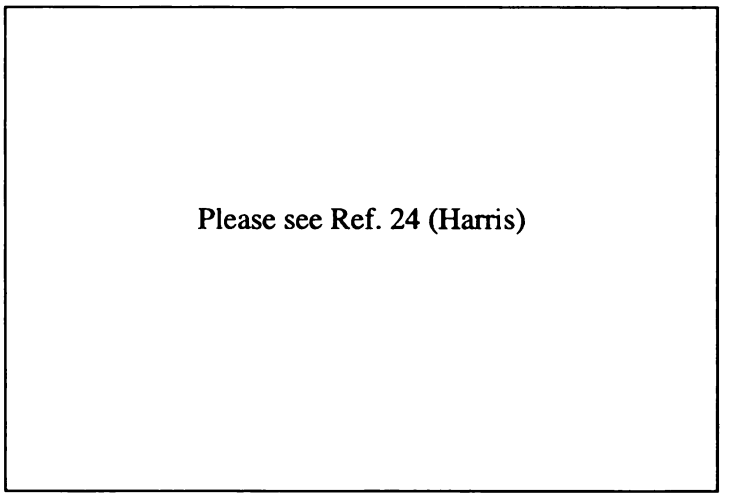

Figure 2.1 Optical transmission of Single Crystalline Diamond and CVD optical diamond [ref. 24]

Some sub-bandgap absorption can be seen in high quality diamond. This is due in part to the Urbach rule[16] which models a temperature-dependent exponential increase in absorption near the bandgap. Additional absorption is seen near the bandgap, which follows a temperature-independent relationship to about 0.35 μm[17].

Excitation of vibrational modes in carbon-to-carbon bonds leads to weak absorption of wavelengths in the mid-infrared[18]. Since pure diamond is a symmetric covalent material, it does not posses a dipole moment, which would lead to single phonon absorption in the

IR regime. Multi-phonon processes cause weak absorption between 2.5 and 7.5μm. The largest multi-phonon absorption peak magnitude is about 12 cm^{-1}, which occurs at about 5μm.

This research primarily studies the region of the spectrum between 700nm and 1600nm. For this spectral range, high optical quality CVD diamond should show virtually no optical absorption.

For this research, the index of refraction for diamond as a function of wavelength is modeled by the commonly used Sellmeier equation for diamond[19]:

$$n_d(\lambda) = \sqrt{\frac{4.3356 \cdot \lambda^2}{\lambda^2 - (0.1060)^2} + \frac{0.3306 \cdot \lambda^2}{\lambda^2 - (0.1750)^2} + 1} \qquad [2.11]$$

where λ is in units of micrometers. This empirical equation is valid over the range of wavelengths studied in this research, as well as much more of the electromagnetic spectrum.

Like any crystalline material, imperfections in diamond's crystal structure can influence the optical properties exhibited by a particular sample[20]. The most common defects found in natural diamond are the presence of nitrogen, and to a lesser extent, boron[18]. The presence of nitrogen typically leads to absorption of higher photon energies. Such absorption typically leads to a yellow or brown appearance of the diamond. Boron, which occurs less commonly than nitrogen in natural diamond, leads to IR absorption that can extend into the longer wavelengths of the visible spectrum. Absorption at the longer

visible wavelengths leads to a blue appearance. Also, if the incorporation of nitrogen or boron into the crystal breaks the lattice symmetry, single phonon absorption in the infrared may occur[21].

The diamond used in this research is polycrystalline diamond deposited on a substrate by plasma enhanced chemical vapor deposition (CVD). For modeling purposes, though, the diamond film is treated as a continuous slab of diamond, i.e. grain boundary effects within the diamond are not explicitly considered. For the films in this study, the excellent match of empirical data to theoretical calculations can be argued to justify such an assumption.

It should be noted, however, that not all diamond produced by CVD techniques is of high optical quality. The CVD technique itself may introduce chemical impurities, surface roughness, non-diamond bonds between carbon atoms, and grain boundaries that would not be present in pure, ideal diamond. Each of these may cause characteristics in the optical properties of the CVD diamond that would not be present in ideal diamond[18].

CVD may lead to the presence of nitrogen or boron as can be found in natural diamond, but an additional concern with CVD diamond is the presence of hydrogen and oxygen. Hydrogen and oxygen can often be found in the feed gases used in the CVD process, and as such, may be incorporated into the film during growth. Hydrogen in the diamond lattice often allows additional phonon modes, centered around 3.5μm. Oxygen is sometimes added to CVD feed gasses to improve the properties of the diamond at visible

wavelengths by reducing the number of non-diamond carbon to carbon bonds. Oxygen incorporated into the film, though, will lead to increased absorption in the IR[18].

Carbon-to-carbon bonds in diamond are referred to as sp^3 bonds. Depending on CVD growth conditions, varying amounts of non-sp^3 bonds can be introduced into the lattice. This can lead to sub-bandgap absorption in the visible range[22,23].

Typically, producing films of high optical quality means that process parameters are such that growth rate will be relatively low[24]. High growth rate conditions often lead to various defects in the resultant diamond as described above. Additionally, as-grown surface roughness of CVD films can vary greatly. Surface roughness can lead to great reductions in the optical performance of a film[25,26,27]. However, polished slabs of CVD polycrystalline diamond[24] can demonstrate optical properties quite close to the best single crystal diamond from the UV, through the visible, and into the IR and microwave.

2.4 Modeling of Multi-Layer Optical Structures

The theoretical calculations in this research require the treatment of multilayered optical structures. For many years, the n-layer problem in optics was considered to be intractable, much like the n-body problem in mechanics. In 1937, however, Rouard showed a method for closed form matrix solution in which multilayer structures can be analyzed by representing each layer by a 2 x 2 matrix[28,29,30,31,32]. This method has become essential to the analysis of multilayer thin film optics. Subsequent treatments

H
t
r

T
re
ta
c
c
m
th
o

E
li
n
n
ca
Th

2.4

Th
of

have resulted in different, but equivalent, formulations of this method. Two distinct formulations have been used in the analysis of results in this research, and are described in the following sections.

The first formulation shall be referred to here as the MacLeod technique, after the reference most often cited in the literature when referring to this technique[31]. The second technique, commonly called the transfer matrix, uses matrices containing the Fresnel coefficients and phase propagation across the layer. This nomenclature is only partially consistent with the literature, as MacLeod's method is sometimes called a 'transfer matrix' method as well. However, the two methods are distinct enough that inspection of the equations presented should readily identify which technique is being used, regardless of the particular nomenclature chosen by the author.

Each of the techniques presented relies upon a superposition of plane waves, and thus linearity of the optical medium is assumed. Additionally, this research will also assume normal incidence of the light onto the optical structure. Although the models can treat non-normal incidence, the assumption of normal incidence simplifies the derivations and calculations to some extent and is an accurate representation of the experimental set-up. The reader is referred to the cited references for the case of non-normal incidence.

2.4.1 MacLeod method

The development of MacLeod's approach begins with Maxwell's equations, which are often expressed in Gaussian units for work with thin film optics[33,34]. Gaussian units will

be briefly discussed here. The velocity with which light propagates in free space is taken to be:

$$c = \frac{1}{\sqrt{\mu_0 \varepsilon_0}} \qquad [2.12]$$

In the MKS system of units, μ_0 is chosen as $4\pi * 10^{-7}$ Henries/meter. However, in Gaussian units, μ_0 is chosen as unity. For optical materials, the total magnetic permeability of the material is almost always essentially unity.

The Poynting vector in Gaussian units is written as:

$$\mathbf{S} = \frac{c}{4\pi}(\mathbf{E} \times \mathbf{H}) \qquad [2.13]$$

Maxwell's equations written in these units are:

$$\begin{aligned} \nabla \times \mathbf{E} &= -\frac{1}{c}\frac{\partial \mathbf{B}}{\partial t} \\ \nabla \times \mathbf{H} &= \frac{4\pi}{c}\mathbf{j} + \frac{1}{c}\frac{\partial \mathbf{D}}{\partial t} \\ \nabla \cdot \mathbf{B} &= 0 \\ \nabla \cdot \mathbf{D} &= 4\pi\rho \end{aligned} \qquad [2.14]$$

Here **E** is the electric field vector, **B** is the magnetic induction vector, **H** is the magnetic vector, **j** is the electric current density, **D** is the electric displacement, c is the speed of light, and ρ is the electric charge density. Assuming a source free region with no space charge:

$$\nabla \times \mathbf{E} = -\frac{1}{c}\frac{\partial \mathbf{B}}{\partial t}$$
$$\nabla \times \mathbf{H} = \frac{4\pi}{c}\mathbf{j} + \frac{1}{c}\frac{\partial \mathbf{D}}{\partial t} \qquad [2.15]$$
$$\nabla \cdot \mathbf{B} = 0$$
$$\nabla \cdot \mathbf{D} = 0$$

Additionally, a homogeneous, isotropic medium is assumed such that:

$$\mathbf{D} = \varepsilon \mathbf{E}$$
$$\mathbf{B} = \mu \mathbf{H} \qquad [2.16]$$
$$\mathbf{j} = \sigma \mathbf{E}$$

Maxwell's equations are then expressed as:

$$\nabla \times \mathbf{E} = -\frac{\mu}{c}\frac{\partial \mathbf{H}}{\partial t}$$
$$\nabla \times \mathbf{H} = \frac{4\pi\sigma}{c}\mathbf{E} + \frac{\varepsilon}{c}\frac{\partial \mathbf{E}}{\partial t} \qquad [2.17]$$
$$\nabla \cdot \mathbf{B} = 0$$
$$\nabla \cdot \mathbf{D} = 0$$

Working with the first equation in [2.17]:

$$\nabla \times \nabla \times \mathbf{E} = \nabla \times \left(-\frac{\mu}{c}\frac{\partial \mathbf{H}}{\partial t} \right) = -\frac{\mu}{c}\frac{\partial}{\partial t}(\nabla \times \mathbf{H}) \qquad [2.18]$$

substituting the second equation of [2.17] into [2.18] leads to an expression for the E field:

$$\nabla^2 \mathbf{E} = \frac{\varepsilon\mu}{c^2}\frac{\partial^2 \mathbf{E}}{\partial t^2} + \frac{4\pi\sigma\mu}{c^2}\frac{\partial \mathbf{E}}{\partial t} \qquad [2.19]$$

A plane wave solution to this equation, propagating in the z-direction with velocity v, is given by:

$$\mathbf{E} = \mathbf{E_0} e^{i\omega\left(t - \frac{z}{v}\right)} \qquad [2.20]$$

where ω is the angular frequency. This solution requires that:

$$\frac{c^2}{v^2} = \varepsilon\mu - i\frac{4\pi\sigma\mu}{\omega} \qquad [2.21]$$

This requirement can be seen simply by inserting equation [2.20] into equation [2.19] and carrying out the operations of equation [2.19]:

$$\nabla^2\left(\mathbf{E_0}e^{i\omega\left(t-\frac{z}{v}\right)}\right) = \frac{\varepsilon\mu}{c^2}\frac{\partial^2}{\partial t^2}\left(\mathbf{E_0}e^{i\omega\left(t-\frac{z}{v}\right)}\right) + \frac{4\pi\sigma\mu}{c^2}\frac{\partial}{\partial t}\left(\mathbf{E_0}e^{i\omega\left(t-\frac{z}{v}\right)}\right) \qquad [2.22]$$

After carrying out the operations and canceling common terms:

$$\frac{\omega^2}{v^2} = \frac{\varepsilon\mu\omega^2}{c^2} - i\frac{4\pi\sigma\mu\omega}{c^2} \qquad [2.23]$$

Equation [2.23] is the same as equation [2.21]. The ratio of c/v is the index of refraction. MacLeod defines the optical (or characteristic) admittance, N, as the c/v ratio, which, by equation [2.21], leads to:

$$N^2 = \varepsilon\mu - i\frac{4\pi\sigma\mu}{\omega} \qquad [2.24]$$

This means that N is a complex variable, which in general can be written as a sum of a real and complex part:

$$N = n - ik \qquad [2.25]$$

Although n and k could be negative in principal, this would not correspond to a physical situation, so n and k are assumed to be positive. MacLeod defines n as the refractive index and k as the extinction coefficient, which is related to the optical absorption coefficient, α, as:

$$\alpha = \frac{4\pi k}{\lambda} \qquad [2.26]$$

Next, equation [2.25] is inserted into equation [2.24].

$$N^2 = (n - ik)^2 = n^2 - i2nk - k^2 = \varepsilon\mu - i\frac{4\pi\sigma\mu}{\omega} \qquad [2.27]$$

The real and imaginary parts of equation [2.27] are equated, and the assumption that μ is unity for optical materials is invoked, giving the following two relations:

$$n^2 - k^2 = \varepsilon \qquad [2.28]$$

$$2nk = \frac{4\pi\sigma}{\omega} \qquad [2.29]$$

By noting that ω can be expressed as:

$$\omega = \frac{2\pi c}{\lambda} \qquad [2.30]$$

and using the definition of N as the ratio of c/v, the expression for the plane wave, equation [2.20], can be rewritten as:

$$\mathbf{E} = \mathbf{E_0}\exp\left[i\left(\omega t - \omega\frac{z}{v}\right)\right] = \mathbf{E_0}\exp\left[i\left(\omega t - \frac{2\pi Nz}{\lambda}\right)\right] \qquad [2.31]$$

Using equation [2.25] for N in equation [2.31] shows how the extinction coefficient k works:

$$\mathbf{E} = \mathbf{E_0}\exp\left[i\left(\omega t - \frac{2\pi(n-ik)z}{\lambda}\right)\right] = \mathbf{E_0}\exp\left[-\frac{2\pi k}{\lambda}z\right]\exp\left[i\left(\omega t - \frac{2\pi n}{\lambda}z\right)\right] \qquad [2.32]$$

Since the exponential term containing k is real and negative, it causes the amplitude to decay as the wave propagates in the z direction.

MacLeod next shows a relationship between **E**, **H**, and N which is very important to the development of this matrix technique:

$$\frac{\mathbf{H}}{\mathbf{r}\times\mathbf{E}} = N \qquad [2.33]$$

where **r** is a vector perpendicular to **E** and **H** and for this simple derivation, will be considered the direction of the wave's propagation. MacLeod next introduces a *modified admittance*, η, although for the case of a normal incidence as assumed at the outset of this section, the modified admittance is exactly the same as the optical admittance, N. So, for purposes of this work, equation [2.33] is rewritten as:

$$\mathbf{H} = N(\mathbf{r}\times\mathbf{E}) \qquad [2.34]$$

Next, equation [2.34] is applied to a simple material boundary in order to see an important relationship used in the matrix technique. Also, superposition is used to break the total field into positive- and negative-going waves.

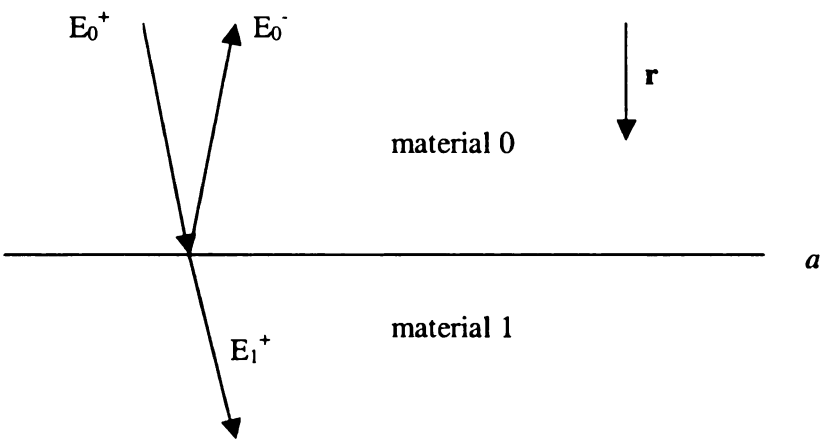

Figure 2.4 A wave encountering a material interface

Figure 2.4 shows a wave, E_0^+, propagating in direction **r**, incident on a material interface, marked by line a, between material 0 and material 1. E_0^- is the reflected wave, and E_1^+ is

the transmitted wave. Equation [2.34] can be used to relate the electric and magnetic fields by:

$$\begin{aligned} \mathbf{H}_0^+ &= N_0\left(\mathbf{r}\times\mathbf{E}_0^+\right) \\ \mathbf{H}_0^- &= N_0\left(-\mathbf{r}\times\mathbf{E}_0^-\right) \end{aligned} \qquad [2.35]$$

MacLeod then goes on to show the derivation of the Fresnel reflection and transmission coefficients, as well as how to handle the case of non-normal incidence. However, equation [2.35] is sufficient to begin the derivation of the multilayer matrix approach. The model will initially be derived for a single layer, and then extended to the case of multiple layers. Figure 2.5 shows a wave incident upon a single layer.

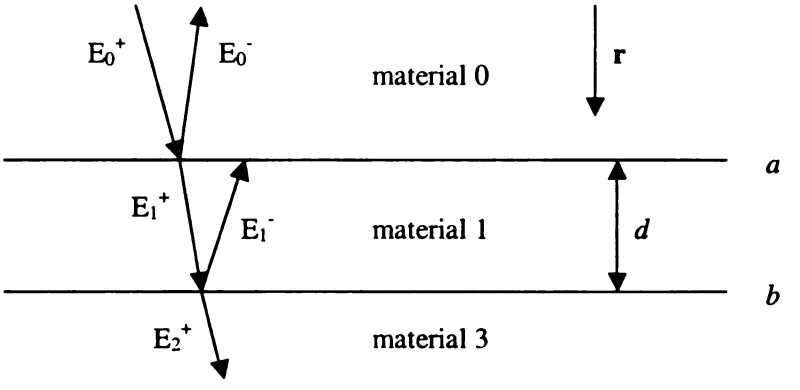

Figure 2.5 a thin layer

Using superposition, the fields in material 1 at boundary *b* can be written as:

$$\mathbf{H}_{1b} = \mathbf{H}_{1b}^{+} + \mathbf{H}_{1b}^{-} = N_1\left(\mathbf{r}\times\mathbf{E}_{1b}^{+}\right) - N_1\left(\mathbf{r}\times\mathbf{E}_{1b}^{-}\right)$$
$$\mathbf{E}_{1b} = \mathbf{E}_{1b}^{+} + \mathbf{E}_{1b}^{-} \qquad [2.36]$$

The electric field equation can be rewritten as:

$$\mathbf{r}\times\mathbf{E}_{1b} = \mathbf{r}\times\mathbf{E}_{1b}^{+} + \mathbf{r}\times\mathbf{E}_{1b}^{-} \qquad [2.37]$$

Equations [2.36] and [2.37] can be combined to eliminate the negative-going portion of the wave, which gives:

$$\mathbf{H}_{1b} = N_1\left(\mathbf{r}\times\mathbf{E}_{1b}^{+}\right) - N_1\left(\mathbf{r}\times\mathbf{E}_{1b} - \mathbf{r}\times\mathbf{E}_{1b}^{+}\right) \qquad [2.38]$$

which simplifies to:

$$2\mathbf{r}\times\mathbf{E}_{1b}^{+} = \frac{\mathbf{H}_b}{N_1} + \mathbf{r}\times\mathbf{E}_{1b} \qquad [2.39]$$

Similarly, the positive-going portion of the wave can be eliminated to give:

$$2\mathbf{r}\times\mathbf{E}_{1b}^{-} = -\frac{\mathbf{H}_{1b}}{N_1} + \mathbf{r}\times\mathbf{E}_{1b} \qquad [2.40]$$

Next, the fields in material 1 at interface *a* are written in terms of the fields at interface *b* by using a propagation term. The propagation term is based on equation [2.31] and the thickness of the layer, *d*. If interface *b* is located at *z*, then interface *a* is located at *z-d* such that:

$$\mathbf{E}(z-d)=\mathbf{E_0}\exp\left[i\left(\omega t-\frac{2\pi N_1(z-d)}{\lambda}\right)\right] \qquad [2.41]$$

Also, this propagation term gives rise to the concept of a "thin" layer, in that it is assumed that the time dependence of the wave is not apparent over the thickness of the film.

$$\mathbf{E}(z-d)\approx\mathbf{E_0}\exp\left[-i\left(\frac{2\pi N_1 z}{\lambda}-\frac{2\pi N_1 d}{\lambda}\right)\right]=\exp\left[i\frac{2\pi N_1 d}{\lambda}\right]\mathbf{E}(z) \qquad [2.42]$$

MacLeod defines the phase factor as δ, so that:

$$\mathbf{E}(z-d)=e^{i\delta}\mathbf{E}(z) \qquad [2.43]$$

with:

$$\delta=\frac{2\pi N_1 d}{\lambda} \qquad [2.44]$$

With this in mind, the fields at interface *a* can now be written conveniently in terms of the fields at interface *b*:

$$\begin{aligned}\mathbf{E}_{1a}^{+}&=\mathbf{E}_{1b}^{+}e^{i\delta}\\ \mathbf{E}_{1a}^{-}&=\mathbf{E}_{1b}^{-}e^{-i\delta}\\ \mathbf{H}_{1a}^{+}&=\mathbf{H}_{1b}^{+}e^{i\delta}\\ \mathbf{H}_{1a}^{-}&=\mathbf{H}_{1b}^{-}e^{-i\delta}\end{aligned} \qquad [2.45]$$

Using equations [2.39] and [2.40], the electric fields are then:

$$\mathbf{r}\times\mathbf{E}_{1a}^{+}=\frac{1}{2}\left(\frac{\mathbf{H}_{1b}}{N_1}+\mathbf{r}\times\mathbf{E}_{1b}\right)e^{i\delta}$$
$$\mathbf{r}\times\mathbf{E}_{1a}^{-}=\frac{1}{2}\left(-\frac{\mathbf{H}_{1b}}{N_1}+\mathbf{r}\times\mathbf{E}_{1b}\right)e^{-i\delta} \qquad [2.46]$$

Equation [2.36] can be used to find expressions for the magnetic fields:

$$\mathbf{H}_{1a}^{+}=N_1\left(\mathbf{r}\times\mathbf{E}_{1a}^{+}\right)=\frac{N_1}{2}\left(\frac{\mathbf{H}_{1b}}{N_1}+\mathbf{r}\times\mathbf{E}_{1b}\right)e^{i\delta}$$
$$\mathbf{H}_{1a}^{-}=-N_1\left(\mathbf{r}\times\mathbf{E}_{1a}^{-}\right)=-\frac{N_1}{2}\left(-\frac{\mathbf{H}_{1b}}{N_1}+\mathbf{r}\times\mathbf{E}_{1b}\right)e^{-i\delta} \qquad [2.47]$$

The total electric field is next written from equation [2.46]:

$$\mathbf{r}\times\mathbf{E}_{1a}=\mathbf{r}\times\mathbf{E}_{1a}^{+}+\mathbf{r}\times\mathbf{E}_{1a}^{-}=\frac{1}{2}\left(\frac{\mathbf{H}_{1b}}{N_1}+\mathbf{r}\times\mathbf{E}_{1b}\right)e^{i\delta}+\frac{1}{2}\left(-\frac{\mathbf{H}_{1b}}{N_1}+\mathbf{r}\times\mathbf{E}_{1b}\right)e^{-i\delta}$$
$$=\frac{1}{2}\left(\frac{\mathbf{H}_{1b}}{N_1}\left(e^{i\delta}-e^{-i\delta}\right)+\mathbf{r}\times\mathbf{E}_{1b}\left(e^{i\delta}+e^{-i\delta}\right)\right) \qquad [2.48]$$

By the applying the Euler identity, this can be simplified further to give:

$$\mathbf{r}\times\mathbf{E}_{1a}=\mathbf{r}\times\mathbf{E}_{1b}(\cos\delta)+\frac{\mathbf{H}_{1b}}{N_1}(i\sin\delta) \qquad [2.49]$$

Similarly, the total magnetic field can be found to be:

$$\begin{aligned}\mathbf{H}_{1a} &= \frac{N_1}{2}\left(\frac{\mathbf{H}_{1b}}{N_1}+\mathbf{r}\times\mathbf{E}_{1b}\right)e^{i\delta}-\frac{N_1}{2}\left(-\frac{\mathbf{H}_{1b}}{N_1}+\mathbf{r}\times\mathbf{E}_{1b}\right)e^{-i\delta}\\ &= \frac{\mathbf{H}_{1b}}{2}\left(e^{i\delta}+e^{-i\delta}\right)+\frac{N_1}{2}\mathbf{r}\times\mathbf{E}_{1b}\left(e^{i\delta}-e^{-i\delta}\right)\\ &= N_1\mathbf{r}\times\mathbf{E}_{1b}(i\sin\delta)+\mathbf{H}_{1b}(\cos\delta)\end{aligned} \qquad [2.50]$$

The results of equations [2.49] and [2.50] can be combined in matrix from:

$$\begin{bmatrix}\mathbf{r}\times\mathbf{E}_{1a}\\ \mathbf{H}_{1a}\end{bmatrix}=\begin{bmatrix}\cos\delta & \frac{i}{N_1}\sin\delta\\ iN_1\sin\delta & \cos\delta\end{bmatrix}\begin{bmatrix}\mathbf{r}\times\mathbf{E}_{1b}\\ \mathbf{H}_{1b}\end{bmatrix} \qquad [2.51]$$

The 2 x 2 matrix in equation [2.51] is called the characteristic matrix for the film. This matrix is a function of the properties of the film, namely, the index of refraction, *N*, and the film thickness, through equation [2.44]. MacLeod then invokes equation [2.33] to eliminate the magnetic field term, while introducing the admittance of the assembly, *Y*, defined as the ratio of the magnetic field to the wave vector crossed with the electric field all at boundary *a*, and using the fact that the electric field parallel to the material boundary is continuous across the boundary:

$$\mathbf{r}\times\mathbf{E}_{0a}\begin{bmatrix}1\\ Y\end{bmatrix}=\begin{bmatrix}\cos\delta & \frac{i}{N_1}\sin\delta\\ iN_1\sin\delta & \cos\delta\end{bmatrix}\begin{bmatrix}1\\ N_2\end{bmatrix}\mathbf{r}\times\mathbf{E}_{2b} \qquad [2.52]$$

Two new variables, *B* and *C*, are defined as the components of the product:

$$\begin{bmatrix}B\\ C\end{bmatrix}=\begin{bmatrix}\cos\delta & \frac{i}{N_1}\sin\delta\\ iN_1\sin\delta & \cos\delta\end{bmatrix}\begin{bmatrix}1\\ N_2\end{bmatrix} \qquad [2.53]$$

Equation [2.53] has all of the information needed to calculate transmission through, reflection from, and absorption in the layer. First, the reflection from the layer will be studied. The relationship between Y, C and B is:

$$Y = \frac{C}{B} \qquad [2.54]$$

Since Y is an equivalent admittance, it can be used in the calculation of the Fresnel reflection coefficient, r, as:

$$r = \frac{N_0 - Y}{N_0 + Y} \qquad [2.55]$$

The power reflection, R, is then:

$$R = r \cdot r^* = \left(\frac{N_0 - Y}{N_0 + Y}\right) \cdot \left(\frac{N_0 - Y}{N_0 + Y}\right)^* \qquad [2.56]$$

In calculating the transmission, first the mean value of the Poynting vector is needed, which is:

$$\overline{\mathbf{S}} = \left[\frac{c}{8\pi}\mathrm{Re}\left(EH^*\right)\right] \cdot \mathbf{r} \qquad [2.57]$$

Equation [2.53] is now used to introduce the variables B and C into the Poynting vector. If the magnitude of the electric field in the final material is denoted by E_{2b}, then the Poynting vector in material 0 can be shown to be:

$$\begin{aligned} \overline{\mathbf{S}}_0 &= \frac{c}{8\pi}\mathrm{Re}\left(BE_{2b} \cdot \left(CE_{2b}\right)^*\right) \cdot \mathbf{r} \\ &= \frac{c}{8\pi}\mathrm{Re}\left(BC^*\right)E_{2b}^2 \cdot \mathbf{r} \end{aligned} \qquad [2.58]$$

The Poynting vector in the final material is:

$$\overline{\mathbf{S}}_2 = \frac{c}{8\pi} N_2 E_{2b}^2 \cdot \mathbf{r} \qquad [2.59]$$

Equation [2.57] can be thought of as proportional to the energy entering the layer, while equation [2.59] is proportional to the energy leaving the layer. To calculate the transmission through the layer, reflection of the incident power must also be considered. Let P_{in} be the total incident power. This leads to the expression:

$$\overline{\mathbf{S}}_0 = (1-R)P_{in} \qquad [2.60]$$

Solving for P_{in} gives:

$$P_{in} = \frac{\frac{c}{8\pi}\mathrm{Re}\left(BC^*\right)E_{2b}^2 \cdot \mathbf{r}}{(1-R)} \qquad [2.61]$$

Equation [2.59] is equivalent to the power leaving the layer, P_{out}, so from [2.58] and [2.61], the transmission through the layer can be easily calculated as:

$$T = \frac{P_{out}}{P_{in}} = \frac{(1-R)N_2}{\mathrm{Re}\left(BC^*\right)} = \frac{(1-R)N_2}{\frac{1}{2}\left(BC^* + B^*C\right)} \qquad [2.62]$$

where R can be calculated from equation [2.56]. Although transmission calculations can be made from equation [2.62], this expression can be further simplified in an effort to aid computational speed. First, combining equations [2.54] and [2.56] gives:

$$\begin{aligned} R &= \left(\frac{N_0 - \frac{C}{B}}{N_0 + \frac{C}{B}}\right)\cdot\left(\frac{N_0 - \frac{C}{B}}{N_0 + \frac{C}{B}}\right)^* \\ &= \left(\frac{N_0 B - C}{N_0 B + C}\right)\cdot\left(\frac{N_0 B - C}{N_0 B + C}\right)^* \end{aligned} \qquad [2.63]$$

Using [2.63], 1-R can be seen to be:

$$1-R=\left(\frac{N_0B+C}{N_0B+C}\right)\cdot\left(\frac{N_0B+C}{N_0B+C}\right)^{*}-\left(\frac{N_0B-C}{N_0B+C}\right)\cdot\left(\frac{N_0B-C}{N_0B+C}\right)^{*}$$
$$=\frac{2N_0\left(BC^{*}+B^{*}C\right)}{\left(N_0B+C\right)\left(N_0B+C\right)^{*}} \qquad [2.64]$$

Equation [2.64], can be inserted into [2.62] to give an expression for the transmission through the film:

$$T=\frac{4N_0N_2}{\left(N_0B+C\right)\left(N_0B+C\right)^{*}} \qquad [2.65]$$

Equation [2.65] is used to calculate transmission when applying MacLeod's technique. However, as derived, equation [2.65] is specifically for one layer. This is not a problem, though, since this approach can easily be extended to the case of multiple layers.

If a two-layered system is considered, as shown in Figure 2.6, a development analogous to the preceding will give the result:

$$\mathbf{r}\times\mathbf{E}_{0a}\begin{bmatrix}1\\Y\end{bmatrix}=\begin{bmatrix}\cos\delta_1 & \frac{i}{N_1}\sin\delta_1\\ iN_1\sin\delta_1 & \cos\delta_1\end{bmatrix}\begin{bmatrix}\cos\delta_2 & \frac{i}{N_2}\sin\delta_2\\ iN_2\sin\delta_2 & \cos\delta_2\end{bmatrix}\begin{bmatrix}1\\N_3\end{bmatrix}\mathbf{r}\times\mathbf{E}_{3b} \qquad [2.66]$$

where materials are now indexed by 0 through 3.

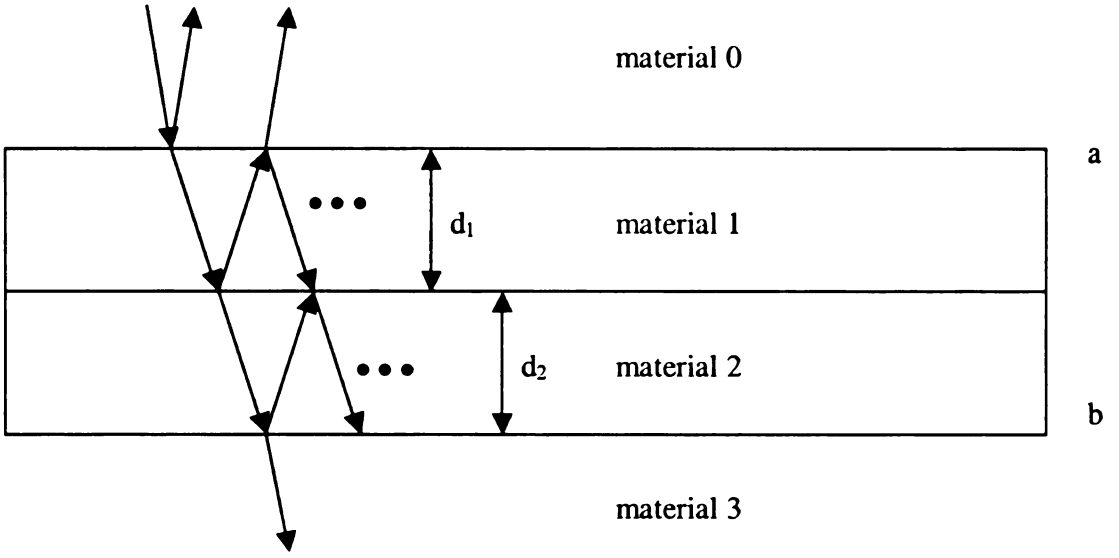

Figure 2.6 A multilayer stack of materials

For a stack of an arbitrary number of m layers, such an analysis gives

$$\mathbf{r}\times\mathbf{E}_{0a}\begin{bmatrix}1\\Y\end{bmatrix}=\prod_{n=1}^{m}\begin{bmatrix}\cos\delta_n & \frac{i}{N_n}\sin\delta_n\\ iN_n\sin\delta_n & \cos\delta_n\end{bmatrix}\begin{bmatrix}1\\N_{m+1}\end{bmatrix}\mathbf{r}\times\mathbf{E}_{(m+1)b} \qquad [2.67]$$

The characteristic matrix for this assembly is written:

$$\begin{bmatrix}B\\C\end{bmatrix}=\prod_{n=1}^{m}\begin{bmatrix}\cos\delta_n & \frac{i}{N_n}\sin\delta_n\\ iN_n\sin\delta_n & \cos\delta_n\end{bmatrix}\begin{bmatrix}1\\N_{m+1}\end{bmatrix} \qquad [2.68]$$

Equation [2.65] can be used to calculate the transmission of the assembly, by simply rewriting the equation:

$$T=\frac{4N_0N_{m+1}}{(N_0B+C)(N_0B+C)^*} \qquad [2.69]$$

As an example, a modeling calculation for a gold-diamond-gold Fabry-Perot resonator is shown in Figure 2.7. Calculations are based upon a diamond membrane thickness of 1.0

μm, and partially transparent gold film coatings of 25 nm. Optical data for gold is taken from Kingslake[35]. The index of refraction for diamond is taken from the Sellmeier equation. These modeling results account for absorption in the gold films but do not account for absorption in the diamond or for scattering losses at rough surfaces.

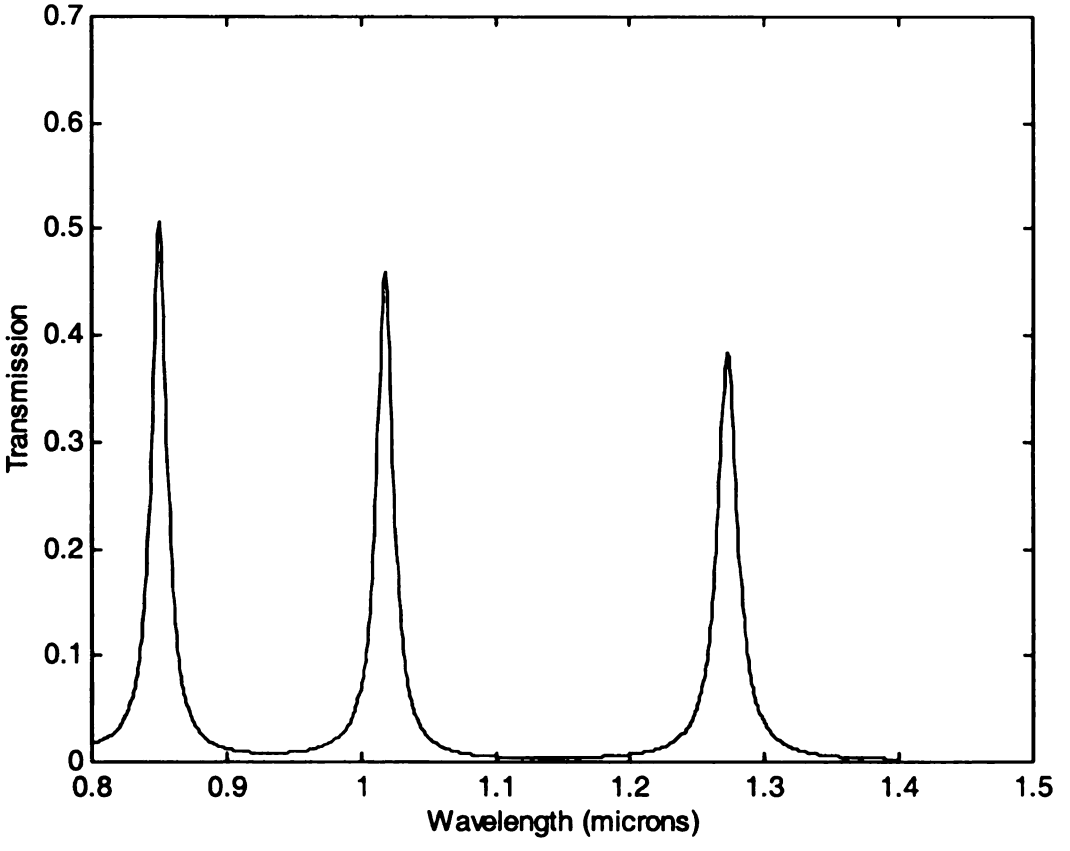

Figure 2.7 Theoretical calculation of transmission versus wavelength for a gold-diamond-gold optical resonator with d=1μm of diamond, and 25nm gold layers on each side.

2.4.2 Transfer Matrix Method

The transfer matrix technique[36] explicitly uses the Fresnel coefficients along with a superposition of electric fields to solve the problem of multilayer optics.

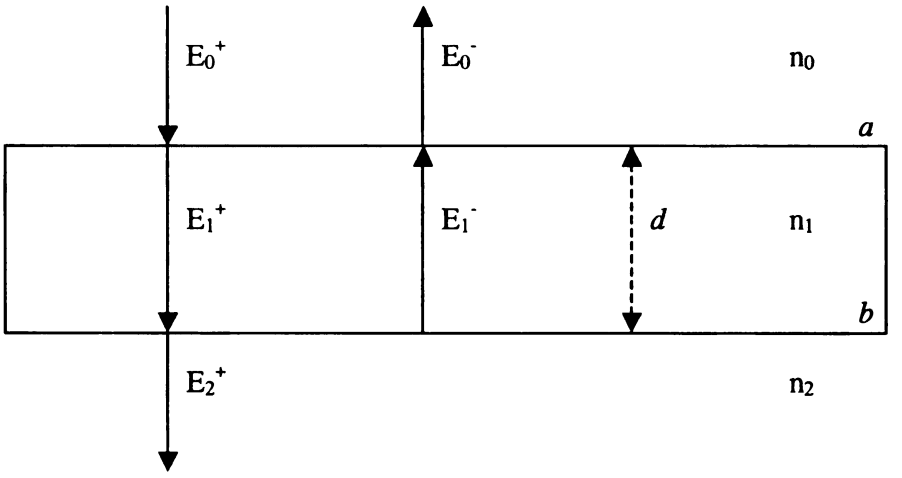

Figure 2.8 A single thin layer

Figure 2.8 shows a thin layer, of thickness *d*, where *a* and *b* denote the two material interfaces in the system. An electric field of E_{0a}^+ is incident upon the structure. The incident field causes a reflected field, E_{0a}^-, which travels in the opposite direction to the incident field, as well as fields internal to the layer, E_{1a}^+ and E_{1a}^-, where the + and – signs indicate direction of travel. The field transmitted through the layer is E_{2b}^+. It is assumed that E_{2b}^- is equal to zero, which means that there is no optical source or additional material boundaries to cause reflection in medium n_2.

The aim of the transfer matrix method is to find the ratio of the reflected, E_{0a}^-, (or transmitted, E_{2b}^+) field to the incident field, E_{0a}^+. This is accomplished by noting that at the interface *a*, E_{1a}^+ is the sum of the fraction of E_{0a}^+ transmitted through the interface and the fraction of E_{1a}^- reflected from the interface, which can be written as:

$$E_{0a}^+ = \frac{1}{t_{01}} E_{1a}^+ - \frac{r_{10}}{t_{01}} E_{1a}^- \qquad [2.70]$$

Similarly, the reflected field can also be written as a sum of two other fields, which can be written in matrix notation as:

$$E_{0a}^{-} = t_{10}E_{1a}^{-} + r_{01}E_{0a}^{+} \qquad [2.71]$$

Inserting equation [2.70] into equation [2.71] gives:

$$\begin{aligned} E_{0a}^{-} &= t_{10}E_{1a}^{-} + r_{01}\left(\frac{1}{t_{01}}E_{1a}^{+} - \frac{r_{10}}{t_{01}}E_{1a}^{-}\right) \\ &= \frac{r_{01}}{t_{01}}E_{1a}^{+} + \frac{1}{t_{01}}(t_{01}t_{10} - r_{10}r_{01})E_{1a}^{-} \end{aligned} \qquad [2.72]$$

Equations [2.70] and [2.72] can be written in matrix form as:

$$\begin{bmatrix} E_{0a}^{+} \\ E_{0a}^{-} \end{bmatrix} = \frac{1}{t_{01}}\begin{bmatrix} 1 & -r_{10} \\ r_{01} & t_{01}t_{10} - r_{01}r_{10} \end{bmatrix}\begin{bmatrix} E_{1a}^{+} \\ E_{1a}^{-} \end{bmatrix} \qquad [2.73]$$

Equation [2.73] can be significantly simplified by noting that:

$$\begin{aligned} t_{01}t_{10} - r_{01}r_{10} &= \frac{(2n_0)(2n_1)}{(n_0+n_1)^2} - \frac{(n_0-n_1)(n_1-n_0)}{(n_0+n_1)^2} \\ &= \frac{4n_0n_1 + n_0^2 + n_1^2 - 2n_0n_1}{(n_0+n_1)^2} = 1 \end{aligned} \qquad [2.74]$$

and that:

$$r_{10} = -r_{01} \qquad [2.75]$$

So, incorporating equations [2.74] and [2.75] into equation [2.73] gives:

$$\begin{bmatrix} E_{0a}^{+} \\ E_{0a}^{-} \end{bmatrix} = \frac{1}{t_{01}}\begin{bmatrix} 1 & r_{01} \\ r_{01} & 1 \end{bmatrix}\begin{bmatrix} E_{1a}^{+} \\ E_{1a}^{-} \end{bmatrix} \qquad [2.76]$$

Equation [2.76] is used to find the relationship between the fields on opposite sides of a boundary. Equation [2.45] can be used to see how the fields propagate across the thickness of the layer. Writing the electric fields of [2.45] in matrix form gives:

$$\begin{bmatrix} E_{1a}^{+} \\ E_{1a}^{-} \end{bmatrix} = \begin{bmatrix} e^{i\delta} & 0 \\ 0 & e^{-i\delta} \end{bmatrix} \begin{bmatrix} E_{1b}^{+} \\ E_{1b}^{-} \end{bmatrix} \quad [2.77]$$

Equations [2.76] and [2.77] can be combined to describe the wave from material n_0 up to interface b in material n_1:

$$\begin{bmatrix} E_{0a}^{+} \\ E_{0a}^{-} \end{bmatrix} = \frac{1}{t_{01}} \begin{bmatrix} 1 & r_{01} \\ r_{01} & 1 \end{bmatrix} \begin{bmatrix} e^{i\delta} & 0 \\ 0 & e^{-i\delta} \end{bmatrix} \begin{bmatrix} E_{1b}^{+} \\ E_{1b}^{-} \end{bmatrix} \quad [2.78]$$

The description of the system is complete when the matrix transferring the wave from material n_1 into material n_2 is written:

$$\begin{bmatrix} E_{1b}^{+} \\ E_{1b}^{-} \end{bmatrix} = \frac{1}{t_{12}} \begin{bmatrix} 1 & 0 \\ r_{12} & 0 \end{bmatrix} \begin{bmatrix} E_{2b}^{+} \\ 0 \end{bmatrix} \quad [2.79]$$

Equations [2.78] and [2.79] are then combined to write a full description of the wave from material n_0 to material n_2:

$$\begin{bmatrix} E_{0a}^{+} \\ E_{0a}^{-} \end{bmatrix} = \frac{1}{t_{01}t_{12}} \begin{bmatrix} 1 & r_{01} \\ r_{01} & 1 \end{bmatrix} \begin{bmatrix} e^{i\delta} & 0 \\ 0 & e^{-i\delta} \end{bmatrix} \begin{bmatrix} 1 & 0 \\ r_{12} & 0 \end{bmatrix} \begin{bmatrix} E_{2b}^{+} \\ 0 \end{bmatrix} \quad [2.80]$$

which has a general form of:

$$\begin{bmatrix} E_{0a}^{+} \\ E_{0a}^{-} \end{bmatrix} = \begin{bmatrix} a & b \\ c & d \end{bmatrix} \begin{bmatrix} E_{2b}^{+} \\ 0 \end{bmatrix} \quad [2.81]$$

The ratio of the transmitted field to the incident field can then be found by:

$$\frac{E_{2b}^{+}}{E_{0a}^{+}} = \frac{1}{a} \quad [2.82]$$

The power transmission can be calculated by:

$$T = \left(\frac{1}{a}\right)^{*} \left(\frac{1}{a}\right) \quad [2.83]$$

This approach can be easily generalized to the case or many layers. Essentially, one matrix is needed for each interface, and an additional matrix is needed for each layer to account for the change in phase as the wave travels the thickness of the layer. Thus, for a system of m layers between interfaces a and b, the equivalent of equation [2.80] would be:

$$\begin{bmatrix} E_{0a}^{+} \\ E_{0a}^{-} \end{bmatrix} = \left(\prod_{j=0}^{(m-1)} \frac{1}{t_{(j)(j+1)} t_{(j+1)(j+2)}} \begin{bmatrix} 1 & r_{(j)(j+1)} \\ r_{(j)(j+1)} & 1 \end{bmatrix} \begin{bmatrix} e^{i\delta_j} & 0 \\ 0 & e^{-i\delta_j} \end{bmatrix} \right) \cdots \cdots \begin{bmatrix} 1 & 0 \\ r_{(m)(m+1)} & 0 \end{bmatrix} \begin{bmatrix} E_{(m+1)b}^{+} \\ 0 \end{bmatrix} \quad [2.84]$$

Despite it's more complex appearance, equation [2.84] still can be reduced to a general form of equation [2.81], and thus equation [2.82] and [2.83] can be used to find transmission for the system.

2.5 Effect of Interface Roughness on Transmission Through a Single Surface

When a wave reflects from a smooth surface, the reflection is in a specific direction, according to electromagnetic theory. This is called the *specular* direction. When a wave is incident on a medium with a small, random surface roughness, the reflected energy will be distributed in some manner about the specular direction. This research will focus on a one-dimensional transmission problem, so when the reflected energy is no longer totally in the specular direction, it corresponds to a loss mechanism.

Figure 2.9 shows the general scattering geometry for a harmonic plane wave incident upon a rough surface with a mean value of z=0 for the surface heights, where I is the

plane of incidence, which is perpendicular to the y direction, and R is the plane of reflection which can be rotated by an angle θ_3 away from the x-axis. The incident beam is rotated by an angle θ_1 from the z-axis, while the reflected beam is rotated by an angle θ_2 from the z-axis. Note that for a smooth surface and specular reflection, the angle θ_2 will be equal to θ_1, and θ_3 will be zero.

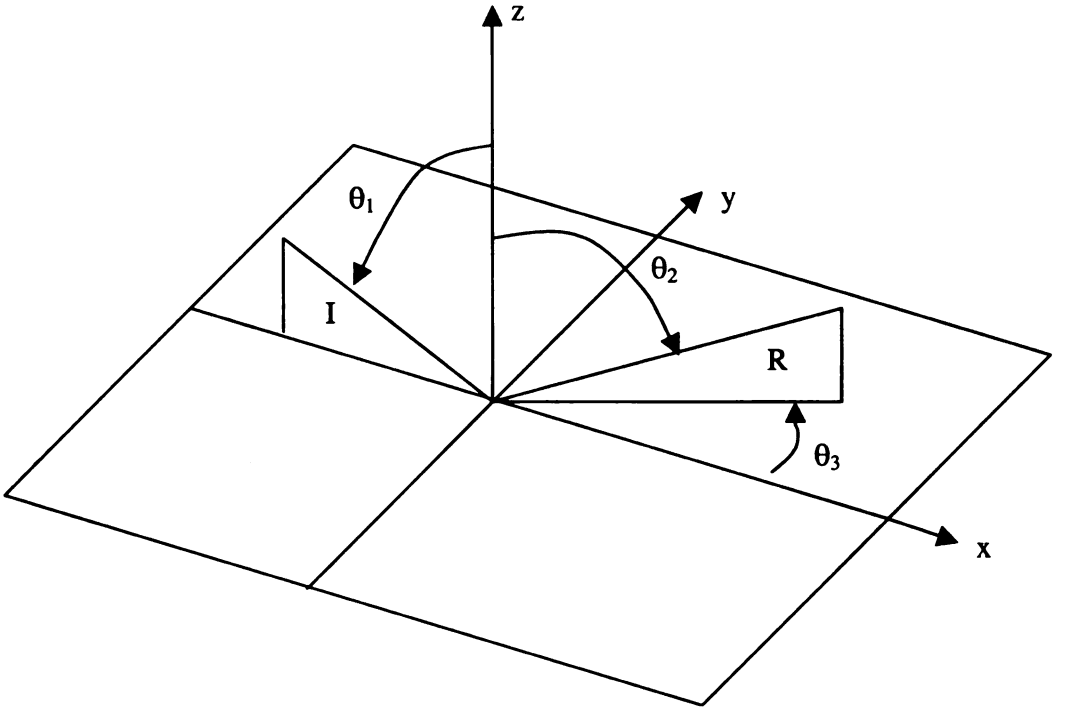

Figure 2.9 The general scattering geometry

Beckman[37] shows that the case of a rough surface with a random Gaussian distribution, which has a small standard deviation compared to the incident wavelength, can be solved with only two dimensions if the parameters of the distribution are constant over the x-y plane. Under these conditions, θ_3 is nearly equal to zero and θ_2 is nearly equal to θ_1.

Additional assumptions that Beckman employs are: that the incident wavelength, λ, is much larger than the RMS value of the surface roughness, σ; that the extent of the surface in the x and y directions, L, is much larger than λ; and that no correlation exists in the distribution. Conceptually, this set of assumptions may be likened to a radio wave being incident upon a dense forest with treetops spaced much closer than the incident wavelength, thus the treetops would form a very random surface profile. This is in contrast to a gently rolling meadow, where the surface height could still be considered random, but the separation between peaks is not small compared to the wavelength.

Under this set of assumptions, Beckman shows that the mean field reflected in the specular direction can be written as:

$$\langle E_{20} \rangle = E_2 \operatorname{sinc}\left[\frac{2\pi}{\lambda}(\sin\theta_1 - \sin\theta_2)L\right] \cdot \exp\left(-\frac{2\pi\sigma^2}{\lambda^2}(\cos\theta_1 + \cos\theta_2)^2\right) \quad [2.85]$$

Where E_2 is the total field reflected, and E_{20} is the field reflected in the specular direction. For normal incidence, as is the case for this research, θ_1 and θ_2 are taken to be zero, and the reflected power in the specular direction is then shown to be:

$$\langle E_{20} \rangle \langle E_{20} \rangle^* = E_2 \cdot E_2^* \exp\left(-\left(\frac{4\pi\sigma}{\lambda}\right)^2\right) \quad [2.86]$$

This result can also be obtained by considering a sum of plane waves.

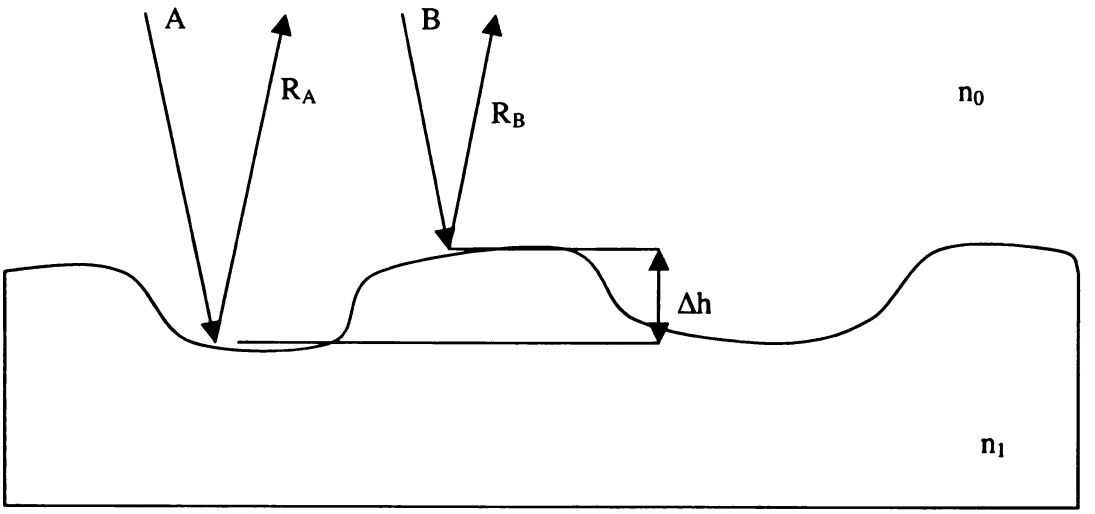

Figure 2.10 Cross-section of a rough interface

Figure 2.10 shows two beams incident upon a rough surface. R_A and R_B are the reflected beams, and Δh is the difference in surface height from which the beams are reflected. Assuming that the incident beams are initially in-phase, of the same amplitude, and that they are normally incident on the sample, the incident wave can be written as:

$$E_{i0}(z) = 2E_i e^{i\frac{2\pi n_0}{\lambda_0}z} = E_i e^{i\frac{2\pi n_0}{\lambda_0}z} + E_i e^{i\frac{2\pi n_0}{\lambda_0}z} \qquad [2.87]$$

where λ_0 is the free space wavelength and n_0 is the index of refraction. The reflected wave can then be written as:

$$E_{r0}(z) = r_0 E_i e^{-i\frac{2\pi n_0}{\lambda_0}(z+2\Delta h)} + r_0 E_i e^{-i\frac{2\pi n_0}{\lambda_0}z} \qquad [2.88]$$

where r_0 is the Fresnel reflection coefficient for the surface[38]:

$$r_0 = \frac{n_1 - n_0}{n_1 + n_0} \qquad [2.89]$$

The phase difference between the reflected waves is:

$$R_r = R_s \exp\left(-\left(\frac{4\pi\Delta h n_0}{\lambda_0}\right)^2\right) \qquad [2.90]$$

The reflected wave can be rewritten as:

$$E_{r0}(z) = r_0 E_i e^{-i\frac{2\pi n_0}{\lambda_0}z}\left(1 + e^{-i\frac{4\pi n_0 \Delta h}{\lambda_0}}\right) \qquad [2.91]$$

If instead of having reflections from two surfaces, reflections from many surfaces are considered, the reflected wave could be written as:

$$E_{r0}(z) = r_0 E_i e^{-i\frac{2\pi n_0}{\lambda_0}z} + r_0 E_i e^{-i\frac{2\pi n_0}{\lambda_0}(z+2\Delta h_1)} + r_0 E_i e^{-i\frac{2\pi n_0}{\lambda_0}(z+2\Delta h_2)} + \ldots \qquad [2.92]$$

$$E_{r0}(z) = r_0 E_i \sum_j e^{-i\frac{2\pi n_0}{\lambda_0}\left(z+2\Delta h_j\right)} \qquad [2.93]$$

If the summation is converted to an integration over the z-direction, and the surface heights are assumed to have a Gaussian distribution in the z-direction, denoted by z', the average reflected field will be:

$$\langle E_{r0}(z)\rangle = r_0 E_i e^{-i\frac{2\pi n_0}{\lambda_0}z} \int_{-\infty}^{\infty} w(z') e^{-i\frac{2\pi n_0}{\lambda_0}z'} dz' \qquad [2.94]$$

where $w(z')$ is the Gaussian distribution with standard deviation of σ:

$$w(z') = \frac{1}{\sigma\sqrt{2\pi}} e^{-\frac{z'^2}{2\sigma^2}} \qquad [2.95]$$

Inserting $w(z')$ into the integral of equation [2.95], the reflected field can be found to be:

$$\langle E_{r0}(z)\rangle = r_0 E_i e^{-i\frac{2\pi n_0}{\lambda_0}z} e^{-\frac{1}{2}\left(\frac{4\pi n_0\sigma}{\lambda_0}\right)^2} \quad [2.96]$$

The total power reflected in the specular direction can be found as:

$$\langle E_{r0}(z)\rangle\langle E_{r0}(z)\rangle^* = r_0 E_i e^{-i\frac{2\pi n_0}{\lambda_0}z} e^{-\frac{1}{2}\left(\frac{4\pi n_0\sigma}{\lambda_0}\right)^2} r_0 E_i^* e^{i\frac{2\pi n_0}{\lambda_0}z} e^{-\frac{1}{2}\left(\frac{4\pi n_0\sigma}{\lambda_0}\right)^2} \quad [2.97]$$

$$\langle E_{r0}(z)\rangle\langle E_{r0}(z)\rangle^* = r_0^2 E_i E_i^* e^{-\left(\frac{4\pi n_0\sigma}{\lambda_0}\right)^2} \quad [2.98]$$

This is the same as Beckman's result for normal incidence.

Filinski[39] first shows the same result, and then extends this approach to transmission through the interface. Consider the situation shown in Figure 2.11.

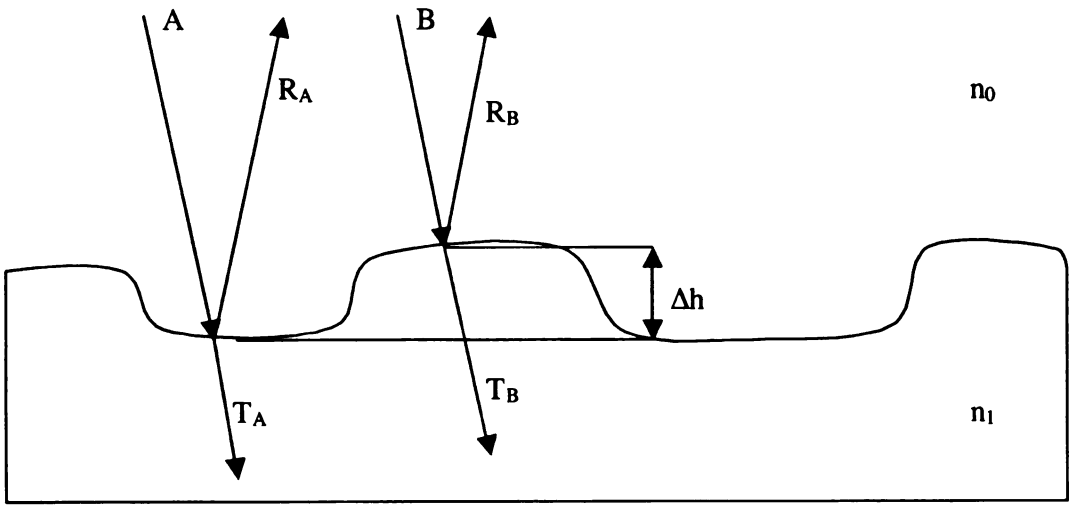

Figure 2.11 Cross-section of a rough interface

A and B represent incident beams of light. R_A and R_B represent reflected beams, and T_A and T_B represent transmitted beams. Δh is the difference in height between the points on the surface the beams are reflected from. The two different media are again represented by their indices of refraction, n_0 and n_1. Assuming that A and B are initially in phase and normally incident upon the surface, the phase difference of the transmitted waves can be expressed as:

$$\Delta\Phi_{Tr} = \frac{2\pi\Delta h}{\lambda_0}(n_1 - n_0) \qquad [2.99]$$

The transmitted wave could thus be written as:

$$E_{t0}(z) = t_0 E_i e^{-i\frac{2\pi n_1}{\lambda_0}z}\left(1 + e^{-i\frac{2\pi\Delta h}{\lambda_0}(n_1 - n_0)}\right) \qquad [2.100]$$

where t_0 is the transmission coefficient for the surface:

$$t_0 = \frac{2n_0}{n_1 + n_0} \qquad [2.101]$$

If, as in equation [2.93], a summation of many interfaces is considered the transmitted wave can be written as:

$$E_{t0}(z) = t_0 E_i e^{-i\frac{2\pi n_1}{\lambda_0}z}\sum_j e^{-i\frac{2\pi\Delta h_j}{\lambda_0}(n_1 - n_0)} \qquad [2.102]$$

Again, this summation will be converted to an integration over a Gaussian distribution of surface heights:

$$\langle E_{t0}(z)\rangle = t_0 E_i e^{-i\frac{2\pi n_1}{\lambda_0}z}\int_{-\infty}^{\infty} w(z')e^{-i\frac{2\pi(n_1 - n_0)}{\lambda_0}z'}dz' \qquad [2.103]$$

$w(z')$ is again the Gaussian distribution with a standard of σ, and thus the integral can be evaluated to give:

$$\langle E_{t0}(z)\rangle = t_0 E_i e^{-i\frac{2\pi n_1}{\lambda_0}z} e^{-\frac{1}{2}\left(\frac{2\pi\sigma(n_1-n_0)}{\lambda_0}\right)^2} \qquad [2.104]$$

This can now be used to find the power transmission coefficient for the rough surface:

$$T_r = \left|\frac{\langle E_{t0}(z)\rangle\langle E_{t0}(z)\rangle^* n_1}{\langle E_i(z)\rangle\langle E_i(z)\rangle^* n_0}\right| \qquad [2.105]$$

which Filinski expresses as:

$$T_r = T_s \exp\left[-(\Delta\Phi_{Tr})^2\right] = (1-R_s)\exp\left(-\left(\frac{2\pi\sigma(n_1-n_0)}{\lambda_0}\right)^2\right) \qquad [2.106]$$

where T_s is the transmission if the surface was smooth, and R_s is the power reflection coefficient for a smooth surface.

2.6 Concluding Remarks

In this chapter, the optical properties of diamond, including thin film diamond of the type used in this research have been reviewed. The matrix approach to multilayer modeling of thin films was described, as well as performance measures of Fabry-Perot resonators and impacts of surface roughness. The research presented in the remainder of this thesis aims to incorporate all of these issues in the fabrication and analysis of on-chip diamond-based Fabry-Perot resonators.

References:

[1] J. Verdeyor, Laser Electronics, Prentice Hall, Englewood Cliffs, NJ, 1989.

[2] J. Han and D. P. Neikirk, "Deflection behavior of Fabry-Perot pressure sensors having planar and corrugated membrane," SPIE's Micromachining and Microfabrication '96 Symposium: Micromachined Devices and Components II, R. Roop and K. Chau, Proc. SPIE 2882, Austin, Texas, USA, 14-15 October, 1996, pp. 79-90.

[3] S. Ahmadi and M. Zaghloul, "A Fabry-Perot Optical Sensor System-on-Chip", Can. J. Elect. & Comp. Eng., Vol. 26, NO 3/4, July/Oct 2001, PP159-162.

[4] R. A. Booth and D. K. Reinhard, "Diamond Thin-Film Fabry-Perot Optical Resonators", ADC-FCT 2001, August 5-10 2001, Auburn, AL, USA.

[5] J. H. Correia and C. Couto, "MEMS: a New Joker in Microinstrumentation", IEEE Industrial Electronics Newsletter, January 2000.

[6] J. H. Correia, M. Bartek and R. F. Wolffenbuttel, "High Selectivity single-chip spectrometer for operation at visible wavelengths", Proc. 1998 IEEE IEDM, December 6-9, 1998, San Francisco, USA.

[7] J. H. Correia, M. Bartek, R. F. Wolffenbuttel, "High-Selectivity Single-Chip Spectrometer in Silicon for Operation at Visible Part of the Spectrum", IEEE Transactions on Electron Devices, Vol. 47, No. 3, March 2000, PP 553-559.

[8] M. Bartek, I Novotny, J. H. Correia, V. Tvarozek, "Quality Factor of Thin-Film Fabry-Perot Resonators: Dependence on Interface Roughness", EuroSensors XIII, September 12-15, 1999, The Hague, The Netherlands.

[9] M. Bartek, J. H. Correia, S. H. Kong, and R. F. Wolffenbuttel, "Stray-Light Compensation in Thin-Film Fabry-Perot Optical Filters: Application to an On-Chip Spectrometer", Transducers '99, June 7-10, 1999, Sendai, Japan.

[10] J.H. Jerman, D.J. Clift and S.R. Mallisnson, "A miniature Fabry-Perot Interferometer with a Corrugated Diaphragm Support," Technical Digest IEEE Solid State Sensor and Actuator Workshop, Hilton Head, June 1990, PP 140-144.

[11] H. Saari, R. Mannila, J. Antila, M Blomberg, O. Rusaned, "Miniaturized Gas Sensor Using a Micromachined Fabry-Perot Interferometer", Preparing for the Future, Vol. 10 No. 3, October 2000 PP 4-5.

[12] Y. Kim and D. P. Neikirk, "Design for Manufacture of Micro Fabry-Perot Cavity-based Sensors" Sensors and Actuators A 50, Jan. 1996, pp. 141-146.

[13] Y. Kim and D. P. Neikirk, "Micromachined Fabry-Perot Cavity Pressure Transducer" IEEE Photonics Technology Letters 7, Dec. 1995, pp. 1471-1473.

[14] D. Shin, S. Tibuleac, T. A. Maldonado, and R. Magnusson, "Thin-Film optical filters with diffractive elements and waveguides", Opt. Eng., September 1998, PP 2634-2646.

[15] M. Seal and W. J. P. van Enckevort, "Applications of diamond in optics", SPIE Vol. 969 Diamond Optics, 1988 PP 144-152.

[16] F. Urbach, Phys. Rev., **92**, PP1324, 1953.

[17] C. D. Clark, "Optical Properties of Natural Diamond", Physical Properties of Diamond, ed. R. Berman, Clarendon Press, Oxford, 1965.

[18] D. K. Reinhard, Diamond Films Handbook, Chapter 14, J. Asmussen and D. K. Reinhard, Eds, Marcel Dekker, Inc. New York, NY, 2001.

[19] M. Thomas and W. J. Tropf, Johns Hopkins APL Tech. Dig. 14; P.16, 1993.

[20] M. P. Marder, Condensed Matter Physics, John Wiley & Sons, New York, NY, 2000.

[21] A. Feldman and L. H. Robins, "Critical assessment of optical properties of CVD Diamond Films", Applications of Diamond Films and Related Materials, Y. Tzeng, M. Yoshikawa, M. Murakawa, and A. Feldman, Eds, Elsevier Science, 1991, PP 181-188.

[22] A. T. Collins, M. Kamo, Y. Sato, "A spectroscopic study of optical centers in diamond grown by microwave-assisted chemical vapor deposition", J. Mater. Res., **5**, 1990, PP 2507-2514.

[23] V. Vorlicek, J. Rosa, M. Vanecek, M. Nesladek, L. M. Stals, "Quantitative study of Raman scattering and defect optical absorption in CVD diamond films", Diamond and Related Materials, 6 (5-7): 704-707 1997.

[24] D. C. Harris, "Development of Chemical-Vapor-Deposited Diamond for Infrared Optical Applications. Status Report and Summary of Properties", Naval Air Warfare Center Weapons Division, July 1994.

[25] A.J. Gatesman, R. H. Giles, and J. Waldman, Diamond Optics III, SPIE Volume. 1325, The International Society for Optical Engineering, Washington, 1990.

[26] L.H. Robbins, E. N. Farabaugh, A. Feldman, Diamond Optics IV. SPIE Volume 1534, The International Society for Optical Engineering, Washington, 1991.

[27] X. Ying, Y. Shen, H. Xue, L. Jianhai, Z. Xing, J. Xu and F. Zhang, Diamond Optics V, SPIE Vol. 1759, The International Society for Optical Engineering, Washington, 1992.

[28] P. Rouard, Annuel de Physique 7, 291, (1937).

[29] A. Nussbaum and R. A. Phillips, Contemporary Optics For Scientists and Engineers, Prentice Hall, Inc., New Jersey, 1976.

[30] O. S. Heavens, Optical Properties of Thin Solid Films, Butterworths, London, 1955.

[31] F. Abeles, Advanced Optical Techniques, A.C.S. Van Heel ed, North-Holland Publishing Co., Amsterdam, 1967.

[32] H.A. MacLeod, Applied Optics and Optical Engineering, R.R. Shannon and J.C. Wyant eds, Academic Press, New York, NY, 1987.

[33] H.A. MacLeod, Thin-Film Optical Filters, American Elsevier Publishing Co., New York, NY, 1969.

[34] Born and Wolf, Principles of Optics, Pergamon Press, New York, NY, 1959.

[35] R. Kingslake, Applied Optics and Optical Engineering, Academic Press, New York, NY, 1965.

[36] O.S. Heavens, Optical properties of Thin Solid Films, Dover, New York, 1965.

[37] P. Beckmann and A. Spizzichino, The Scattering of Electromagnetic Waves from Rough Surfaces, Pergamon Press, Oxford, 1963.

[38] R. Harrington, Time-Harmonic Electromagnetic Fields, McGraw Hill, New York, NY 1961.

[39] I. Filinski, "Effects of Sample Imperfections on Optical Spectra", Phys. Stat. Sol. (b), 49, 577-588, (1972).

Chapter 3: Experimental Methods

3.1 Introduction

This chapter describes the experimental aspect of this research, including the fabrication of the device and the techniques used to characterize the device optically. The goal of this chapter is to convey an understanding of the methods used to create and measure the samples in this research.

3.2 Device Fabrication

The fabrication of the device involves a series of many steps. First, an overview of the fabrication sequence is given. Next, the oxidation and photolithography steps are discussed. The diamond deposition is described, and then the method used to achieve through-etch of the wafer is presented. At this point in the sequence it is necessary to perform an optical measurement of the sample to document the diamond thickness before proceeding to the last fabrication sequence, sputtering thin gold films to complete the Fabry-Perot device. Also, atomic force microscopy (AFM) and scanning electron microscopy (SEM) are used to document device topology and morphology. Finally the methods used to measure the optical performance of the finished device are described.

3.2.1 Fabrication Overview

Figure 3.1 shows a conceptual cross-sectional final view of the device constructed for this study. The Fabry-Perot device is fabricated on a double-side polished, 2" diameter (100) lightly doped (1-10 ohm-cm) p-type silicon wafer with an approximate thickness of 250 μm, which has been through an RCA cleaning process[1].

As can be seen in Figure 3.1, in certain spots the entire thickness of the wafer is anisotropically etched away in order to form a diamond membrane approximately 1μm thick, supported on 4 sides by the remaining silicon. The first step in the device fabrication is to grow a thermal oxide on the wafer that will eventually serve as a mask for the aforementioned through-etch of the wafer. For this reason, the desired thickness of the oxide layer is a function of the wafer thickness, as well as the relative etch rates of silicon and silicon-dioxide in the etching solution.

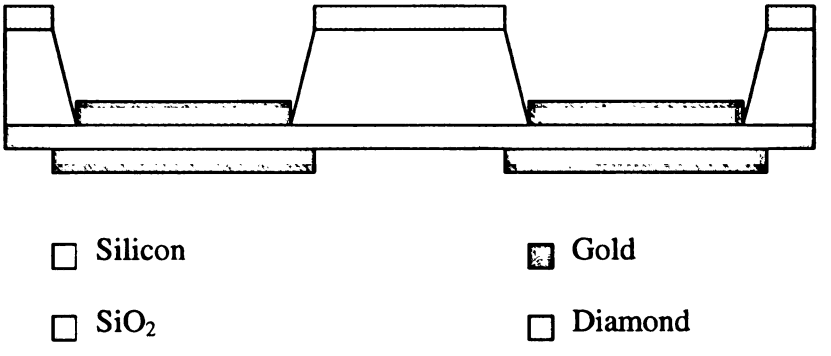

Figure 3.1 Cross-sectional view of two Fabry-Perot resonators. Drawing not to scale.

Bean[2] gives the oxide etch rate in KOH/H_2O solution as approximately 3 nm per minute. Others report even slower rates for etching oxide. For the KOH/H_2O solution used in this

research, the reported etch rates for silicon are between 250 and 330nm per minute. This means the minimum oxide mask thickness should be approximately 1% of the thickness of the wafer in order to avoid the etching of silicon in the masked area. However, in this application, some etching of the masked silicon is tolerable since the silicon would still be thick enough to support the diamond windows. Thus, for a 250μm thick silicon wafer, the target oxide thickness was taken to be 2μm. After oxidation, the next step is patterning of the oxide followed by diamond deposition and silicon etching. Finally, gold mirrors are sputtered, resulting in the structure in Figure 3.1.

3.2.2 Oxidation

For a target oxide thickness of approximately 2μm, the Deal-Grove oxidation model[3] indicates approximately 8.5 hours of wet oxidation, or 150 hours of dry oxidation time, at 1100°C. However, the ideal, 100% wet oxidation considered in the model can be difficult to achieve in the laboratory without considerable effort. Recognizing that 8.5 hours would be insufficient, the wafers were oxidized for approximately 20 hours at 1100°C under wet oxidation conditions. The weight of the wafer was measured before and after the oxidation. The weight gained during the oxidation can be used to estimate the resulting oxide thickness.

To calculate the oxide thickness via weight gain measurements, it is assumed that the total number of silicon atoms in the wafer does not change, and that all of the weight gain comes from oxygen atoms bonding with the silicon in the wafer to form an SiO_2 layer.

This means that the weight of the SiO_2 on the wafer, w_{ox}, is related to the measured weight gain, w_g, by:

$$w_{ox} = \left(1 + \frac{28.09}{2 \cdot 16.00}\right) \cdot w_g \qquad [3.1]$$

Where 28.09 and 16.00 are the atomic masses of silicon and oxygen, respectively. Additionally, it is assumed that the wafer is a perfect 2-inch diameter circle and that oxide growth on the edges can be neglected. This means that the thickness of the oxide layer on one side of the wafer, t_{ox}, can be determined by the using the density of SiO_2, ρ_{ox}, and w_{ox}.

$$t_{ox} = \frac{w_{ox}}{2 \cdot \rho_{ox} \cdot \pi \cdot r^2} \qquad [3.2]$$

The factor of two in the denominator comes from the fact that the oxide is grown on both sides of the wafer. The radius of the wafer is r. If ρ_{ox} is 2.2 grams per cubic centimeter, and r is 2.54cm, equations [3.1] and [3.2] can be combined and solved to give a relationship between w_g and t_{ox}:

$$t_{ox} = \frac{1.878 \cdot w_g}{89.18} = 0.02106 \cdot w_g \qquad [3.3]$$

where the units of t_{ox} are in cm, and w_g is in grams. Expressed in units of μm and grams, equation [3.3] is:

$$t_{ox} = 210.6 \cdot w_g \qquad [3.4]$$

As an SiO_2 layer is grown on a silicon surface, a certain thickness of the silicon is lost. A common rule of thumb is that the thickness of silicon consumed by the oxidation is 44% of the thickness of the final resulting oxide layer. This means that after the oxidation, the thickness of the wafer, t_w, is approximately:

$$t_w = 250 - 2 \cdot 0.44 \cdot t_{ox} = 250 - 185.3 \cdot w_g \qquad [3.5]$$

where the factor of two accounts for the fact the silicon is consumed from both surfaces. Again, the units for t_w are μm, and w_g is in grams, and a starting thickness for the wafer of 250μm is assumed.

A Thermco Mini Brute diffusion furnace was used to thermally oxidize the wafer. A heated bubbler containing deionized (DI) water was used to provide steam for the oxidation. Grade 5.0 oxygen (meaning "five-nines", or, 99.999% pure) was pumped through the bubbler and into the furnace at an approximate rate of 200 standard cubic centimeters per minute (sccm). MSU has recently acquired a PECVD system which can deposit oxides and nitrides at lower deposition temperatures, which in the future may be a better method of producing a masking layer for the silicon through etch due to both thermal budget considerations, as well as the possibility of an increased deposition rate.

Weight gain measurements showed that these growth conditions resulted in an oxide layer approximately 1.5μm thick. This is slightly less than the target oxide thickness, but was found adequate for masking purposes. As shown in Figure 3.2, the oxide was grown on both sides of the wafer.

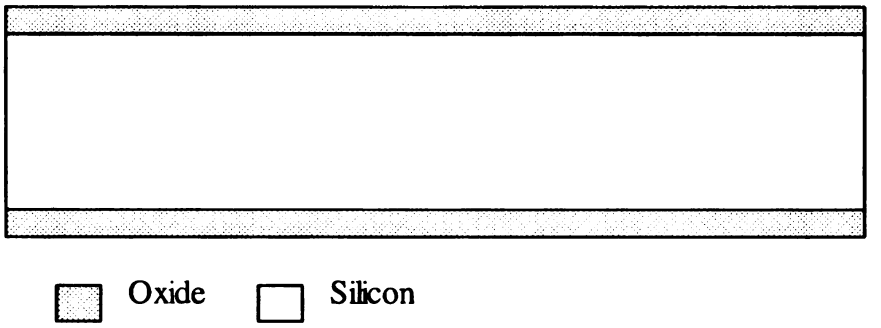

Figure 3.2 Cross-sectional view of the wafer after oxidation. Drawing not to scale.

3.2.3 Photolithography

After oxidation, one side of the wafer is patterned with an array of squares, each square measuring approximately 2mm by 2mm. The squares are aligned with the flat edge of the wafer in order to align the pattern with the atomic lattice of the silicon wafer.

The pattern on the wafer is created with Waycoat HR200 negative photoresist. Before the resist is applied to the wafer, the wafer is cleaned by spraying it with acetone for approximately 30 seconds, followed by a methanol spray for approximately 30 seconds, a DI water rinse for 2 minutes, and then blown dry by N_2. The wafer is then placed in a convection oven for a "bake-out" step at 200°C for 30 minutes to assure the surface is dry for good resist adhesion. After the bake-out, the wafer is placed on the resist spinner, coated with resist, and spun at 2000 rpms for 30 seconds. This corresponds to a pre-bake resist thickness of approximately 1μm. The coated wafer is then placed in a convection oven for a "pre-bake" procedure, which occurs at 65°C for 20 minutes.

After the pre-bake, the wafer is ready for exposure. A Karl Suss MJB-3 mask aligner equipped with a UV300 optical source was used. This optical source exposes the photoresist with wavelengths from 280 to 350nm. Exposure is in the soft-contact mode for approximately 10 seconds. The MJB-3 is capable of very high resolution (up to 0.4 microns in this configuration), but given the large feature sizes of the device constructed for this research, such high resolutions are not necessary in this case.

After exposure, the wafer is placed directly in the Waycoat negative photoresist developer solution. The wafer is agitated in this solution for 100 seconds. After the developer, the wafer is transferred to a beaker of xylene and agitated for approximately 20 seconds. The wafer is then placed in a beaker of isopropyl alcohol and again agitated for approximately 20 seconds, and then dried with blowing N_2. The wafer is next placed in a convection oven for a "post-bake" procedure, which occurs at 135°C for 15 minutes. After the post-bake, the wafer and pattern are ready for the oxide etch.

3.2.4 Oxide Etch

An oxide etch is performed after the photolithography process. The goal of the etching step is to transfer the pattern in the photoresist to the oxide, while also removing all of the oxide from the unpatterned side of the wafer. The etch solution was a 6:1 mixture of 40% NH_4F to 50% HF at room temperature. This solution etches the oxide at an approximate rate of 100nm per minute, so the etching time of 15 minutes was expected for the 1.5μm oxide layer. Since SiO_2 is hydrophilic and Si is not, the progress of the etch can be monitored by periodically removing the wafer from the etching solution,

submerging it in a beaker of water, and then removing the wafer and watching the behavior of the wafer as it streams off the wafer. When the oxide has been removed, the water will run off of the silicon rapidly and essentially completely, while when the wafer is still coated with oxide the water will 'sheet' and cling to the wafer. The oxide etch was terminated when observing the water indicated that the SiO_2 had been removed. Since the oxide etch solution is hazardous, after terminating the etch in a beaker of de-ionized (DI) water, the wafer was transferred to a second beaker of DI water to dilute any remaining etchant, next rinsed in running DI water for two minutes, and then dried with blowing N_2.

After the oxide etch, the photoresist has served its purpose and must be removed. A beaker containing Waycoat Microstrip photoresist remover is heated to 85°C on a hotplate. The wafer is placed in the heated solution for 10 minutes. The wafer is then sprayed with methanol for approximately 20 seconds, and then rinsed in running DI water for approximately 2 minutes. Finally, the wafer is blown dry with N_2. This procedure was used since the wafers for this research were processed in batches of 1 or 2 at a time. If larger batches of wafers were to be processed, a two-step procedure for stripping the photoresist may be appropriate.

Figure 3.3 shows a cross-sectional view of the wafer after etching the oxide and removing the photoresist.

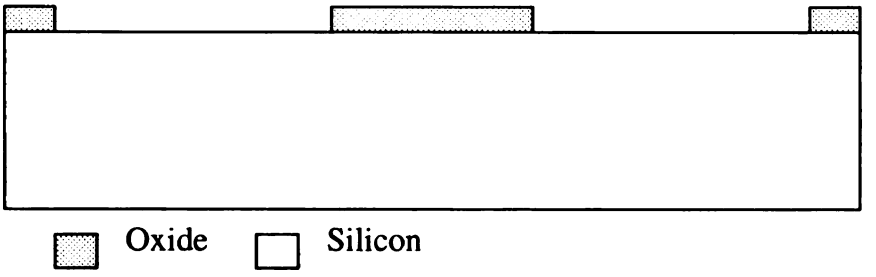

Figure 3.3 Cross section of the wafer after oxide etch and photoresist removal. Drawing not to scale.

3.2.5 Diamond Deposition

Various techniques for diamond deposition were explored at the beginning of this project. This included experiments in seeding, deposition chemistry, power and chamber configurations, and wafer sizes. What is described in this section was the procedure that resulted in the best optical properties of the diamond film and the resulting free-standing windows and Fabry-Perot resonators.

After etching and photoresist removal, one side of the wafer is bare silicon, while the other side has a patterned oxide. Figure 3.4 shows a photograph of the patterned oxide.

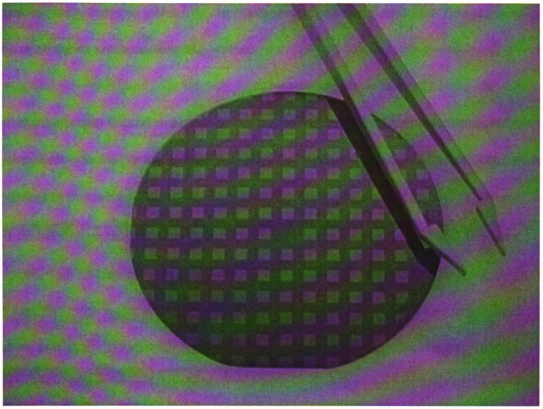

Figure 3.4 Patterned oxide on 2-inch diameter wafer

The wafer is then polish seeded for diamond film growth on the non-patterned side, and a diamond film is then deposited on that side of the wafer. The method used to seed the wafer was based on a method originally suggested by Windischmann, and later modified by Ulczynski[4]. Briefly, the wafer is cleaned in acetone, methanol, and then deionized water for 2 minutes each step. The wafer is then dried with blowing N_2. Next, the wafer is placed on a KimWipe and lightly dusted with diamond powder, which is then used to polish the wafer by hand for several minutes. The polishing procedure is to use a KimWipe to hold the wafer steady on the tabletop, while wrapping the index finger of the other hand with a KimWipe and using the index finger to wipe the diamond powder

across the surface of the wafer in a circular pattern for several minutes. Gloves should be worn at all times while seeding the wafer.

Both synthetic and natural diamond powders, all sourced from Amplex, were used for seeding, both showing good results, although the synthetic powder may have been more consistent in producing films that exhibit good optical properties. Both 0.25μm and 0.10μm maximum particle size diamond powders were used in natural and synthetic varieties, with no obvious advantage being seen with either size. When the polishing step was complete, the wafer was carefully wiped clean of any blemishes or marks visible to the eye, and again blown with N_2 to whisk away any small particles clinging to the wafer. This method differs from Ulczynski in that a final cleaning step has been omitted. The omission of the cleaning step seemed to have little impact on the wafers for purposes of this research, and shortened the seeding procedure significantly.

The diamond films were deposited using a Microwave Cavity Plasma Reactor (MCPR) of the Asmussen design, built at Michigan State University[5]. The particular system used in this research was developed to deposit diamond at relatively low temperatures, which allows films to be deposited on a wide array of substrates which may otherwise prove difficult to coat with diamond. The MCPR was configured in an end-feed style for this research. Ulcyznski[4] refers to this configuration as MCPR Configuration 7, and also details other configurations for this reactor, as well as giving an overview of various deposition conditions and results. The main variable in MCPR Configuration 7 is the height of a quartz ring which supports the substrate holder. For this research, a quartz

ring 59mm tall was used. The two user adjustable dimensions of the MCPR are the cavity length and the length that the probe protrudes into the cavity. For this work, typical cavity lengths were on the order of 21.5cm, and the typical probe insertion depths were on the order of 2.5cm. These values vary slightly depending on the plasma pressure and other deposition variables. These parameters are selected to minimize the reflected microwave power during the deposition. Figure 3.5 shows a cross-section of the wafer after the diamond deposition.

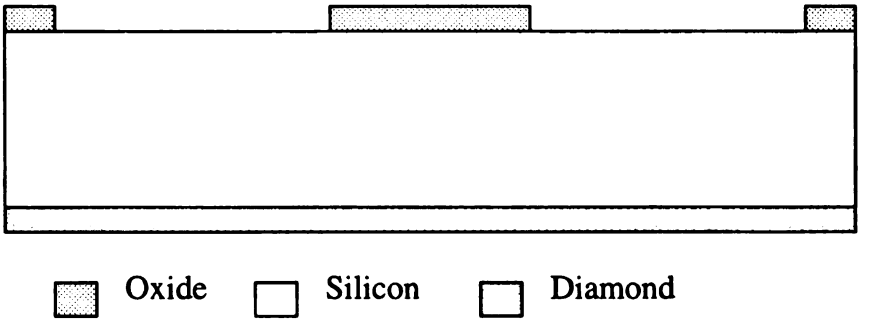

Figure 3.5 Cross section of wafer after diamond deposition. Drawing not to scale.

Diamond deposition parameters prove to be very critical not only to optical quality, but film integrity as well. Intrinsic stress in the film due to thermal mismatch is a large factor in the flatness and durability of the film[6]. The deposition was performed at 35 Torr, at a substrate temperature of approximately 660°C. This resulted in a flat membrane when the underlying silicon was etched away. Depositing at substantially lower temperatures and pressures would usually result in films that would wrinkle due to compressive stress, and in some cases break, at the completion of the subsequent silicon through-etch. Figure 3.6 shows a picture taken through an optical microscope of a window that wrinkled upon

completion of the through-etch, due to depositing the diamond at too low of a substrate temperature.

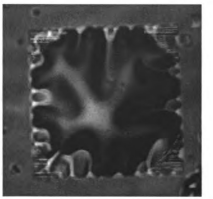

Figure 3.6 Wrinkled window resulting from low deposition temperature. This is an optical image taken with dark-field illumination.

At higher deposition temperatures, the windows would remain flat after the silicon had been etched away. Figure 3.7 shows a flat window taken under the same dark-field illumination as Figure 3.6. Since the window in Figure 3.7 is very flat compared to the window in Figure 3.6, the dark-field image is not very bright in this case.

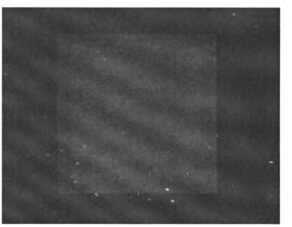

Figure 3.7 Flat window shown for comparison to Figure 3.6. This is an optical image taken with dark-field illumination.

An important parameter to the optical properties of the diamond film is the gas mixture used in the plasma. All of the working devices in this research were grown with 200 sccm of H_2, 8 sccm of CO_2, and 3 sccm of CH_4. This chemistry was found to produce windows which were very transparent, although the presence of CO_2 may lead to the slower growth rate than could otherwise be attained.

At the conditions used for this research, the thickness of the diamond film is observed to be non-uniform across the wafer as evidenced by the presence of many fringes in the film. However, a rough estimate of the film thickness, t_d, can be made by using the weight gained during the deposition, w_d, in an equation similar to [3.2]:

$$t_d = \frac{w_d}{\rho_d \cdot \pi \cdot r^2} \qquad [3.6]$$

where r is the diameter of the wafer, and ρ_d is the density of diamond. Using 3.51 grams per cubic centimeter for the density of diamond, and 2.54cm for the radius of the wafer, and changing the length units to micrometers, equation 3.6 can be rewritten as:

$$t_d = 140.6 \cdot w_d \qquad [3.7]$$

where t_d is again in units of micrometers, and w_d is in grams.

3.2.6 Silicon Through-Etch

After the diamond film deposition, the silicon wafer is through-etched using KOH to create the diamond membranes. Figure 3.8 shows a cross section of the wafer after the silicon through etch.

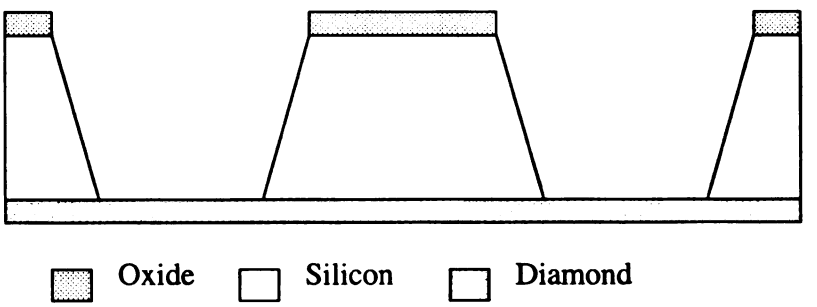

Figure 3.8 Cross section of the wafer after the silicon etch. Drawing not to scale.

The patterned oxide is used as a mask, while the diamond film has proven to be resilient to the KOH etch, thus serving as a mask on the second side of the wafer. The through-etch is performed at a temperature of 60°C, in a 44/56 weight percentage KOH/H_2O solution[7].

The literature[2,6,8,9] reports that the 44/56 solution etches (100) silicon at approximately 300 nm per minute. This corresponds to 18 μm per hour, for a total etching time of about 14 hours for a 250 μm thick wafer. In practice, it was observed that the etch would not start immediately, and proceeded slowly in the beginning, possibly due to the existence of a native oxide on the wafer, and the possibility of material left on the backside of the wafer from the diamond deposition. Actual etching times were around 18-20 hours to

etch completely through the wafer under these conditions. Another possible reason for the etch taking longer than expected is that the concentration of the KOH solution may not be constant for the duration of the etch. This phenomena is discussed briefly in a subsequent paragraph, along with a possible solution.

Figure 3.9 shows a schematic of the apparatus constructed for the KOH etch.

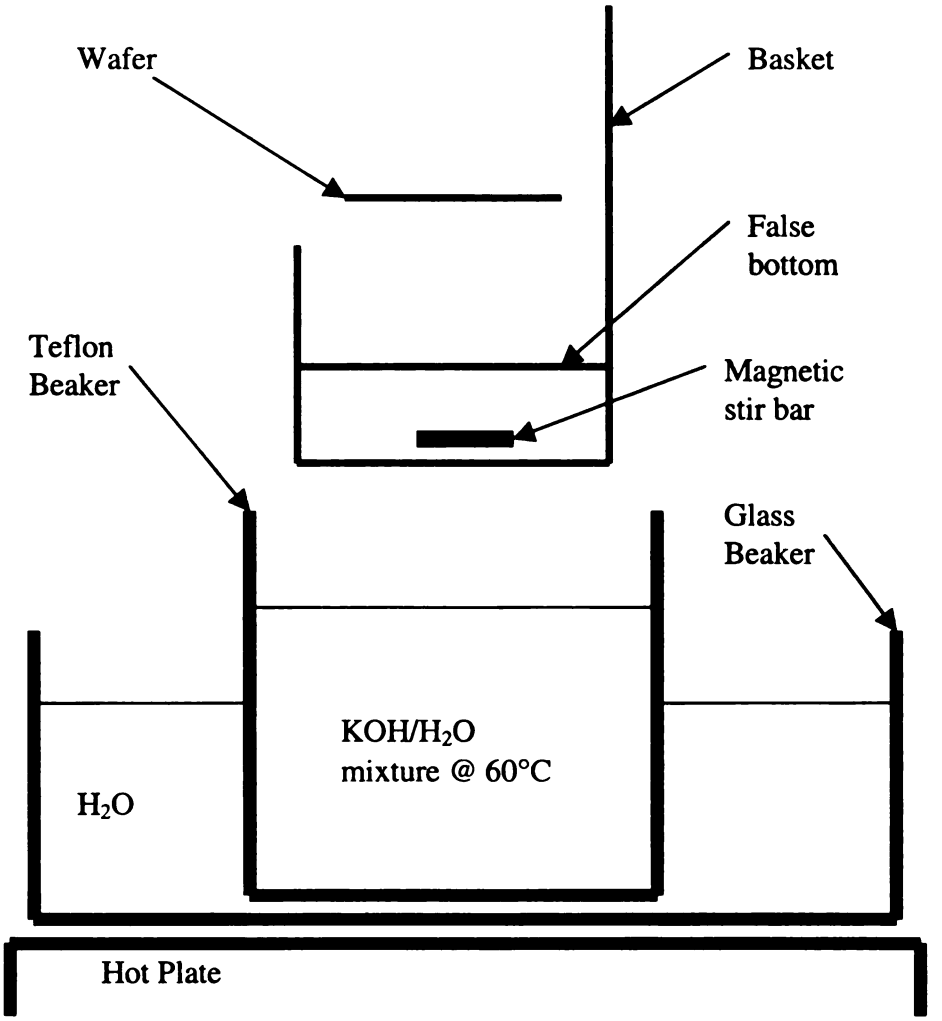

Figure 3.9 Schematic of the apparatus used for KOH etching of silicon.

The apparatus of Figure 3.9 takes into account several problems associated with the KOH etch. First, the etch must be maintained at approximately 60°C, and it must be contained in a plastic beaker, as it will slowly etch any sort of glass container. However, the plastic beaker cannot be placed on a hot plate as the temperature of the hot plate may become high enough to melt the plastic. Thus, the large water bath is used to assure that the plastic beaker will not see temperatures above 100°C. The Teflon beakers used in this research were rated to 121°C. It was observed that the KOH would gradually precipitate out of the mixture, and thus continuous stirring of the mixture is necessary. A standard plastic-coated magnetic stir bar was employed, but it necessitated a change to the way in which the wafer was held in the mixture. To this end, a false bottom was created in a plastic wafer processing basket, such that the stir bar could be located safely beneath the wafer. Once this apparatus was in place, the temperature of the etch was monitored with respect to the temperature control knob on the hot plate until a suitable setting was found. This corresponded to a water bath temperature of roughly 85°C, which lead to the KOH solution having the intended 60°C operating point.

The apparatus can be improved from the configuration employed in this research. Namely, a reflux condenser can be used to reduce the effects of evaporation on the solution. The solution can be observed to evaporate approximately 200mL over the course of the Si through-etch, which means that the 44/56 KOH/H_2O content of the mixture was not likely constant throughout the etching step.

When the diamond membrane is created by removing the silicon beneath it, the through transmission of the membrane is measured as described in the Optical Measurements section. The measurement step allows characterization of the particular window, namely the thickness of the film at that point, as well as the surface roughness. Figures 3.10 and 3.11 show photographs of clear, flat diamond windows at this phase of the fabrication sequence.

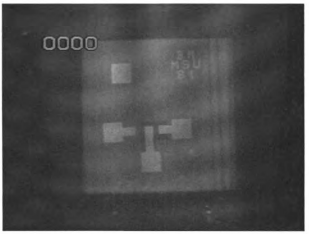

Figure 3.10 Looking through a clear diamond window onto a transistor (transistor shown for purposes of illustration only).

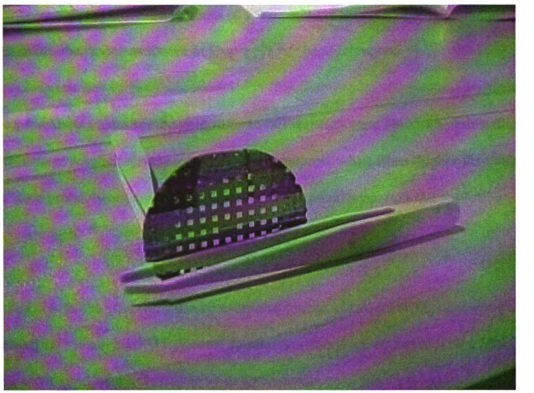

Figure 3.11 Holes seen in wafer are actually flat, transparent diamond windows.

3.2.7 Gold Sputtering

Once the diamond membranes are formed and measured, the final step is to sputter coat gold on both sides of the membrane. A commercial DC sputtering system used to conductively coat samples for scanning electron microscopy was used to apply the gold layer to the sample. A shadow mask is used to selectively coat the windows, instead of coating the entire wafer at once. The diamond film tends to have a rougher surface on the growth side as opposed to the silicon side of the film. The result is that the gold deposition on the growth side of the membrane has to be slightly thicker to form a continuous film. Experimentally, a ratio of 5/3 was determined for the thickness of the

gold film on the rough/smooth surfaces of the membrane for minimum gold thickness. At this point, the device as shown in Figure 3.1 has been fabricated.

Typical thickness values for the gold films in this research were 18-35nm. Films thicker than this range resulted in very low optical transmission, while films thinner than this range were probably not continuous, and thus their optical properties did not follow theory very well.

The thickness of the gold films can be estimated by one of two methods, depending upon the sputtering system used. First, some sputtering systems are equipped with a film thickness monitor, which directly provides some estimate of the thickness of the film being applied. A second method employed was to place a microscope slide next the diamond membrane in the sputtering system. Presumably, the thickness of the gold deposited on the slide would be almost the same as that deposited on the diamond membrane. The optical transmission through the slide can then be measured, and the gold thickness mathematically determined by fitting a simulation to the measurement.

3.3 Optical Measurements

The device is characterized in two steps. First, before the diamond membrane is sputter coated with gold, the through-transmission vs. wavelength is obtained for the diamond membrane only. This allows independent determination of the thickness and surface roughness of the particular window. Secondly, the transmission through the gold-coated resonator is measured.

3.3.1 Measurement Procedure

The optical through-transmission measurement is performed by passing a monochromatic beam of light through a particular diamond membrane or resonator, which is masked to block any light from passing through the silicon or other diamond membranes. The sample is placed in the system, and then carefully positioned for maximum power transmission through the system. The wavelength is varied and the transmitted power and the wavelength value at each wavelength of interest are recorded. The sample is then removed from the optical system, and a mask with the same size opening as was used on the sample is placed in the path of the beam. The monochromator is returned to the wavelength noted during the positioning of the sample in the system, and again the position of the mask is chosen for maximum power transmission through the system. The power of light passing through the mask with no sample is then recorded for each wavelength. The "sample" data is then normalized against the "air" data to obtain an accurate value for percent transmission through the sample.

3.3.2 Measurement Apparatus

Three different monochromators were used during the course of this research to document optical transmission as a function of wavelength: a Bausch & Lomb High Intensity Grating Monochromator, a Beckman IR 4200 Infrared Spectrometer, and a Perkin Elmer Lambda 9000 Monochromator.

Figure 3.12 shows a diagram of the experimental set-up used with the Bausch & Lomb monochromator, which was used for the bulk of optical measurements. It consists of a light source and monochromator, an adjustable aperture, two lenses, a sample holder, and an optical power detector and meter. A Bausch & Lomb Tungsten Light Source is coupled to a Bausch & Lomb High Intensity Monochromator, with an optical filter in the middle to eliminate higher order spectra. Different monochromator and filter combinations are available to span the visible wavelengths into the near IR. There are two monochromator gratings used in this setup, called "VIS" and "IR-1". Three filters are employed, Corning C.S. Number 3.74 which cuts off wavelengths below 400nm, Corning C.S. Number 2.56 which cuts off wavelengths below approximately 600nm, and Corning C.S. Number 7.56 which cuts off wavelengths below 800nm. The VIS grating used with the 3.74 filter spans wavelengths from 420nm – 760nm. The IR1 grating combined with the 2.56 filter goes from 700nm – 1050nm. The IR1 grating combined with the 7.56 filter spans the range of 1000nm to 1600nm.

The monochromator allows the user to change the entrance and exit slits, which is a trade-off between how monochromatic the beam is, and the beam intensity. For this

research, the narrowest slit widths were selected, 0.75mm, giving the most monochromatic beam available from this particular setup (4.8nm for the VIS grating and 9.6nm for the IR1 grating), at the expense of some intensity. Even at the reduced beam intensity, sufficient power reaches the detector to give good results.

The optical power transmitted through the sample is measured using a Newport 835 Optical Power Meter. Two different detectors are used in conjunction with this meter, depending upon the wavelength being measured. The Newport 818-SC silicon detector is used from the visible up to 1050nm in wavelength, and the 818-IR germanium detector is used from 1000-1600nm.

To avoid the effects of stray light getting to the detector and offsetting the reading, the measurement apparatus, from the monochromator to the optical power detector, is placed under a cover during measurements, and the room lights are turned off. Additionally, the apparatus is carefully checked to make sure that as much of the beam as possible is going through the sample, and the remainder of the beam is blocked so that there are no alternate paths to the detector.

The beam exiting the monochromator is first incident upon an adjustable aperture, which is used to tailor the spot size of the beam to the physical dimensions of the diamond membrane or resonator, as well as block any of the beam that would not be properly incident upon the first lens in the system. The first lens focuses the beam to a small spot so that almost the entire beam can pass through the small hole in the sample. The beam

is then incident upon a second lens, which focuses the beam onto the active area of the detector.

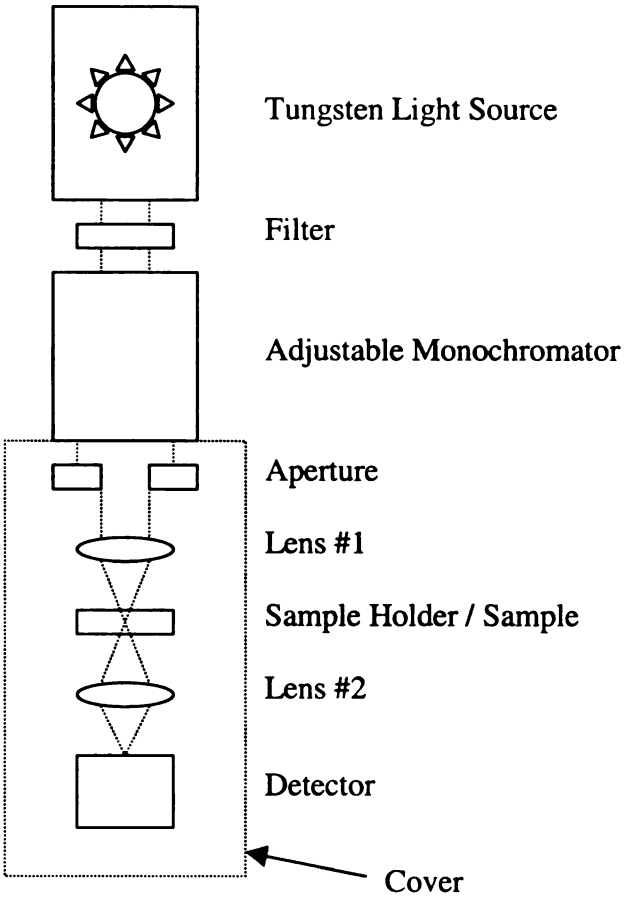

Figure 3.12 Diagram of the optical measurement apparatus constructed for this research.

The two other spectrometers used for this research are both prefabricated, commercial grade units. Both the Perkin Elmer and Beckman instruments are automated and offer the user little direct control of sources, gratings, filters, or slit widths. Both instruments perform dual beam measurements, and each instrument offers computerized data collection.

The two commercial instruments have a large spot size compared to the dimensions of the diamond windows constructed for this research. This can make getting good optical transmission data difficult since a very large portion of the beam's power is blocked by the mask, and thus the signal to noise ratio is increased accordingly.

3.4 Atomic Force Microscopy (AFM)

An AFM was used in this research to examine the surface of the diamond films. Data from the AFM can give an indication of grain size, roughness, and the statistical nature of the roughness. For this research, a Digital Instruments Nanoscope III AFM was used to characterize certain samples. This instrument is capable of imaging atomic level features, as well as operating as a Scanning Tunneling Microscope (STM). The instrument requires that the sample be mounted on a 1cm diameter disk, so for this research, the samples must be broken into smaller pieces to be imaged by this AFM. STM mode requires a conductive sample, and was not used for this research.

3.5 Scanning Electron Microscopy (SEM)

At certain points in this research, SEM images were used to evaluate fabrication sequences. For this research, a Japan Electron Optics Laboratories (JEOL) 6400 SEM was used. This particular SEM is equipped with a lanthanum hexaboride (LaB6) electron source, and has a maximum magnification of 300,000. Such high magnifications are not necessary for evaluation of the features found in this research, however. The SEM

requires that the sample be mounted on either a 1-inch diameter or 0.25-inch diameter aluminum stub for insertion into the SEM. This means that the 2-inch wafer must be broken into smaller pieces to examine with the SEM. Typically, non-conductive samples must be gold coated for SEM imaging, although it was observed that for moderate accelerating voltages of around 20kV or less, the samples for this research did not need to be coated to produce acceptable images, but that coating made images somewhat easier to obtain.

3.6 Summary

In this chapter, the fabrication sequence was explained and documented, as well as the characterization steps. The through-etch of the wafer places some requirements on earlier sequences, namely the lithography and oxidation. Additionally, the fabrication sequence must be interrupted to characterize the device optically. Three methods for optical characterization are described. Also, SEM and AFM methods for determining morphology and evaluating fabrication sequences are discussed.

References:

[1] W. Kern and D. A. Puotinen, "Cleaning Solutions based on Hydrogen Peroxide for use in Silicon Semiconductor Technology", RCA Review, 187-206, June 1970

[2] K. E. Bean, "Anisotropic Etching of Silicon", IEEE Trans. Electron Devices, ED-25, 1185-1193, 1978.

[3] Stephen A. Campbell, The Science and Engineering of Microelectronic Fabrication, Oxford University Press, 1996

[4] M. Ulczynski, Low-Temperature Deposition of Transparent Diamond Films with a Microwave Cavity Plasma Reactor, PhD Dissertation, Michigan State University, (1998).

[5] K. P. Kuo and J. Asmussen, "An Experimental Study of High Pressure Synthesis of Diamond Films using a Microwave Plasma Reactor", Diamond Relat. Mater. 6, 1097-1105, 1997.

[6] H. Windischmann, G. F. Epps, Y. Cong, and R. W. Collins, "Intrinsic Stress in Diamond Films Prepared by Microwave Plasma CVD", J. Appl. Phys., February 1991 PP 2231-2237.

[7] D. L. Kendall, "Vertical Etching of Silicon at Very High Aspect Ratios", Ann. Rev. Mater. Sci., Vol. 9, 373-403, 1979.

[8] K. E. Bean and W. R. Runyan, J. Electrochem. Soc., Vol. 124 5c-12c, 1977.

[9] M. Josse, D. L. Kendall, "Rectangular-profile diffraction grating from single-crystal silicon ", Applied Optics, Vol. 19, Issue 1, p.72, January 1980.

Chapter 4: Modeling Approach

4.1 Introduction

This chapter describes the modeling of the transmission properties of the Fabry-Perot device to extract physical parameters from measurements, to predict the performance of the device, and to guide the actual fabrication of the device. The chapter details the modeling used in this thesis, on both a mathematical level, as well as discussing the MATLAB code used to implement the mathematical model devised.

4.2 Motivation for Developing a Different Model

The goal of the model developed for this research is to incorporate the effect of surface roughness into the matrix model for one-dimensional transmission through multi-layered optical structures. The treatment of surface roughness in this research neglects near field effects and is based on a superposition of plane waves. The generally good match between the model presented here and the measurements taken for this research shows that this approach can lead to meaningful results. Chapter 2 showed two different matrix models for calculating transmission through a multilayer structure. Either approach can be modified to include surface roughness effects in the simulation, although this chapter will rely primarily upon the transfer matrix technique for the mathematical development of the model.

Before showing the model developed for this research for multilayer structures, it is of interest to note that a result in the literature is based on an incorrect use of Filinski's results for a single interface. The development of this model illustrates this point, as well as setting the stage for development of the model devised for this research. First, consider the case of a smooth slab with no surface roughness. Figure 4.1 shows a smooth slab with thickness d and index of refraction n_1 separating two semi-infinite materials with indices of refraction n_0 and n_2.

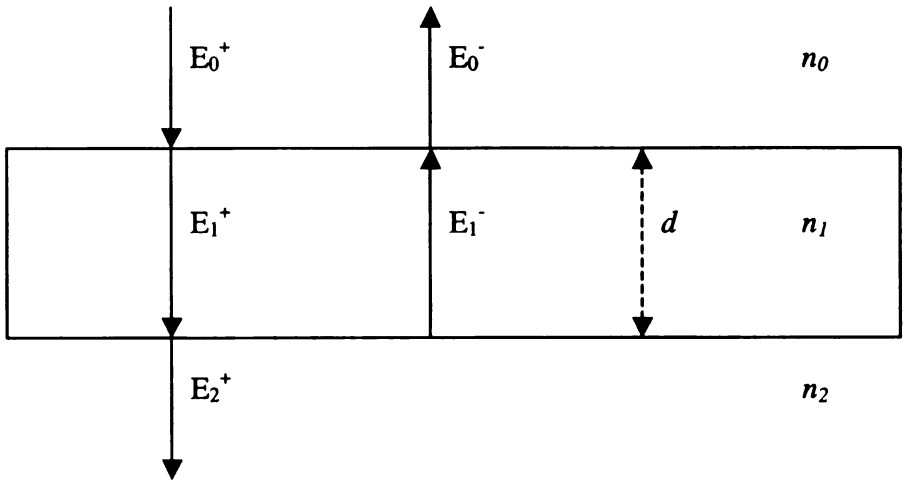

Figure 4.1 a smooth slab

The incident electric field is shown as E_0^+, and the reflected field from the slab is E_0^-. The transmitted field is shown as E_2^+. Using the transfer matrix approach[1,2,3], detailed in Chapter 2, for the case of smooth surfaces, the relationship between E_0^+, E_0^-, and E_2^+ is found from equation [2.83] to be:

$$\begin{bmatrix} E_0^+ \\ E_0^- \end{bmatrix} = S \begin{bmatrix} E_2^+ \\ 0 \end{bmatrix} \qquad [4.1]$$

Where the transfer matrix S is found by:

$$S = \left(\frac{1}{t_{01}}\right)\begin{bmatrix} 1 & -r_{10} \\ r_{01} & t_{01}t_{10} - r_{01}r_{10} \end{bmatrix}\begin{bmatrix} e^{i\phi_1} & 0 \\ 0 & e^{-i\phi_1} \end{bmatrix}\left(\frac{1}{t_{12}}\right)\begin{bmatrix} 1 & -r_{21} \\ r_{12} & t_{12}t_{21} - r_{12}r_{21} \end{bmatrix} \quad [4.2]$$

with

$$\phi_1 = \frac{2\pi n_1 d}{\lambda} \quad [4.3]$$

Using equations [4.1]-[4.3], the field transmission can be found as:

$$\frac{E_2^+}{E_0^+} = \frac{t_{01}t_{12}}{e^{i\phi_1} - r_{12}r_{10}e^{-i\phi_1}} \quad [4.4]$$

Which leads to the well known equation for power transmission through a single thin layer:

$$T = \frac{(t_{01})^2(t_{12})^2}{1 + (r_{12})^2(r_{10})^2 - 2r_{12}r_{10}\cos(2\phi_1)} \quad [4.5]$$

In the literature[4,5,6,7], equations [4.4] and [4.5] have been modified by multiplying the electric field reflection term, r_{10}, and transmission term, t_{01}, by the square root of the Filinski correction factors, equations [2.98] and [2.106], in order to simulate transmission through a thin slab with surface roughness on one side:

$$T_R = \frac{t_{12}^2 t_{01}^2 e^{-\left(\frac{2\pi\sigma(n_0 - n_1)}{\lambda_0}\right)^2}}{1 + r_{12}^2 r_{10}^2 e^{-\left(\frac{4\pi\sigma n_1}{\lambda_0}\right)^2} - 2r_{12}r_{10}e^{-\frac{1}{2}\left(\frac{4\pi\sigma n_1}{\lambda_0}\right)^2}\cos(2\phi_1)} \quad [4.6]$$

Alternatively, the square root of the Filinski exponential terms have also been used to modify the Fresnel coefficients in equation [4.2] for the first interface[4,5]. This has also

been suggested as a general method of including the effects of interface roughness into the problem of multilayer optics, and also leads to equation [4.6].

However, equation [4.6] does not accurately account for the phase of the wave inside the film. The Filinski correction terms are based on the integration of equation [2.103] being carried out over two semi-infinite media with a single interface. The situation is different for a thin film between two semi-infinite media because of the effect of the second interface. For this case, as well as the case of multiple layers, a numerical integration approach must be used, described as follows.

4.3 Model Developed for this Research

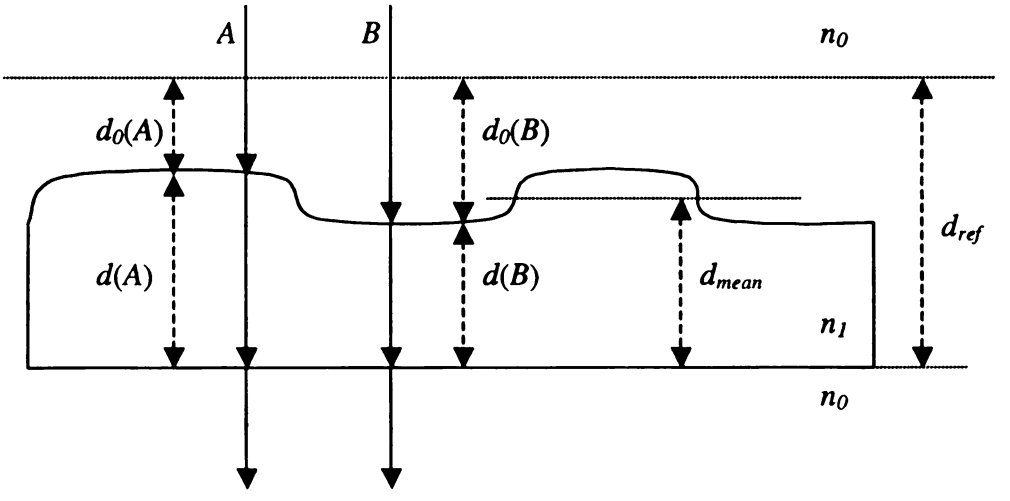

Figure 4.2 Two paths through a rough thin film

Figure 4.2 shows two paths through a thin film with surface roughness on one side. Normal incidence is assumed. The roughness of the layer is assumed to be Gaussian in nature with zero correlation length, and with a mean value of the film thickness d_{mean}. The length of the optical path through the film is denoted by d, and since the two paths shown in the figure are of different lengths, they are denoted as $d(A)$ and $d(B)$. A plane in space above the rough surface is chosen as a reference, located d_{ref} above the second, smooth surface of the thin layer. The distance from this plane to the rough surface, d_0, is also a function of the path length through the layer. Thus the two lengths are labeled $d_0(A)$ and $d_0(B)$. For any path through the slab,

$$d(\text{path } n) + d_0(\text{path } n) = constant = d_{ref} \qquad [4.7]$$

where d_{ref} is independent of path through the sample. The transfer matrix technique can now be applied to this system, and the transmission through (or reflection from) the slab can be calculated.

In Figure 4.2, a phantom layer of thickness d_0 is essentially created to account for the phase change in the wave as it travels from the reference plane to the actual interface. Since there is not an actual interface at the reference plane, the transmission is equal to unity, and the reflection is zero. However, the wave travels through a distance d_0 resulting in a phase change, ϕ_0, of:

$$\phi_0 = \frac{2\pi n_0 d_0}{\lambda} \qquad [4.8]$$

Thus, the transfer matrix of the system, S, can be found by:

$$S = \begin{pmatrix} 1 \\ 1 \end{pmatrix} \begin{bmatrix} 1 & 0 \\ 0 & 1 \end{bmatrix} \begin{bmatrix} e^{i\phi_0} & 0 \\ 0 & e^{-i\phi_0} \end{bmatrix} \begin{pmatrix} 1 \\ t_{01} \end{pmatrix} \begin{bmatrix} 1 & -r_{10} \\ r_{01} & t_{01}t_{10} - r_{01}r_{10} \end{bmatrix} \begin{bmatrix} e^{i\phi_1} & 0 \\ 0 & e^{-i\phi_1} \end{bmatrix} \cdots$$
$$\cdots \begin{pmatrix} 1 \\ t_{12} \end{pmatrix} \begin{bmatrix} 1 & -r_{21} \\ r_{12} & t_{12}t_{21} - r_{12}r_{21} \end{bmatrix} \qquad [4.9]$$

The transfer matrix can be simplified to:

$$S = \frac{1}{t_{01}t_{12}} \begin{bmatrix} e^{i\phi_0}e^{i\phi_1} - r_{10}r_{12}e^{i\phi_0}e^{-i\phi_1} & * \\ * & * \end{bmatrix} \qquad [4.10]$$

Where only the (1,1) element of S is shown, since it alone determines transmission through the layer. The fraction of the field transmitted is related to the inverse of this element as:

$$\frac{E_2^+}{E_0^+} = t = \frac{t_{01}t_{12}}{e^{i\phi_0}e^{i\phi_1} - r_{10}r_{12}e^{i\phi_0}e^{-i\phi_1}} \qquad [4.11]$$

Following the procedure which lead to equation [2.103], a mean ratio of E_2^+/ E_0^+ can be calculated by considering a Gaussian distribution of layer thickness, d. This results in the expression:

$$\left\langle \frac{E_2^+}{E_0^+} \right\rangle = \int_{-\infty}^{\infty} t(d)w(d)d(d)$$
$$= \frac{t_{01}t_{12}e^{-i\frac{2\pi}{\lambda}n_0 d_{ref}}}{\sigma\sqrt{2\pi}} \int_{-\infty}^{\infty} \frac{e^{-\frac{(d-d_{mean})^2}{2\sigma^2}}}{e^{i\frac{2\pi d}{\lambda}(n_1-n_0)} - r_{10}r_{12}e^{-i\frac{2\pi d}{\lambda}(n_0+n_1)}} d(d) \qquad [4.12]$$

where σ is the RMS value of the surface roughness. Note that d_0 has vanished, commensurate with its creation as the thickness of a phantom layer, and that when equation [4.12] is multiplied by its complex conjugate, the term containing d_{ref} will also

vanish. If equation [4.12] is used in equation [2.105] to calculate the transmitted power, the result is different than equation [4.6].

Figure 4.3 shows the results of using equation [4.12] in equation [2.105] to solve for transmission, as well as a plot of equation [4.6] for the same system. The system shown in the figure is a 1μm thick slab of diamond with 20nm RMS surface roughness on one side, with semi-infinite media on either side of the slab with index of refraction equal to one.

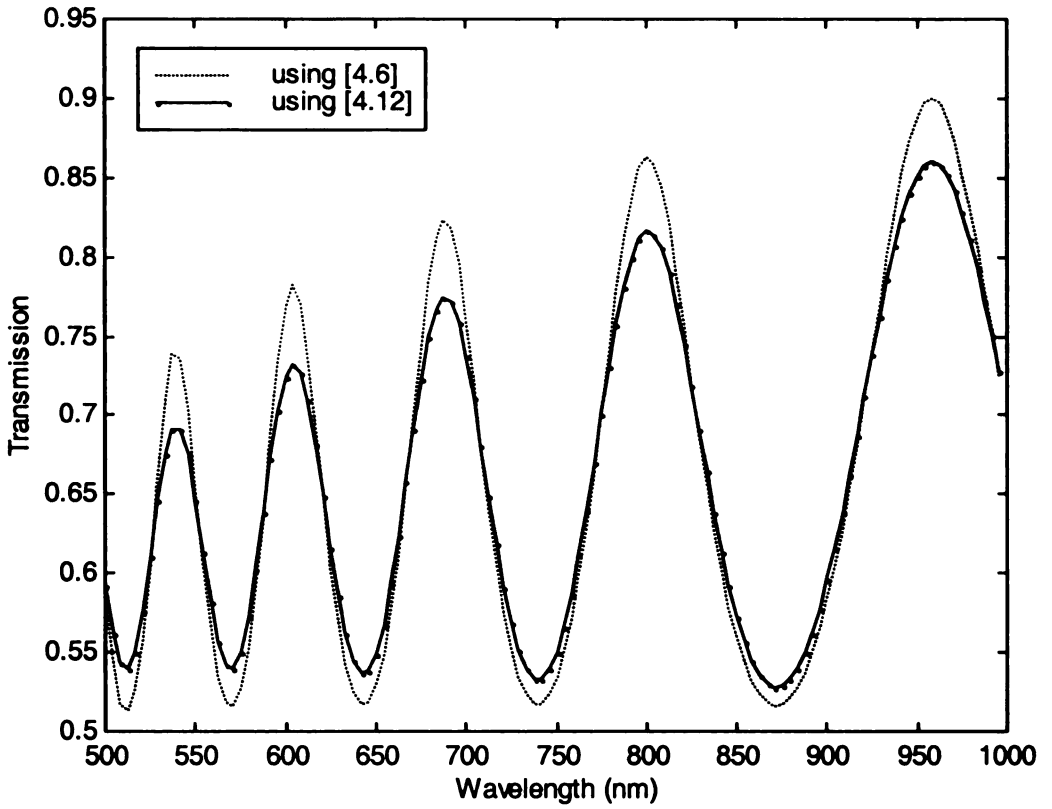

Figure 4.3 Two transmission plots for a rough diamond slab. In both cases, thickness = 1μm, roughness = 20nm. The difference between using the approach of equation [4.6] and that of using [4.12] is readily apparent.

4.4 Extension to Multiple Layers

The concept shown in the previous section of creating a phantom layer and solving equations [4.12] and [2.105] can be applied to multilayer systems. To do so, matrices corresponding to additional layers are inserted in equation [4.9] while retaining the phantom layer and ordering the matrices appropriately for the physical system being modeled.

Here, an example is shown of how to write the transfer matrix for a system that includes one rough interface in a multilayer stack.

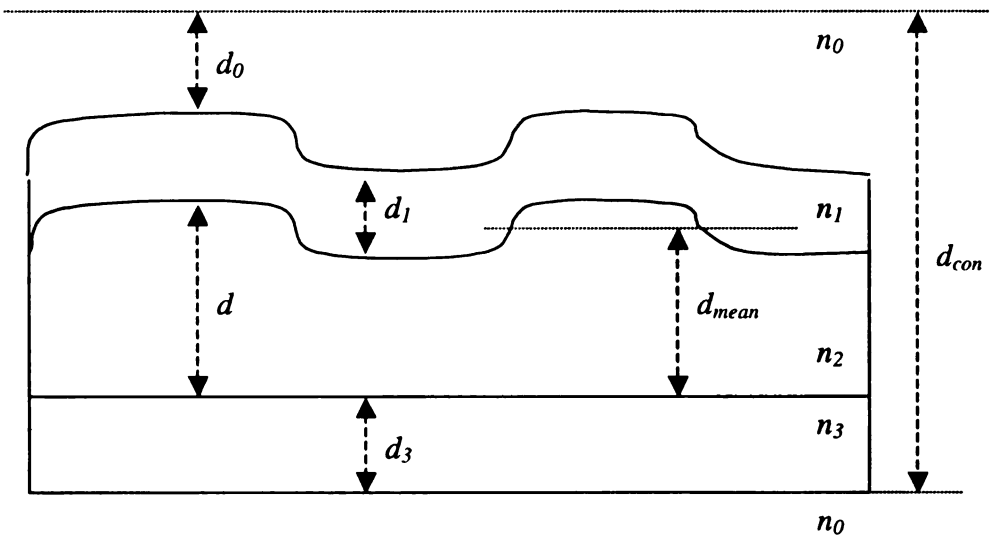

Figure 4.4 A multilayer structure with a rough interface

Figure 4.4 shows a multilayer structure with roughness at one interface, surrounded by two semi-infinite media. The layer with surface roughness is represented by index of refraction n_2, and the layer with index of refraction n_1 coats the n_2 layer conformally, so the roughness is seen at the surface of the structure as well. The layer with index of refraction n_3 is assumed to have smooth interfaces on both sides.

The transfer matrix S for this system is then:

$$S=\begin{bmatrix} e^{i\phi_0} & 0 \\ 0 & e^{-i\phi_0} \end{bmatrix}\left(\frac{1}{t_{01}}\right)\begin{bmatrix} 1 & -r_{10} \\ r_{01} & t_{01}t_{10}-r_{01}r_{10} \end{bmatrix}\begin{bmatrix} e^{i\phi_1} & 0 \\ 0 & e^{-i\phi_1} \end{bmatrix}\cdots$$
$$\cdots\left(\frac{1}{t_{12}}\right)\begin{bmatrix} 1 & -r_{21} \\ r_{12} & t_{12}t_{21}-r_{12}r_{21} \end{bmatrix}\begin{bmatrix} e^{i\phi_2} & 0 \\ 0 & e^{-i\phi_2} \end{bmatrix}\left(\frac{1}{t_{23}}\right)\begin{bmatrix} 1 & -r_{23} \\ r_{32} & t_{23}t_{32}-r_{23}r_{32} \end{bmatrix}\cdots \quad [4.13]$$
$$\cdots\begin{bmatrix} e^{i\phi_3} & 0 \\ 0 & e^{-i\phi_3} \end{bmatrix}\left(\frac{1}{t_{30}}\right)\begin{bmatrix} 1 & -r_{03} \\ r_{30} & t_{30}t_{03}-r_{30}r_{03} \end{bmatrix}$$

where ϕ_0 is taken from equation [4.3], ϕ_1 , ϕ_2, and ϕ_3 are the phase shifts corresponding to the layers which they represent. The (1,1) element of this matrix can be determined, and an integral corresponding to equation [4.12] can be generated and solved numerically to calculate the field transmission. Equation [2.105] can then be employed to find the transmitted power of the system.

One can also use MacLeod's technique to calculate transmission through the structure in Figure 4.4. Under the same assumptions and definitions that lead to equation [4.13], the transmission using the MacLeod technique would be calculated by using the matrix:

$$\begin{bmatrix} B \\ C \end{bmatrix}=\begin{bmatrix} \cos\delta_0 & \frac{i}{n_0}\sin\delta_0 \\ in_0\sin\delta_0 & \cos\delta_o \end{bmatrix}\begin{bmatrix} \cos\delta_1 & \frac{i}{n_1}\sin\delta_1 \\ in_1\sin\delta_1 & \cos\delta_1 \end{bmatrix}\cdots$$
$$\cdots\begin{bmatrix} \cos\delta_2 & \frac{i}{n_2}\sin\delta_2 \\ in_2\sin\delta_2 & \cos\delta_2 \end{bmatrix}\begin{bmatrix} \cos\delta_3 & \frac{i}{n_3}\sin\delta_3 \\ in_3\sin\delta_3 & \cos\delta_3 \end{bmatrix}\begin{bmatrix} 1 \\ n_0 \end{bmatrix} \quad [4.14]$$

where δ_n is calculated according to equation [2.44], using the appropriate thickness and index of refraction for the layer in question. When the matrix in equation [4.14] is calculated, it can be used to calculate the field transmission with the following equation[8]:

$$t=\frac{2n_0}{n_0B+C} \quad [4.15]$$

The field transmission can then be used in equation [4.12] to find the field transmission of the system considering surface roughness. Equation [2.105] is then used to find the transmitted power of the system.

4.5 Applying the Model

Appendix A shows the MATLAB code for a program named modexamp.m. The goal of the model is to produce a plot of transmission versus wavelength. This program will be used to illustrate how the model works and the effects that various parameters have on the output. This program simulates transmission through a thin slab of material with roughness on one interface and numerically solves the integral problem for multilayered structures as setup previously in section 4.3. It uses the MacLeod style matrix method instead of the transfer matrices used to show the development of the model.

The numerical approximation of the integration gives rise to some parameters which are not present in the analytical formulation of the problem. Typically, the selection of these parameters involves a trade-off between accuracy of the simulation and computational time for the simulation.

4.5.1 Setting Up the Variables

The program opens with the code (comments omitted here):

```
clear
dnom=1.0*10^-6;
n1=1;
n3=1;
```

The nominal thickness of the diamond layer is given by *dnom*. The units here are meters. The indices of refraction for the two semi-infinite media are *n1* and *n3*. Here, they are chosen to be unity, corresponding to free-space.

4.5.2 The Gaussian Distribution

For this thesis, the surface roughness at the material interface is first modeled as following a Gaussian distribution. The program can be modified to model the roughness by any distribution. However, Gaussian distributions are often considered a good first approximation for many processes if the exact distribution is not known. In fact, as shown in Chapter 6 with AFM measurements, most of the PECVD films in this study indeed do exhibit essentially a Gaussian distribution in their surface roughness. The issue of deviations from a Gaussian distribution is treated later.

The form of the continuous first order Gaussian distribution without higher order terms is given by equation [2.94] and repeated here:

$$w_c(z) = \frac{1}{\sigma\sqrt{2\pi}} e^{-\frac{z^2}{2\sigma^2}} \qquad [4.16]$$

The subscript c is to emphasize that this is for a continuous distribution. It should be noted that this expression is for z having a mean value of zero. If z instead has a mean value of z_0, the expression changes to:

$$w_c(z) = \frac{1}{\sigma\sqrt{2\pi}} e^{-\frac{(z-z_0)^2}{2\sigma^2}} \qquad [4.17]$$

The distribution $w_c(z)$ can be interpreted in the following manner: the probability of finding z between z_1 and z_2 is expressed as:

$$p = \int_{z_1}^{z_2} w_c(z)dz \qquad [4.18]$$

The distribution $w_c(z)$, as expressed here, is normalized. That is, if it is integrated from z=-∞ to ∞, the result is exactly equal to one. This can be interpreted as meaning that the probability of $w(z)$ taking on some value between -∞ and ∞ is 100%. This is important, because the thickness of the diamond films will be modeled by a Gaussian distribution in this thesis. At any every position on the film, the thickness must have some value. As expression [2.15] stands, it leaves open the unphysical possibilities of a negative film thickness, as well as nearly infinite film thicknesses. However, the nature of using the matrix model to solve the transmission through the structure can easily eliminate these unphysical possibilities, due to the fact that a discrete version of the Gaussian distribution must be used.

A discrete Gaussian distribution with j possible values of z can be calculated by:

$$w'(i = 1 \cdots j) = e^{-\frac{(z_i - z_0)^2}{2\sigma^2}} \qquad [4.19]$$

However, this expression is not normalized. It can be easily normalized by calculating the normalization coefficient c_N :

$$c_N = \sum_{i=1}^{j} w'(i) \qquad [4.20]$$

Thus the normalized expression for this discrete Gaussian is:

$$w(i = 1 \cdots j) = \frac{1}{c_N} e^{-\frac{(z_i - z_0)^2}{2\sigma^2}} \qquad [4.21]$$

Interpreting the meaning of the discrete Gaussian distribution is different than for the continuous case. The probability of finding $z=z_i$ is simply $w(i)$.

The *modexamp.m* MATLAB program listed in Appendix A carries out the calculation and normalization of the distribution of thicknesses with the following loop:

```
for n=1:dpp+1;
     d(n)=dstart+((n-1)*incrp);
     term1=((d(n)-dnom)^2)/(2*(sigma^2));
     dt(n)=exp((-1)*term1);
     nm=nm+dt(n);
end
dt=dt./nm;
```

The loop contains some parameters which thus far have not been mentioned.

The number of terms calculated in the distribution is determined by *dpp*. For this work, a typical range of values for *dpp* is 20 to 40. Figure 4.5 shows the error between subsequent simulations as a function of *dpp* for typical values of surface roughness observed in this work. A point on this curve is calculated by, for example, calculating the n_0 point transmission curve for dpp=3 and again for dpp=4. The value of the error at

dpp=3 is then found by summing the squares of the differences between the two transmission curves. Mathematically, this can be expressed as:

$$Error(dpp) = \sum_{n=1}^{n_0} \left[T_{dpp+1}(n) - T_{dpp}(n)\right]^2 \qquad [4.22]$$

Thus, the smaller the error becomes, the less impact additional terms in the Gaussian distribution contribute to the calculated transmission.

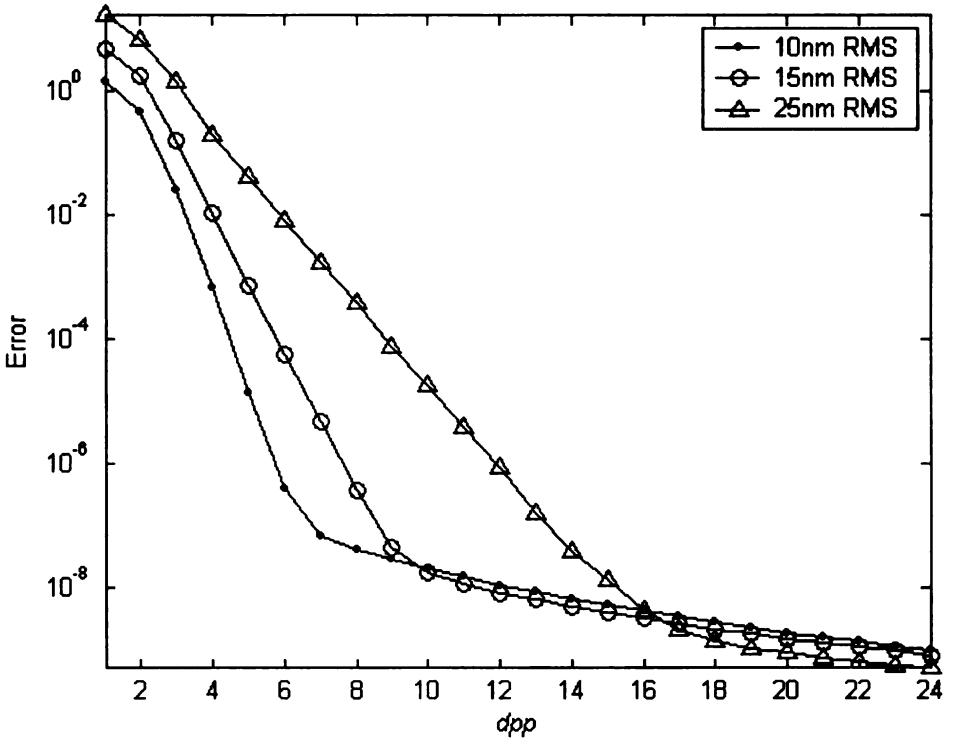

Figure 4.5 Simulation Error as a function of *dpp*.

As can be seen from Figure 4.5, for each value of surface roughness, the curve changes slope at some point, indicating a regime of decreasing return in accuracy as *dpp* increases. Thus for this work, all simulations use *dpp* values of at least 20. Simulation

time increases with *dpp*, so a plot such as Figure 4.5 can be useful in minimizing simulation time.

Returning to the parameters in the MATLAB code, the nominal value of the film thickness is given by *dnom*.

The parameters *dstart* and *incrp* require slightly more explanation. Since there are only a finite number of points in the discrete distribution, it will span only a certain range of layer thicknesses. In the program, this range is the distance from *dstart* to *dstop*, which are calculated based upon *dnom* and *sigma*. For this research, the range spanned by the distribution is chosen to be a simple function of the RMS surface roughness, σ. The starting point of the distribution, and the increment between points are calculated by the following lines of code:

```
dstart=dnom-(4*sigma);
dstop=dnom+(4*sigma);
dpp=10;
incrp=(dstop-dstart)/dpp;
```

As mentioned previously, the nature of having non-infinite start and end points to the distribution adds physical reality to the model based on the film characteristics. The units of *dstart*, *dstop*, *dnom*, *incrp*, and *sigma* are all meters.

The use of the distribution that the program calculates will be discussed in more detail later, but for now, it may add clarity to say that the distribution of layer thicknesses will

be calculated, then the transmission through each thickness will be calculated, and finally the transmissions summed in a weighted manner with respect to the distribution. This weighted summation is a numerical approximation to the integral in equation [2.12].

4.5.3 Calculating the Transmission

The transmission is calculated with a loop on a variable representing the wavelength. There is first a small set of code to set up some variables for the loop.

```
numpoints=400;
lamstart=400*10^-9;
lamstop=1600*10^-9;
incr=(lamstop-lamstart)/numpoints;
```

The variable *numpoints* contains the number of data points that will be calculated along the wavelength axis. This number should be selected to generate a smoothly varying transmission vs. wavelength plot. For a given film thickness, the wider the range of wavelengths considered the more fringes will appear in the transmission. Also, thicker films will have more fringes in a given range of wavelengths, and thus it is appropriate to scale *numpoints* approximately with film thickness and range of wavelength. For the range of film thicknesses and wavelengths considered in this thesis, a typical value of *numpoints* that yields a smooth looking transmission curve is from 300 to 400. More points can be calculated, but the simulation time increases accordingly.

The variables *lamstart*, *lamstop*, and *incr* are analogous to the variables *dstart*, *dstop*, and *incrp* as explained in the previous section. However, these variables are for keeping track of the wavelength, λ, instead of film thickness. The variables *lamstart* and *lamstop* should be chosen to cover the range of wavelengths of interest. The units of *lamstart*, *lamstop*, and *incr* are in meters.

Thus, for the example in Appendix A, 400 transmission data points will be calculated, with the first being at 400nm, the second at 403nm, the third at 406nm, and so on.

After establishing the wavelengths for which the transmission will be calculated, the first loop begins with the following code:

```
for n=1:numpoints+1;
    lam(n)=lamstart+(n-1)*incr;
```

The variable n is an integer which maps to wavelength in conjunction with the vector *lam*. The n^{th} element of the vector *lam* is calculated by the second line of code shown above. After the wavelength is calculated, the index of refraction for the diamond film, n_2, is calculated for that particular wavelength by solving the Sellemeier equation. This part of the code is in Appendix A, but not shown here.

The next step is to perform a numerical approximation to the integral in equation [2.12]. As has been previously stated this is done with a nested loop which carries out a weighted summation. The code which accomplishes this is listed below:

```
Tp(n)=0;
        for j=1:dpp;

            phiair(j)=(2*pi*n1*(d(dpp)-d(j)))/lam(n);
            air=[cos(phiair(j)) (i*sin(phiair(j)))/n1;
                  i*n1*sin(phiair(j)) cos(phiair(j))];

            phid(j)=(2*pi*n2(n)*d(j))/lam(n);
            D=[cos(phid(j)) (i*sin(phid(j)))/n2(n);
                  i*n2(n)*sin(phid(j)) cos(phid(j))];

            BC=air*D*[1;n3];
            B=BC(1);
            C=BC(2);
            t=(2*n1)/((n1*B)+C);
            Tp(n)=Tp(n)+(dt(j)*t);

        end
    Tr(n)=Tp(n)*conj(Tp(n));
```

Again, this loop is nested inside the first loop on the variable *n*. This nested loop operates on the variable *j*, which is tied back into the Gaussian distribution calculated earlier. The variable *j* is tied to the thickness of the layer being considered, as well as the probability of the film having that particular thickness.

The variables *phiair* and *phid* represent the phase shift experienced by the wave as it travels through the appropriate layer. The thickness of the diamond layer is calculated earlier with the Gaussian distribution, and is denoted by *d(j)*. The distance that the wave travels through air before reaching the diamond is the maximum thickness of the diamond film, *d(dpp)*, minus the particular thickness of the film being considered, *d(j)*. In these calculations, *i* is the imaginary unit.

These phase shifts are needed in the calculation of the matrices *air* and *D*. These matrices are calculated by equation [2.53].

Next, the vector *BC* is calculated, using MacLeod's nomenclature. The field transmission of the wave, *t*, is then calculated using *B* and *C*. Here, the calculation of *t* takes the square root of equation [2.69], using the fact that n_1 and n_3 are both equal to unity.

The field transmission is then multiplied by the probability of the layer being *d(j)* thick, *dt(j)* and then summed with *Tp(n)*. *Tp(n)* simply serves as a place to put the sum of the *t*dt(j)* product while the loop is running.

When the loop on *j* has finished and the total transmitted field is accounted for, the transmitted power for the rough layer, *Tr(n)*, is calculated. This is equivalent to solving equation [2.105] for the transmitted power.

The program then continues the loop on *n*, until the transmitted power has been calculated for the entire range of wavelengths selected prior to starting the loop. At the completion of the loop, the transmission curve is stored in two vectors. The fraction transmission is stored in the vector *Tr*, while the corresponding wavelengths are stored in the vector *lam*.

4.6 Summary

This chapter began by showing that a result in the literature has an inaccuracy in its derivation. Then, a model was developed which eliminates the inaccuracy of the previous model. Finally, key points of a numerical solution devised to implement this model were discussed. The program presented in this chapter uses the MacLeod matrix approach, however, the transfer matrix approach may also be used with equivalent results. Appendix A lists the full text of this program, as well as a program which solves the problem using the transfer matrix technique.

References:

[1] O.S. Heavens, Optical properties of Thin Solid Films Dover, New York, 1965.

[2] C. L. Mitsas and D. I. Siapkas, "Generalized matrix method for analysis of coherent and incoherent reflectance and transmittance of multiplayer structures with rough surfaces, interfaces, and finite substrates", Appl. Opt. **34**, 1678-1683, 1995.

[3] Charalambos C. Katsidis, Dimitrios I. Siapkas, "General Transfer-Matrix Method for Optical Multilayer Systems with Coherent, Partially Coherent, and Incoherent Interference" Applied Optics-OT, Volume 41, Issue 19, 3978-3987, July 2002.

[4] See Chapter 2 Ref. 25 (Gatesman).

[5] See Chapter 2 Ref. 26 (Robbins).

[6] See Chatper 2 Ref. 27 (Ying).

[7] M.J. Ulczynski, B. Wright, D.K. Reinhard, "Diamond-coated glass substrates", Diamond and Related Materials 7, 1639-1646, 1998.

[8] W. H. Southwell, "Modeling of Optical Thin Films", Vacuum & thinfilm, May 1999.

Chapter 5: Experimental Results and Comparison with Theory Part 1

5.1 Introduction

In this chapter, the samples produced for this research are briefly discussed, and the optical measurements made on the samples are presented. Before the measurements are presented, the values of the optical constants for gold and other materials used in this work are discussed. Then, the optical transmission measurements made on the samples, as described in Chapter 3, are compared with the theory developed in Chapter 4. After the measurements on the samples have been presented along with their relevant simulations, further simulation is explored to investigate the affects of certain physical device characteristics on the optical performance of the device. All of the simulations presented in this chapter assume a Gaussian distribution for calculations involving surface roughness. The treatment of non-Gaussian distributions is considered in Chapter 6.

5.2 Samples

Appendix B has a detailed list of most of the samples made in the course of this research. A few samples have been omitted since they concerned depositions on small pieces of wafers to test seeding techniques in a non-quantitative fashion. Fabry-Perot structures were not fabricated on all of the samples in this Appendix. Before the work on the Fabry-Perot wafers began, it was necessary to determine, and practice, seeding

techniques and deposition parameters to yield films of high optical quality. Additionally, work on various sizes of substrates was explored, along with some exploratory research in using different quartz ring heights. Eventually, the technique described in Chapter 3 was determined to be the best for producing films for the Fabry-Perot application as examined in this thesis.

Several challenges were overcome in developing the fabrication technique discussed in Chapter 3. Chapter 3 discusses the thermal stress in the diamond films and the solution obtained for that problem. Before the increased diamond deposition temperature was established, an alternate method was explored. This method was to deposit the diamond on an oxide layer. The thought was that since the thermally grown oxide layer was under tensile stress, and the diamond layer was under compressive stress, the two stresses may counteract each other enough to result in flat windows when the silicon was through-etched. This method was implemented on wafer RB2K-2 with 0.48μm of diamond over 1.4μm of SiO_2. However, only 29 of 138 windows had an intact film and these were highly wrinkled. Next, the deposition temperature was increased in order to reduce the diamond compressive stress as described in Chapter 3. The higher deposition temperature provided a solution to the wrinkling films, so no further work in the growth of diamond on an oxide layer was performed.

It is interesting to observe a plot of deposition temperature as a function of deposition pressure. Figure 5.1 shows such a plot. The data points in this plot were taken from the "FB" samples listed in Appendix B.

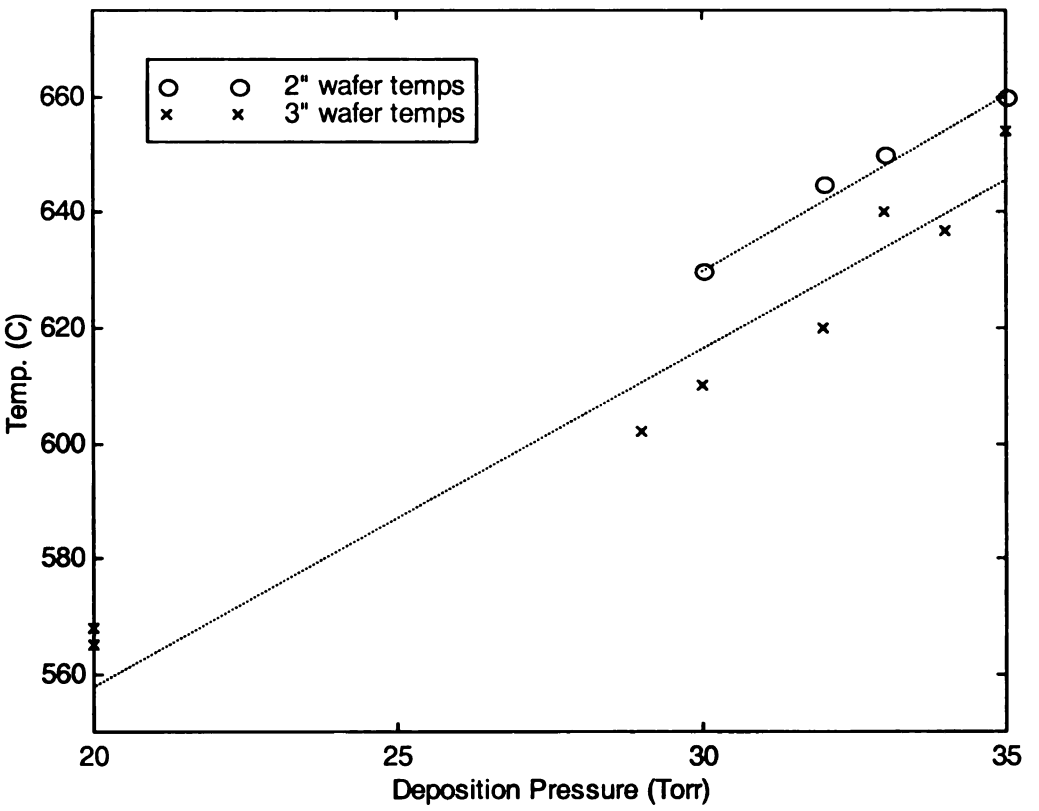

Figure 5.1 Deposition Temperature as a function of Deposition Pressure for MCPR Configuration 7 with a 59mm quartz tube height and approximately 1kW of incident power.

The data in Figure 5.1 was taken using the exact conditions that the films were deposited under for this research. The deposition system was in MCPR Configuration 7 with a 59mm quartz ring height as describer in Chapter 3. Approximately 1kW of power was incident upon the system. The probe length and sliding short were adjusted for minimum reflected power; typical values for these parameters are given in Chapter 3. Two series of data points are shown in the plot, one on 2" substrates and one on 3" substrates. Additionally, straight lines fit to the data are shown in the plot. As can be seen in the Figure, depositions on 2" substrates tend to have slightly higher measured temperatures

than those on 3" substrates. Also, for the temperature regime considered here, the temperature of the deposition tends to follow an approximately linear relationship with deposition pressure, for each substrate size studied.

A problem on some early samples was the formation of small holes in the diamond films during the KOH etching. This would sometimes lead to relatively large-area failures in the film, since the KOH was able to get beneath the diamond and etch the silicon from both sides of the wafer. The original seeding technique for this work was less elaborate than described in Chapter 3. It consisted of simply removing the wafer from the package, scratch seeding it with diamond power, and wiping the wafer clean with a KimWipe. The more thorough seeding steps discussed in Chapter 3 were implemented along with higher deposition temperatures, and the combination of these two techniques greatly reduced the appearance of the small holes in the diamond film during KOH etching.

This chapter looks primarily at Fabry-Perot structures from two wafers in particular, RB2K8 and RB2K9. These two wafers yielded the diamond films with the best optical properties of those deposited for this work. These two wafers were intended to be identical to each other, although as seen in Appendix B, RB2K9 ended up with a thinner film than RB2K8. As is discussed later in this Chapter, no further wafers were fully fabricated for Fabry-Perot measurements after RB2K9.

5.3 Optical Constants

For this research, the index of refraction for diamond is always taken from the Sellemeier equation as given by [2.11], and the index of refraction for air is assumed to be unity.

Variations exist in the published optical constants for gold[1,2,3]. In this work, two sets of optical constants are considered for gold. Palik[3] gives the constants most often cited in the literature. However, models using the Kingslake[2] data often fit the measurements made for this research better than those using the Palik data.

Possible explanations for the variations found in the published data include sample preparation, measurement technique, purity of the gold, and assumptions made in calculations of n and k from the measurements made on the samples. It stands to reason that perhaps the data compiled in Kingslake was based on experimental conditions and assumptions closer to the work in this thesis than Palik's data was.

Figure 5.2 shows a plot of the Kingslake and Palik data for the index of refraction, n, as a function of wavelength.

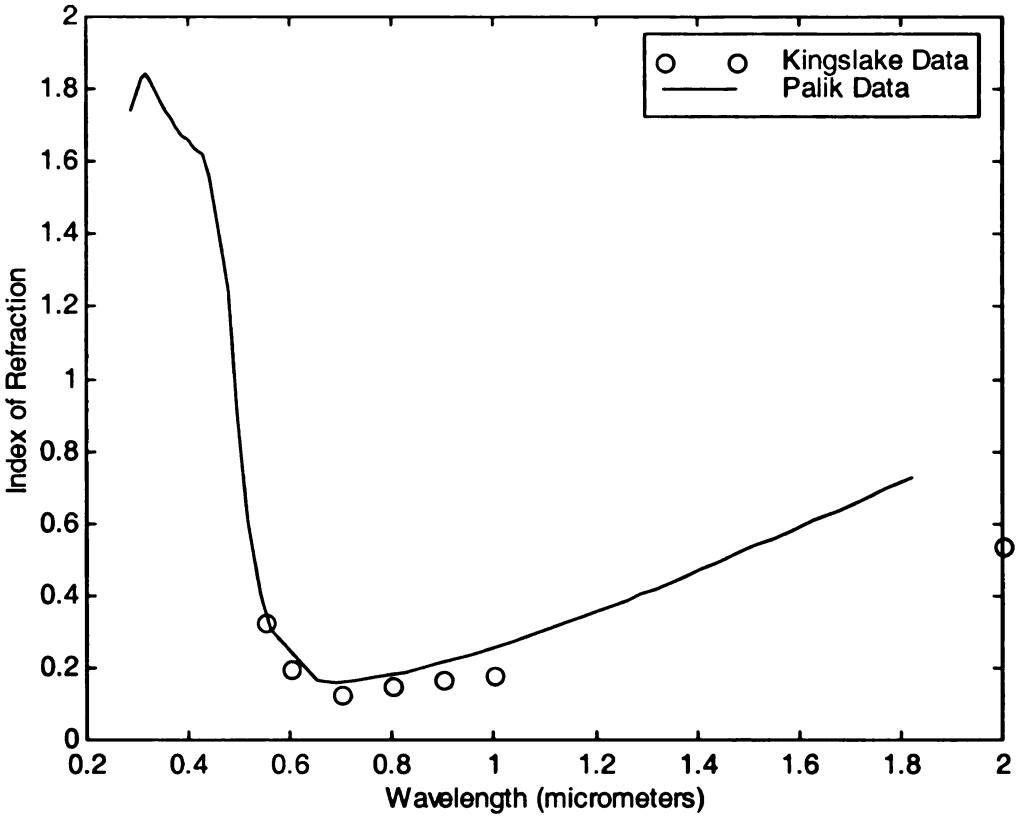

Figure 5.2 Data for the Index of Refraction for gold as a function of wavelength.

Figure 5.3 shows a plot of the Kingslake and Palik data for the absorption constant, *k*, also as a function of wavelength.

In both cases, the two sets of data are relatively close and follow similar trends. Palik's data covers a wider range of wavelengths than Kingslake's data, but Kingslake's data spans a sufficient range of wavelengths for purposes of this research.

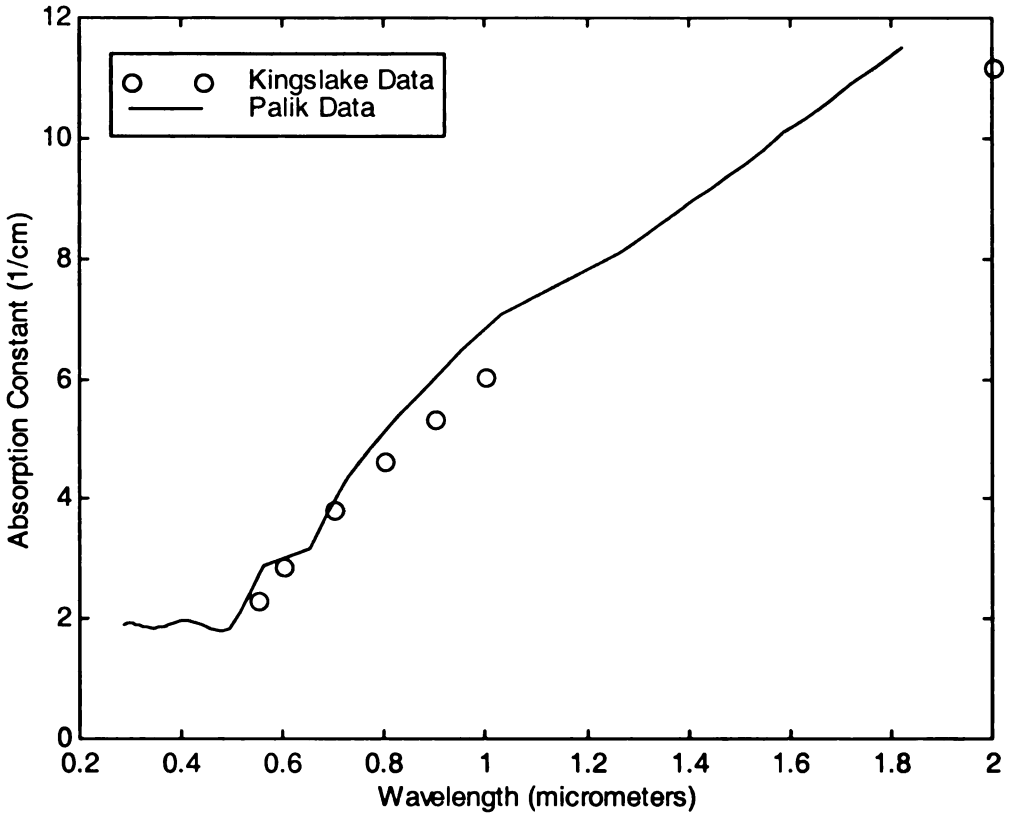

Figure 5.3 Data for the Absorption Constant of gold as a function of wavelength

Notice that in Figure 5.3, the absorption of gold increases with wavelength. This behavior is not desirable for operation in the IR. However, the deposition of gold films was readily available at the time of this research, and the films are very thin so an appreciable amount of light can still be transmitted through the film, even at the longest wavelengths studied in this work.

5.4 Measurements on Diamond Membranes without Gold Coatings

This section presents transmission measurements made on several diamond windows from two wafers, RB2K9 and RB2K8. The transmission data in this section was

collected before any gold coating was applied to the wafer. Fitting simulation to this data allows the extraction of the film thickness and the surface roughness. Observation shows that the fit is sensitive to around 1nm in thickness, and 0.5nm in RMS surface roughness.

Figure 5.4 shows the transmission through a diamond window. This window will be referred to as diamond window 1, or DW1. No gold coatings were applied at this time. This data was taken on wafer RB2K9 with a Perkin Elmer Lambda 9000 UV-Vis system.

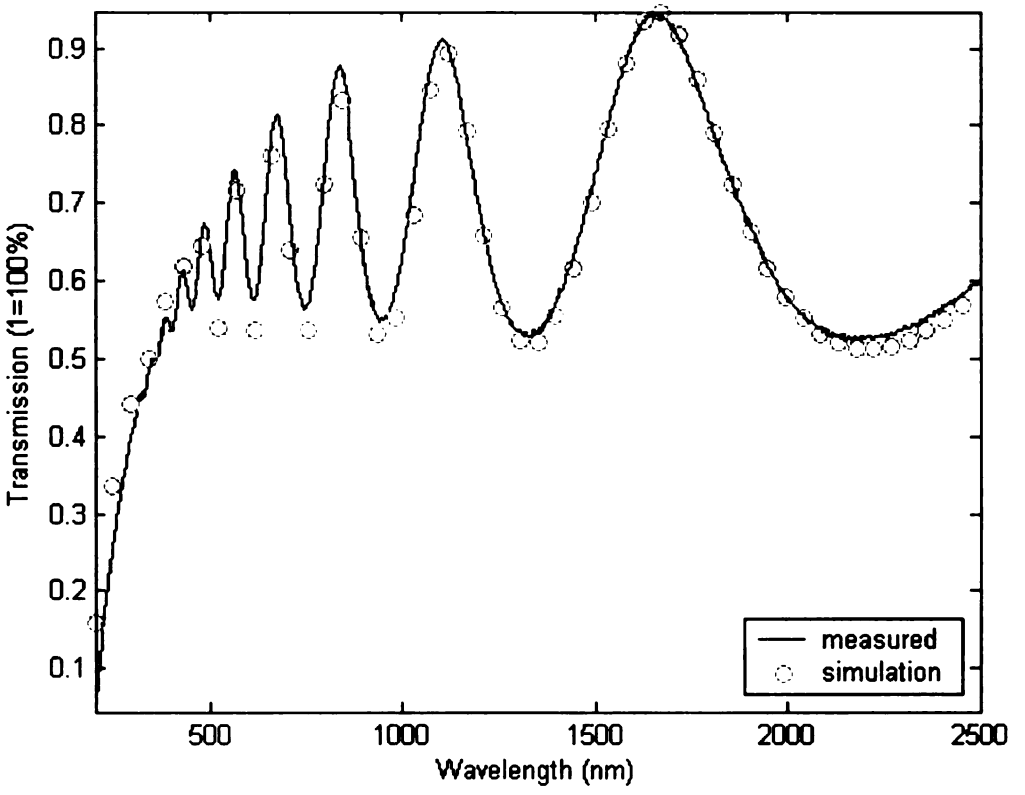

Figure 5.4 Transmission versus wavelength for diamond window 1 on wafer RB2K9. The wavelength axis spans from the UV (200nm) into the IR (2500nm).

Figure 5.4 shows good agreement between the model and experimental measurement, except for the visible region where the measured minima are higher than expected.

Alignment of the sample and mask on the Perkin-Elmer system is difficult as no fixture exists which is specific to the samples for this research. For larger area samples where beam alignment is not critical, this discrepancy was not observed. Fitting the simulation to the data indicates that this window is 695nm thick, and has a surface roughness of approximately 19nm RMS.

For a more detailed study of the portion of the spectrum where the Fabry-Perot devices are to be investigated, a different set up was used which covers a smaller spectral range but is more amenable to aligning the optical beam with the small mask opening.

Figure 5.5 shows transmission through the same window, DW1, but taken with the Bausch & Lomb equipment as described in Chapter 3. Note that this figure is different than Figure 5.3 in that the data points are shown as circles here, and the simulation is a solid line. This data has been corrected for an offset in the measurement.

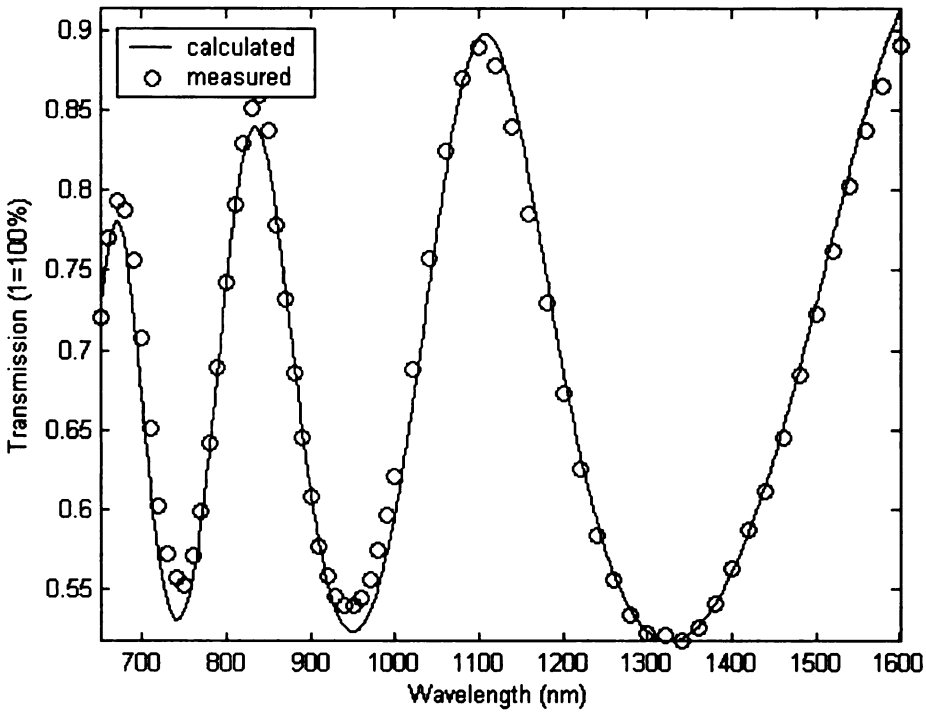

Figure 5.5 Transmission for the same window as shown in Figure 5.4, diamond window 1, but taken with Bausch & Lomb equipment.

Figure 5.6 shows transmission through a diamond window on wafer RB2K8, DW2, taken with the Bausch & Lomb equipment. This data has been corrected for an offset in the measurement.

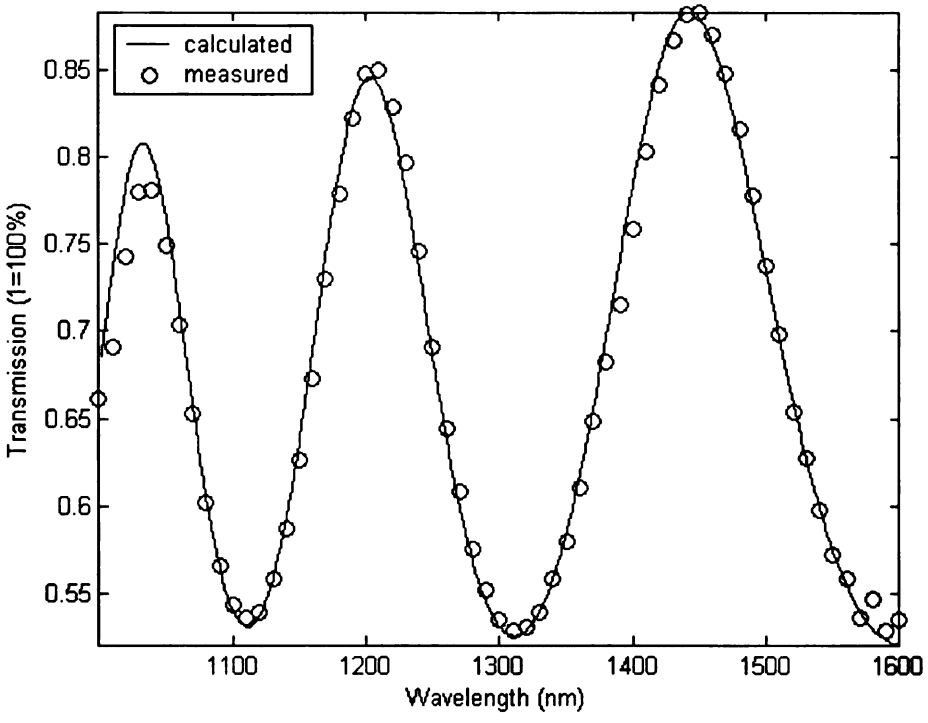

Figure 5.6 Transmission versus wavelength for diamond window 2, on wafer RB2K8.

Fitting the simulation to Figure 5.6 indicates that this film is 1.51μm thick, and has a surface roughness of approximately 27nm RMS.

Figure 5.7 shows another diamond window on wafer RB2K8, DW3, with data also taken on the Bausch & Lomb system. This data has also been corrected for an offset in the measurement.

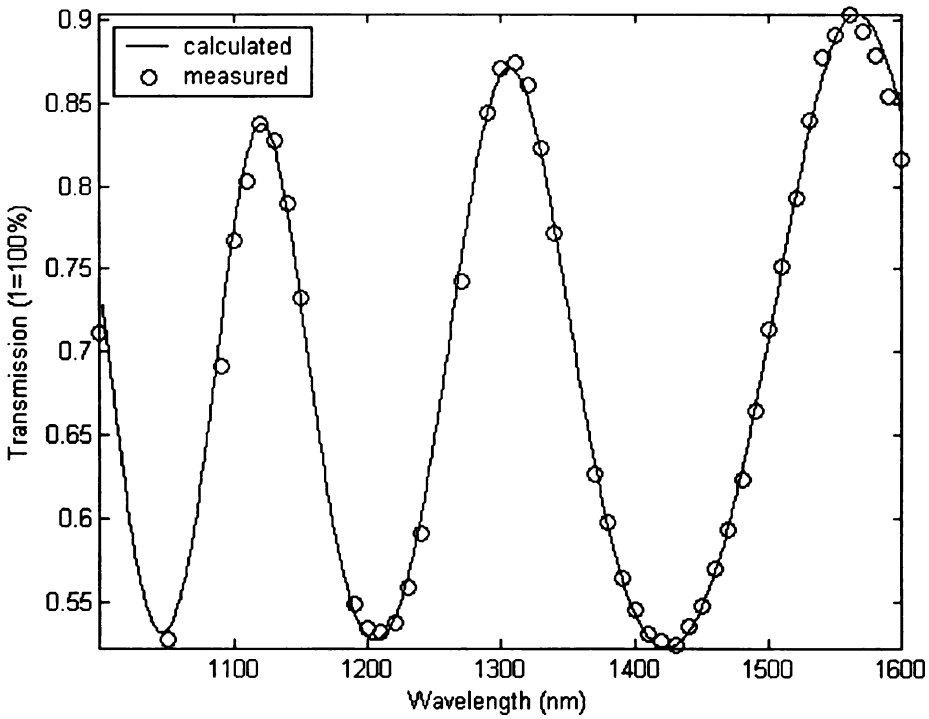

Figure 5.7 Transmission versus wavelength for diamond window 3, on wafer RB2K8.

Fitting the simulation to this data shows that the window is 1.64μm thick, and has an RMS surface roughness of 26nm.

Figure 5.8 shows the transmission through a window on RB2K9, DW4, taken with the Bausch & Lomb system. The measured transmission was shifted down by approximately 2% to fit the simulation.

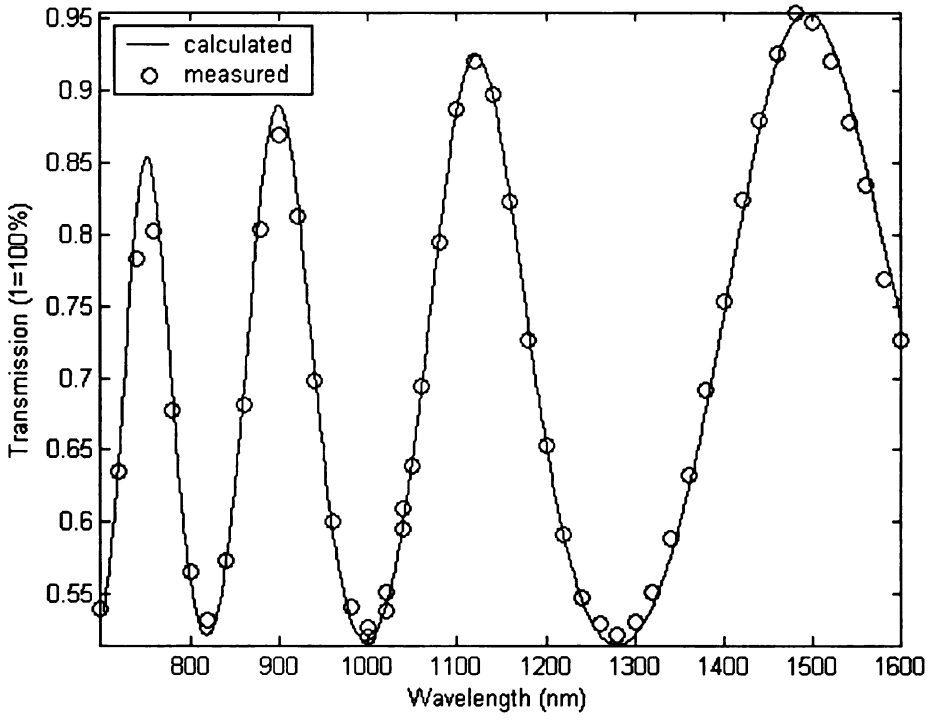

Figure 5.8 Transmission versus wavelength for diamond window 4, on wafer RB2K9.

Fitting the simulation to this data indicates that the film is 938nm thick, and has an RMS surface roughness of about 16nm.

Figure 5.9 shows another window on wafer RB2K9, DW5, taken with the Bausch & Lomb system. This data has had no correction applied.

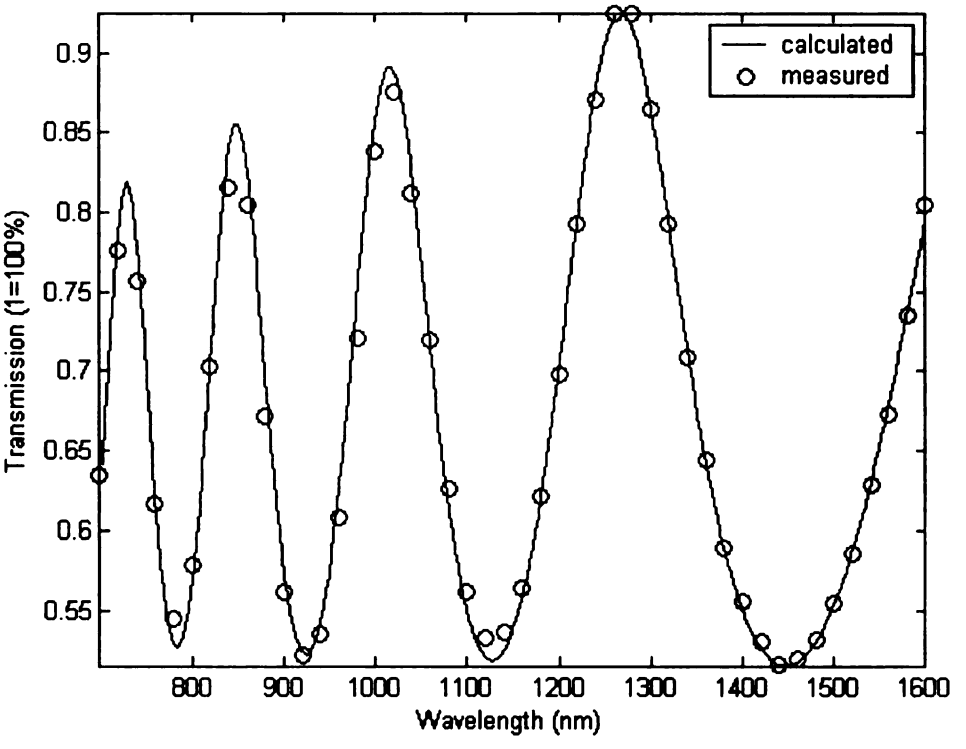

Figure 5.9 Transmission versus wavelength for diamond window 5, on wafer RB2K9.

Fitting the simulation to the data indicated that this film is 1.06μm thick, and has a surface roughness of 18nm RMS.

Figure 5.10 shows data for another window on sample RB2K9, DW6, taken with the Bausch & Lomb system. This data has not been corrected.

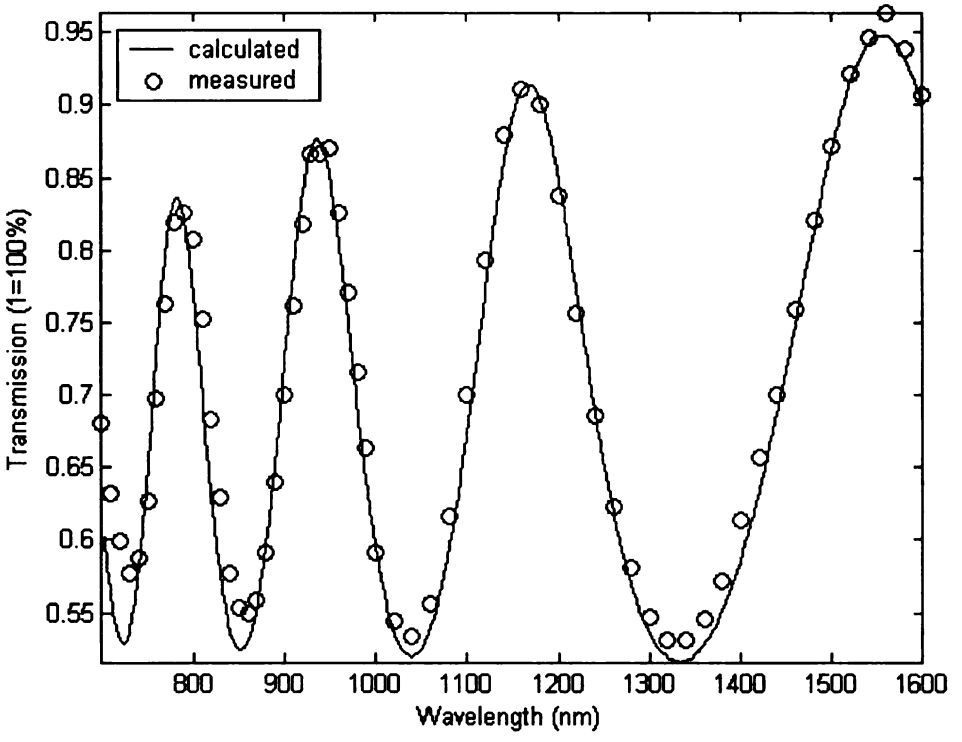

Figure 5.10 Transmission versus wavelength for diamond window 6, on wafer RB2K9.

Fitting the simulation to this window indicates a film thickness of 977nm, and an RMS surface roughness of 18nm.

Some conclusions from these measurements are that RB2K8 appears to be a rougher film than RB2K9, in that measurements on it showed 19nm to more than 25nm RMS of surface roughness, while RB2K9 typically showed less than 20nm. Also, RB2K8 appears to be thicker than RB2K9, with both of its windows showing around 1.6μm of

thickness, while RB2K9 showed no windows thicker than 1.06μm. A higher surface roughness on thicker films is consistent with columnar growth of the diamond film.

5.5 Measurements on Fabry-Perot Cavities

Many windows were measured, coated with gold to form resonators, and measured again for this research. In fact, it took a large amount of trial and error to arrive at the approximate 5/3 ratio of gold thickness discussed in Chapter 3. Presented in this section are measurements of two resonators constructed on RB2K9.

Figure 5.11 shows the transmission through the resonator constructed from DW1, the diamond window shown in Figures 5.4 and 5.5. No correction has been applied to this measurement.

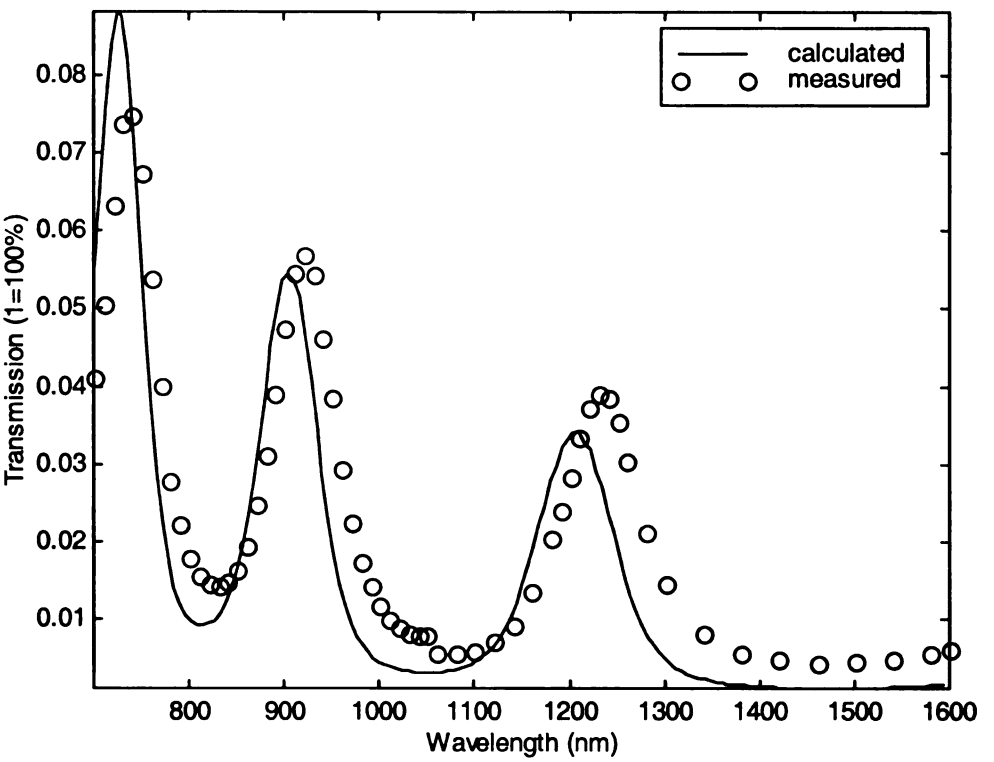

Figure 5.11 Transmission through Fabry-Perot resonator 1, constructed on wafer RB2K9.

The parameters used in this calculation are a nominal diamond film thickness of 695nm, an RMS surface roughness of 19nm, and gold thickness values of 21.5nm and 35.8nm on the smooth and rough sides of the film, respectively. The measurement and simulation do not track as well as they do for uncoated diamond windows, however, there is a close enough match to draw some conclusions from the simulation.

Of particular interest for this measurement and simulation are the Q values of the resonant peaks. The measured peak at 920nm of wavelength has a Q value of 11.5. The

measured peak at 1220nm has a Q of 12.3. The simulation shows a Q of approximately 12.6 for each peak.

Figure 5.12 shows transmission through a Fabry-Perot resonator constructed using DW5, the window shown in Figure 5.9. No correction has been applied to this measurement.

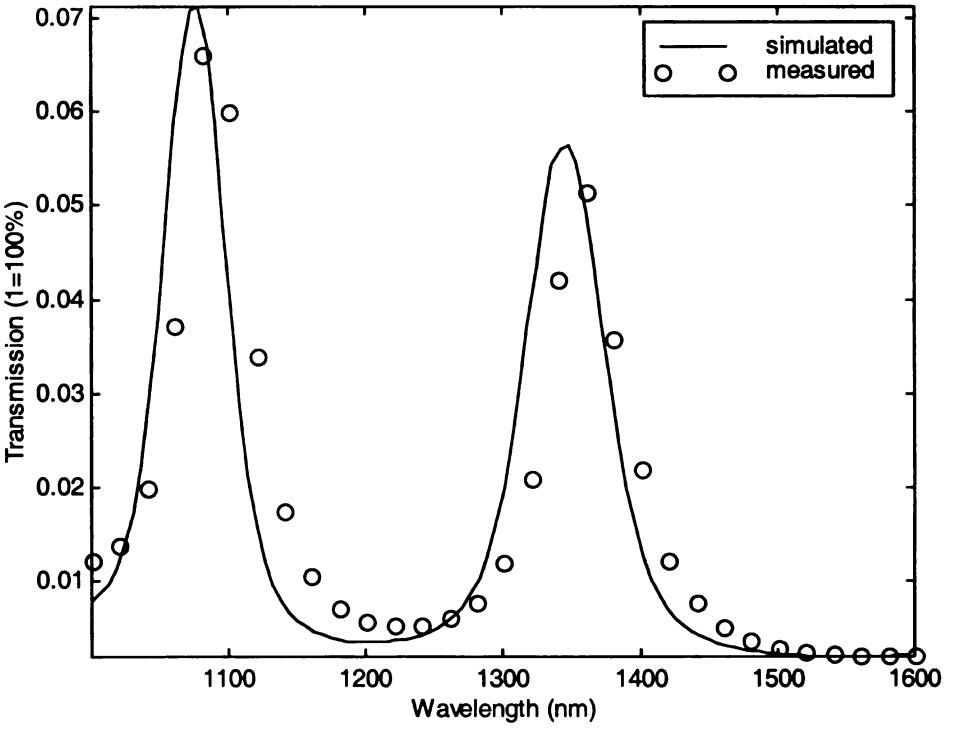

Figure 5.12 Transmission through Fabry-Perot resonator 2, on wafer RB2K9.

The parameters used in this simulation are a diamond window thickness of 1.06m, a surface roughness of 18nm RMS, and gold thickness values of 23nm and 27nm. This window shows a somewhat better fit than is seen in Figure 5.11.

For the measurements in Figure 5.12, the peak occurring at 1080nm has a Q of 18, and the peak at 1370nm has a Q of 17. The simulated peaks show Q values of approximately 20 and 20.4, respectively.

The Q values attained in these measurements are not particularly high, and the total transmission through the cavity is in the neighborhood of 10% or less. Rather than repeating the fabrication sequence to make more cavities with similar performance, it is pertinent to investigate what is limiting the performance of the device.

5.6 Using the Simulation to Gain Insight into the Device

While the simulated Q values are somewhat high compared to measurement, they are close enough that the simulation can be used to identify trends in Q as a function of physical resonator parameters. The surface roughness of the diamond film is one of the main limiting factors in attaining good performance from the device. Figure 5.13 shows a simulation of Q as a function of surface roughness.

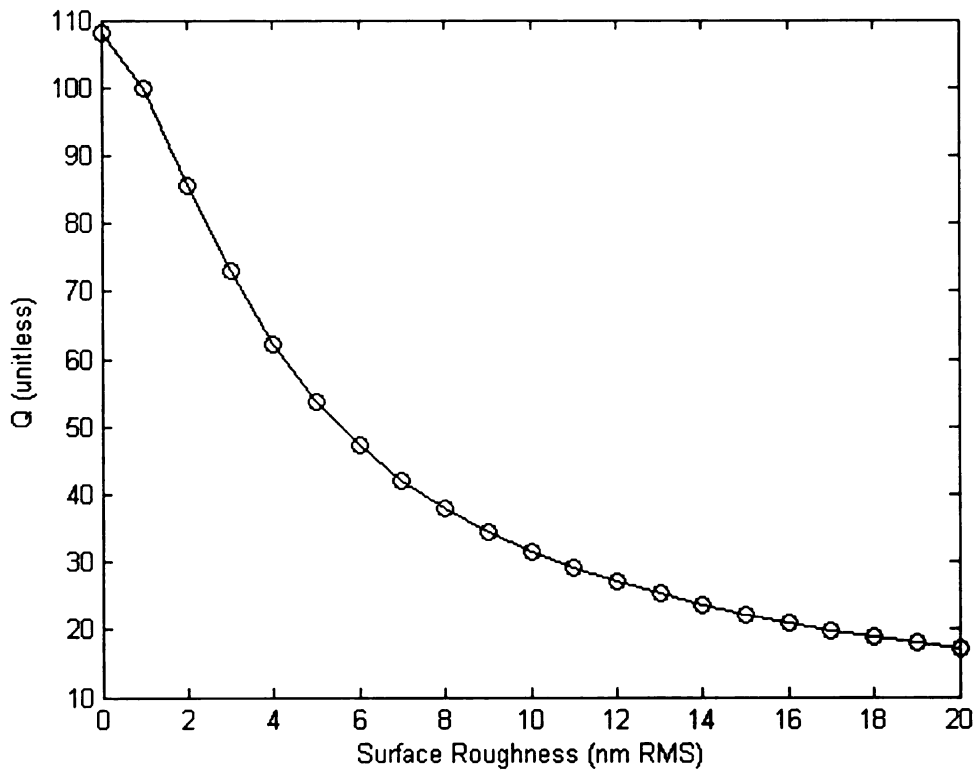

Figure 5.13 Q as a function of surface roughness for a resonator based on a 1μm thick diamond film.

The simulation for Figure 5.13 is based upon a diamond thickness of 1μm, and a gold thickness of 31.5nm on each side of the diamond. The peak studied for the simulation is at 1265nm. From this simulation, it can be seen that the surface roughness of the diamond film is critical to the performance of the resonator. Even at a roughness of around 5nm RMS, Q is reduced from that of a perfectly smooth film by a factor of about 2 for the resonator in question. For surface roughness in the range of 15-30nm, like the films in this study typically show, Q is reduced by a factor of 4 to 5 from the case of perfectly smooth diamond.

A second parameter of concern is the thickness of the gold layers deposited on the diamond window. Since gold has strong absorption at optical wavelengths, this serves to attenuate the power of the transmitted beam. However, performance of the resonator relies on having a reflective surface on either side of the diamond film, so there is a trade-off between signal attenuation and resonator performance, expressed here as Q. To investigate this, a new figure of merit can be established. Figure 5.14 shows a plot of Q multiplied by the peak transmission, QT, as a function of gold thickness.

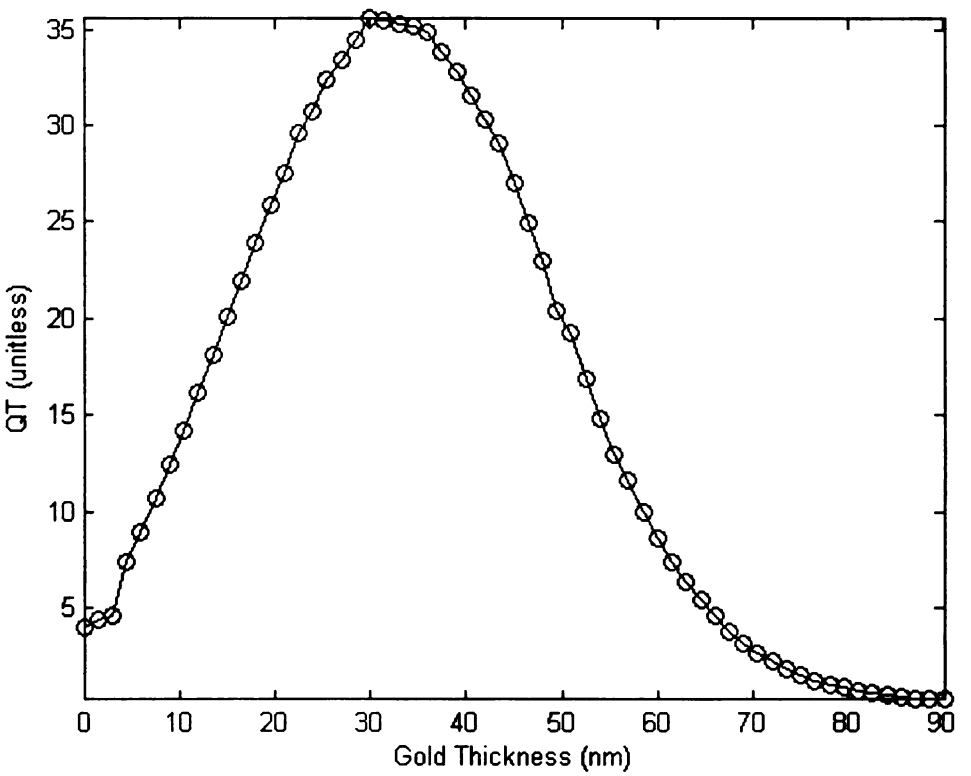

Figure 5.14 QT as a function of gold thickness for a resonator based on a 1μm thick diamond film.

The simulation in Figure 5.14 is based on a smooth diamond film 1μm thick. The gold thickness shown on the x-axis is the thickness of the gold layer on each side of the diamond film. The wavelength of the peak studied in this simulation actually shifts with

increasing gold thickness, however, it is in the range of 1 to 1.2μm. In this case, QT peaks at around 30nm of gold thickness. So having 30nm of gold thickness on each side of the wafer would represent the optimum design for maximizing QT.

The next simulation, shown in Figure 5.15, also creates a plot of QT as a function of gold thickness, in this case, however, 18nm of RMS surface roughness is added to the simulation.

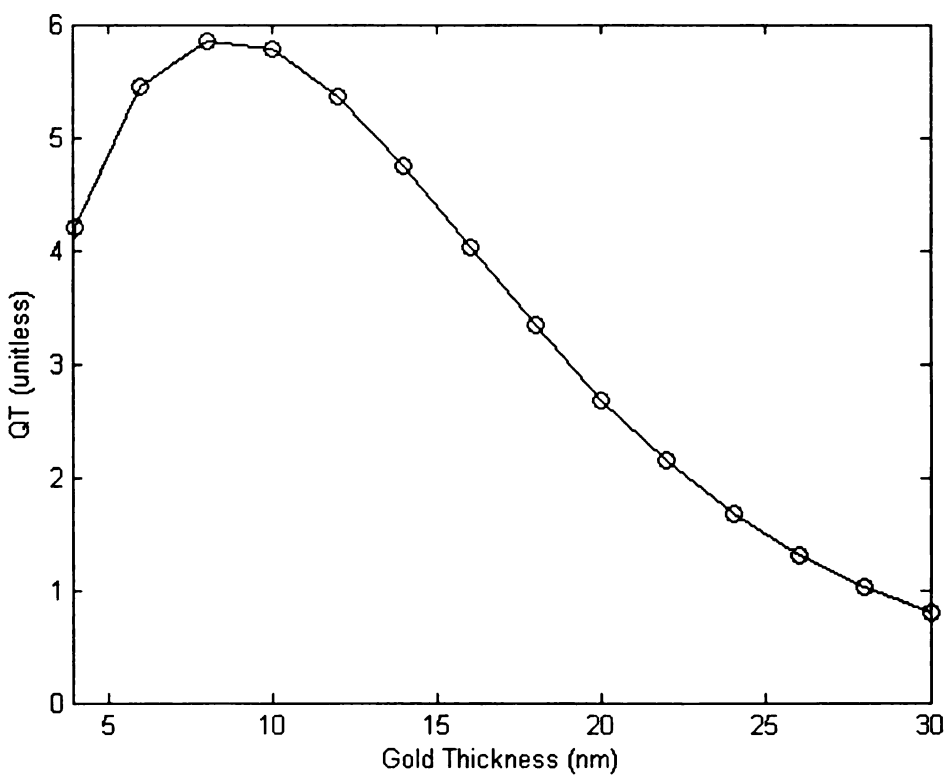

Figure 5.15 QT as a function of gold thickness for a resonator based on a 1μm thick diamond film with a surface roughness of 18nm RMS.

The resonator studied in this figure is based on a 1μm thick diamond window with 18nm of RMS surface roughness. As can be seen in this figure, the addition of surface

roughness changes the gold thickness that maximizes the figure of merit QT. In this case, the simulation indicates that extremely thin gold layers may lead to optimal performance, however, layers this thin are not known to demonstrate the same optical constants as bulk gold[4], so the simulation may not be accurate in this range of thicknesses. The conclusion can nonetheless be drawn that thinner gold layers may give better results for rough diamond membranes.

The final simulation for this chapter, shown in Figure 5.16, is similar to that shown in Figure 5.13, but in this case, thinner gold layers are used.

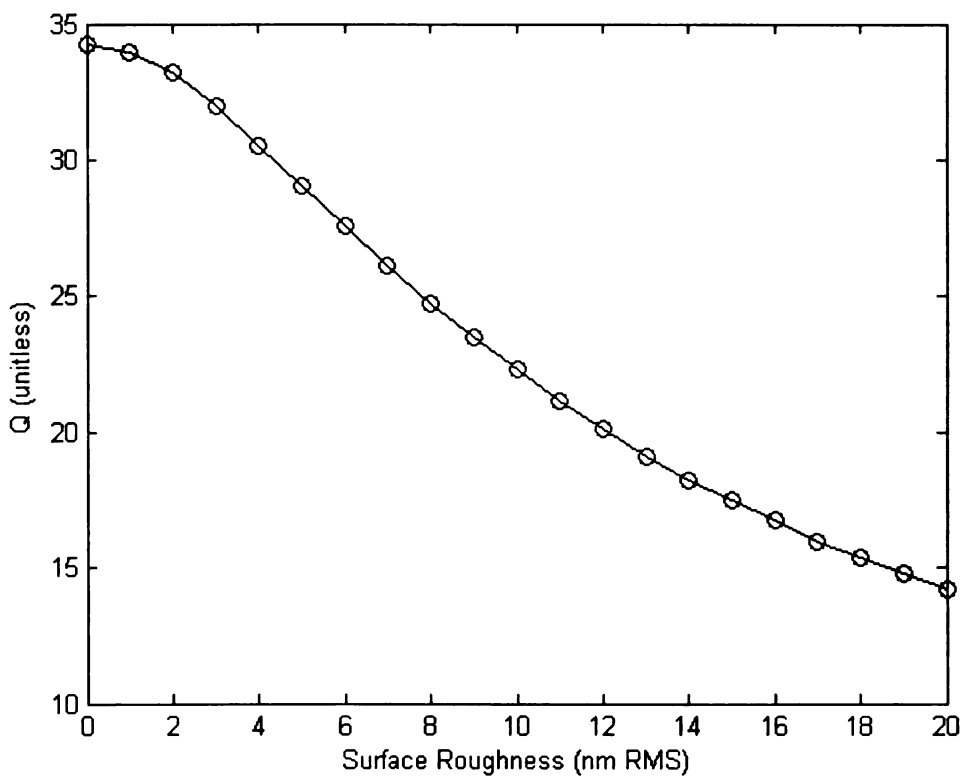

Figure 5.16 Q as a function of surface roughness for a resonator based on a 1μm thick diamond film.

The simulation shown in this figure uses a 1μm thick diamond window with 15nm thick gold layers on each side. As can be seen from this figure, the Q is even lower than that shown in Figure 5.13, however, since the peak transmission was also considered in this selection of gold thickness, more power should be transmitted through the resonator in this case. Figures 5.17 and 5.18 compare these two simulations further. Figure 5.17 shows the Q as a function of surface roughness for both models.

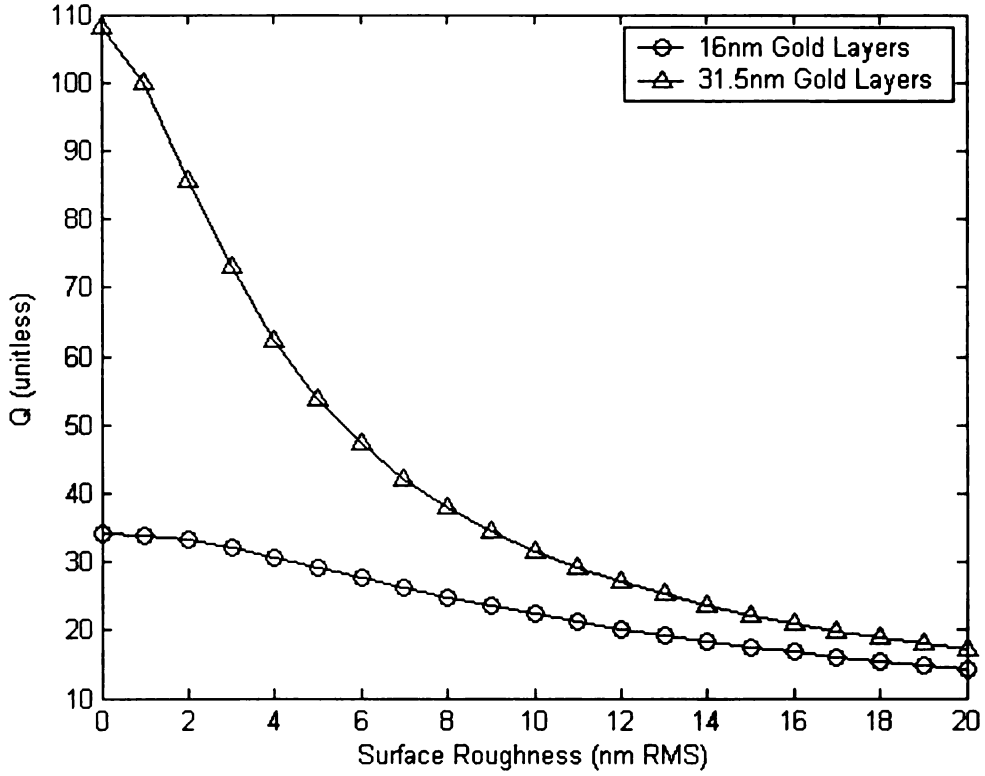

Figure 5.17 Q as a function of surface roughness for both gold layer thicknesses considered.

Figure 5.18 shows the peak transmission as a function of surface roughness. This plot shows that the thinner gold layers should pass a larger percentage of the optical power, despite having peaks that are less sharp.

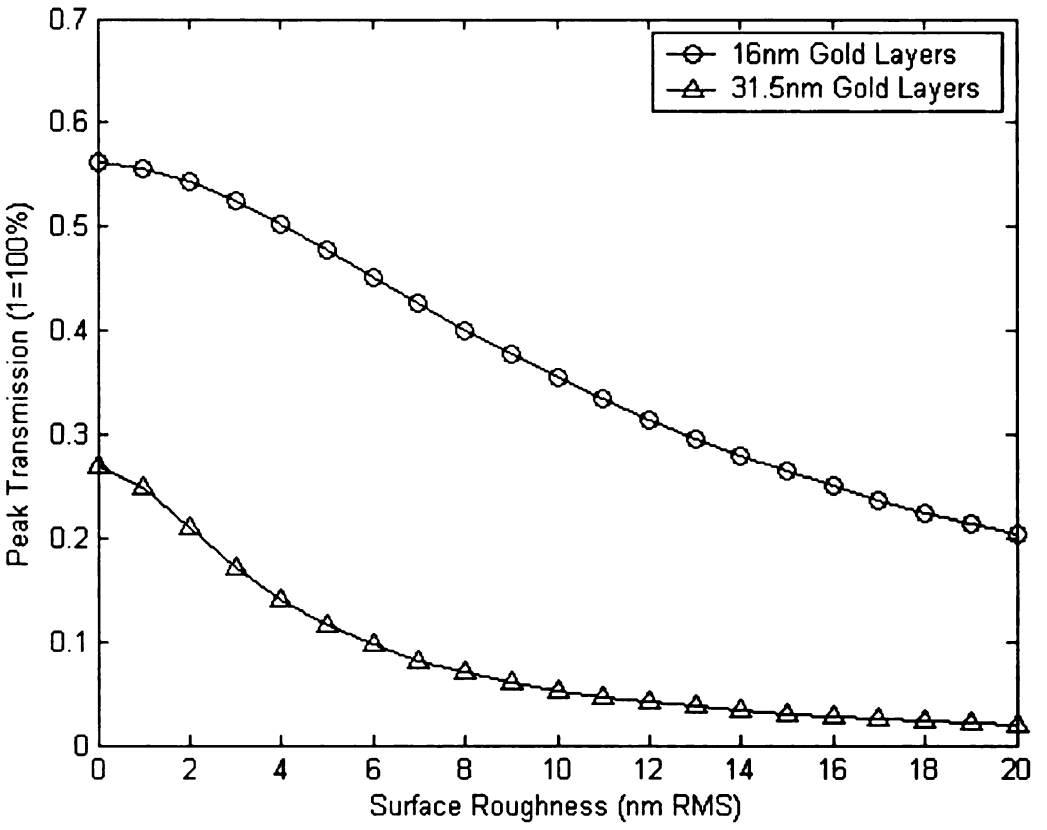

Figure 5.18 Peak transmission vs. surface roughness for the two gold layer thicknesses considered.

What can be seen from Figures 5.16, 5.17, and 5.18 is that achieving a high Q with realistic, as-grown surface roughness values is not possible. This means that to increase the Q values of these cavities to reasonable levels, without sacrificing almost all of the transmitted power, a post-processing technique, for example a mechanical polishing step, is needed. This is beyond the scope of this research and was not investigated experimentally. However, using simulations such as those in this section can give an estimation of what surface roughness must be achieved in order to reach a desired Q value.

Another interesting route for future exploration is to use reflective layers made from either metals that are less lossy than gold, such as silver, or preferably lossless materials. The application of lossless multilayers as reflective coatings for Fabry-Perot resonators, however, is a non-trivial and is beyond the scope of this work[5].

5.7 Summary

In this chapter, the samples fabricated for this research were briefly discussed, as well as the optical constants of the materials specific to this work. After this discussion, measured results were shown with their corresponding simulations, and the parameters extracted from the simulations were listed. Finally, the simulation was used to show that the current method of fabricating the resonators will result in relatively low Q values, although some optimization of the device behavior is possible. The low Q is primarily a function of surface roughness in the diamond film. The diamond films grown for this research tend to be relatively smooth for PECVD diamond films, and even if it is possible to grow the film with somewhat less surface roughness, the simulation shows that significant gains in Q will not be seen until the RMS surface roughness of the film is in the range of 5nm or less. This would not be likely in as-grown films using the current deposition method. This means that to fabricate resonators with significantly higher Q values, a polishing step is probably needed. Alternatively, one may use a different growth method, such as that used to grow ultra-nanocrystalline diamond films.

References:

[1] W. G. Driscoll, W. Vaughan, eds, Handbook of Optics, Sponsored by the Optical Society of America, McGraw-Hill Book Company, New York, NY, 1978.

[2] See Chapter 2 Ref. 34 (Kingslake).

[3] E.D. Palik, ed, Handbook of Optical Constants of Solids, Academic Press, Inc, New York, NY, 1985.

[4] S. A. Kovalenko, "Dimensional effects in thin gold films", Semicond. Phys., Quant. Elect. & Optoelect., V3 N4, 2000.

[5] P.E. Ciddor, *Applied Optics* 7, 2328-2329, 1968.

Chapter 6: Experimental Results and Comparison with Theory 2

6.1 Introduction

In Chapters 4 and 5, it is explicitly assumed that the samples have a surface roughness that can be modeled by a employing a Gaussian distribution. An important question to consider is if this is a good approximation to the reality of the film, since the fit of Chapter 4's theory is not perfect with the measurements in Chapter 5. In this chapter, atomic force microscopy (AFM) measurements are used to show that the surface roughness displayed by most films is indeed close to a Gaussian distribution. Additionally, parameters can be extracted from the AFM image. The most interesting parameter for this research may be the RMS surface roughness, σ. Higher order moments of the distribution can also be extracted from the data.

6.2 Samples

AFM measurements were made on three samples, RB2K8, RB2K9 and FB26. The sample FB26 was not patterned or through-etched like RB2K8 and RB2K9, although the diamond film was deposited under conditions similar to those studied in this work. Additionally, some optical transmission data is available for this sample.

As listed in Appendix B, the film on RB2K8 was deposited at 35 Torr for 5.5 hours. The gas flows were 200 sccm of H_2, 8 sccm of CO_2, and 3 sccm of CH_4. A weight gain

during diamond deposition of 8.7 mg was recorded for this sample. Optical transmission measurements indicate a thickness of 1.5μm.

Also as listed in Appendix B, the film on RB2K9 was deposited at 35 Torr for 5.5 hours. The gas flows were 200 sccm of H_2, 8 sccm of CO_2, and 3 sccm of CH_4. A weight gain during diamond deposition of 6.3 mg was recorded for this sample. Optical transmission measurements indicate a thickness on the order of 0.9μm.

The film on the FB26 sample was deposited at the same gas flows, but the pressure was 20 Torr and the deposition was 12 hours in length. At this pressure, the observed temperature of the substrate during deposition was approximately 590°C. FB26 was grown as part of a different set of experiments than this research, so no weight gain data was collected. However, optical transmission measurements show that this film is approximately 1.4μm thick.

6.3 AFM Images

AFM is an interesting instrument, in that it gives a numerical measurement of the sample topography. This thesis uses these measurements in an attempt to gain insight into the nature of the diamond film, but the AFM can be used as an imaging tool, as well. Figure 6.1 shows an AFM image of sample RB2K8.

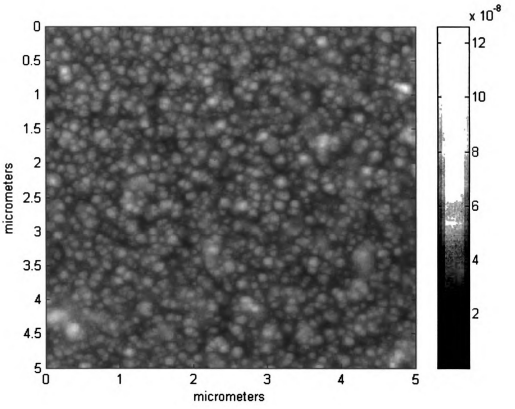

Figure 6.1 AFM picture of sample RB2K8 (this image will also be referred to as AFM Image 2)

The horizontal dimensions of the sample are plotted in the X-Y plane, while the Z dimension is plotted as map in gray scale. The scale bar on the right side of the picture corresponds to the surface height measurement.

The granularity of the diamond film is clearly visible in this image. The image is essentially a view straight down onto the diamond film. The AFM image is not optical in nature, the intensity of the pixels is based on the height of the sample measured at that point. The image in Figure 6.1 is 5μm on a side in the X-Y plane, and the Z scale extends from the lowest point measured on the sample up to approximately 200nm above

the lowest point. The lowest point on the sample would be black, and the highest point of the sample would be white, with varying shades of gray in between.

AFM is capable of very high resolution. Figure 6.2 shows an image from the sample FB26, which is 1μm by 1μm.

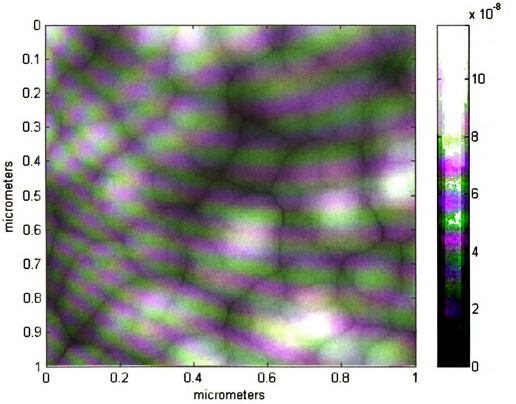

Figure 6.2 AFM image of the sample FB26 (this image will also be referred to as AFM Image 8).

Figure 6.3 shows an image taken at the same location as Figure 6.2, but at a higher magnification so that each side of the image is 500nm.

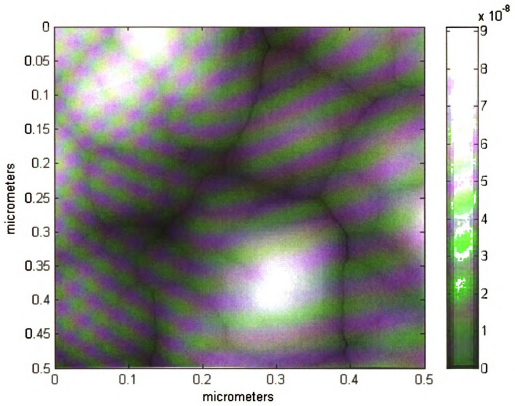

Figure 6.3 AFM image of sample FB26 (this image will also be referred to as AFM Image 9).

These two figures show interesting images of the grains in the diamond film. By inspection of the images, the average grain size is clearly sub-micron, in the range of 200-300nm.

Other renderings of AFM images can be generated in addition to top views. Figure 6.4 shows a simulated 3-dimensional view of the same measurement shown in Figure 6.1.

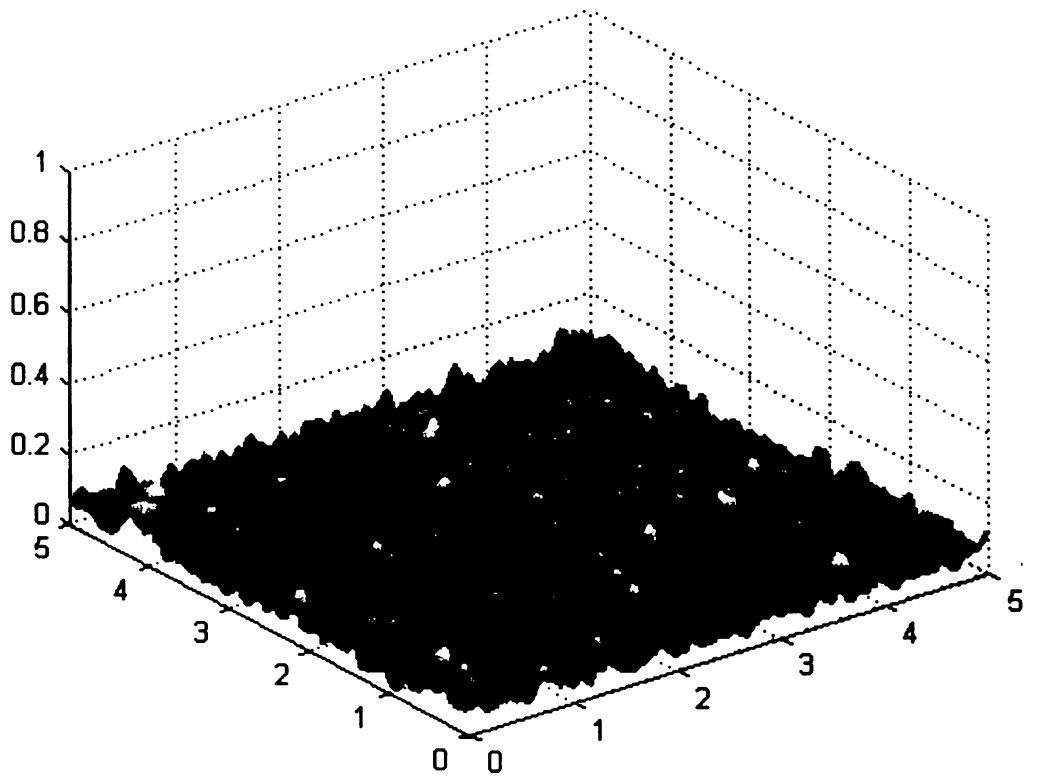

Figure 6.4 Simulated 3-Dimensional view of data in Figure 6.1, sample RB2K8. All axes are in units of micrometers.

Notice that the aspect ratio of the image in Figure 6.4 is not proper, that is, the Z axis spans 1μm, while the X and Y axes each span 5μm. This leads to the surface appearing to be rougher than it would if the scales were equal in proportion.

6.4 AFM Data

As discussed in Chapter 3, the AFM used in this research is a Digital Instruments Nanoscope III. That particular instrument is capable of producing an ASCII file containing the data from its measurement. The file has a header that contains information

on the scaling of the image, the size of the measurement, the number of data points, dates, miscellaneous settings of the instrument, etc. The actual image is represented by a matrix of integers. Each element of the matrix corresponds to a pixel in the AFM image.

The physical dimensions of measurements made by the instrument can be determined by using the data in the file header combined with the matrix of integers. A MATLAB program was written to do this.

Once the data is in MATLAB, it becomes possible to perform some statistical analysis. One of the first questions then explored is whether or not the measured surface heights follow a Gaussian distribution. The next exploration has to do with extraction of parameters from the measurements, namely the moments of the distributions.

Through a MATLAB program, the distribution measured by the AFM can be plotted. Figure 6.5 shows a plot of the distribution of surface heights measured for Figure 6.1, as well as a calculated Gaussian distribution, shown for comparison. There are two parameters in the calculated Gaussian, the mean value and the standard deviation. In this case, the mean was chosen to fit the measurement. The mean of the measurement has no significance to this work. For modeling purposes, the mean is the mean thickness of the film, which the AFM cannot measure, and must be determined by alternate methods. The standard deviation was taken from a value calculated by the AFM software. The Y values are arbitrary.

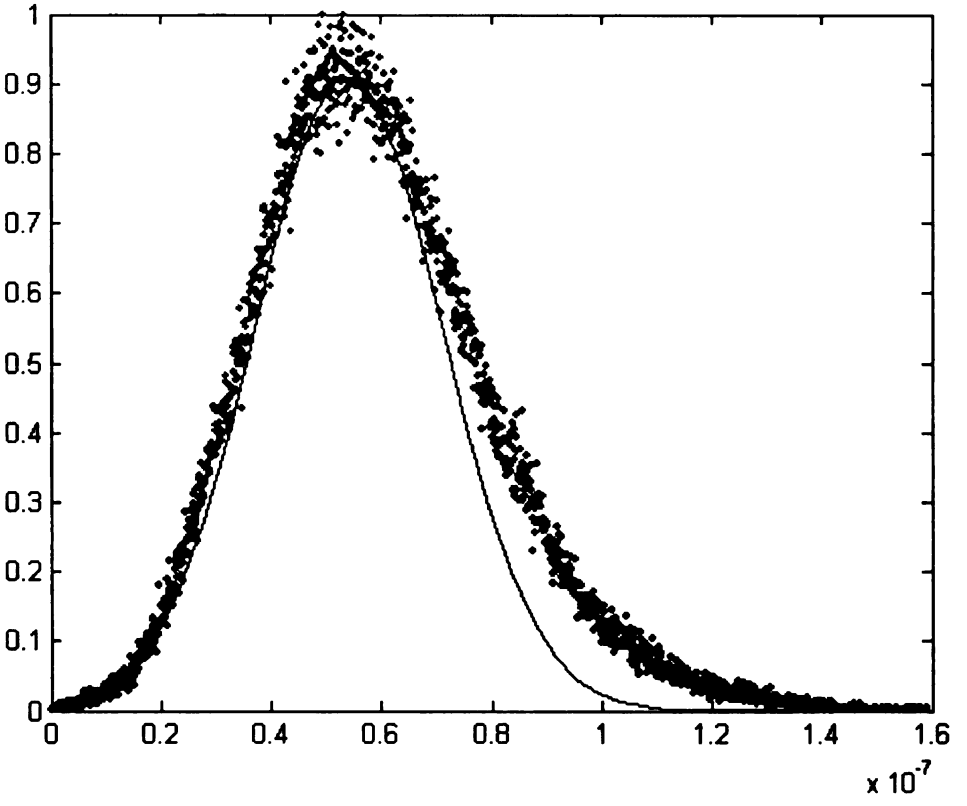

Figure 6.5 Distribution of surface heights for sample RB2K8, as taken from the AFM image shown in Figure 6.1 (data points), and an ideal Gaussian distribution (black line).

The data for this plot follows something similar to a Gaussian distribution, but that there is some difference. One interesting observation is that using the measured mean of the distribution is not the best fit of the pure Gaussian distribution to the measurement.

6.5 Calculations of Statistics from AFM Image Files

Many software packages are available to calculate statistics of a set of numbers, but the AFM images in this work pose a few obstacles. First, the data is in the form of a matrix that typically needs to be converted into a single column array, or a double summation

could be used to perform the statistical calculations. Secondly, the data should be scaled properly in order to calculate meaningful statistics. Scaling was addressed previously in Section 6.4. For this research, the matrix data from the AFM image file was converted into a single column vector by a MATLAB program.

In this Chapter, four statistics of the distribution are considered. These are the mean value, the standard deviation, the skewness and the kurtosis[1,2,3,4]. The mean value corresponds to the average film thickness – although the AFM cannot directly measure this quantity. The standard deviation is a measure of the variation about the mean, i.e. the surface roughness of the film. The skewness is a measure of how centered, or symmetric, the bulk of the surface height distribution is about the mean value. The kurtosis is a measure of how flat or sharp the top of the peak is compared to an ideal Gaussian distribution.

The vector z contains all of the points measured by the AFM in a sequential order. If the vector has N points, the mean, z_{mean}, can be calculated by:

$$z_{mean} = \frac{1}{N}\sum_{i=1}^{N} z_i \qquad [6.1]$$

The standard deviation of the distribution, σ, can be calculated by:

$$\sigma = \sqrt{\frac{1}{N}\sum_{i=1}^{N} z_i^2} \qquad [6.2]$$

The skewness, *skew*, of the distribution can be calculated by:

$$skew = \frac{1}{(N-1)\cdot\sigma^3}\sum_{i=1}^{N}\left(z_i - z_{mean}\right)^3 \qquad [6.3]$$

With this definition of skewness, a pure Gaussian distribution will have a skewness of zero.

The kurtosis, *kurt*, of the distribution can be calculated by:

$$kurt = \frac{1}{(N-1)\cdot\sigma^4}\sum_{i=1}^{N}\left(z_i - z_{mean}\right)^4 \qquad [6.4]$$

Using this definition of kurtosis, a pure Gaussian distribution will have a kurtosis of three. Kurtosis is also sometimes defined by subtracting three from equation [6.4].

A MATLAB program was written that applies the above formulae to the distribution gathered from the AFM image file, and outputs the calculated values.

6.6 Measurements

The AFM measurements made for this research are now presented. For each measurement, a top view image is first shown (or in some cases, reference is made to an earlier figure), and then the measured distribution of surface heights, plotted along with an ideal Gaussian distribution, which is shown to illustrate any deviation from this ideal case. Additionally, the mean value of the distribution, standard deviation (which is the

RMS surface roughness), skewness and kurtosis for each measured distribution are given. These statistics are calculated from the actual measurements.

6.6.1 AFM Image 1: RB2K8-1

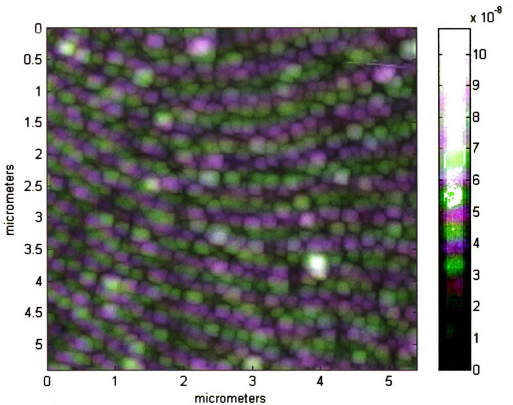

Figure 6.6 AFM Image 1

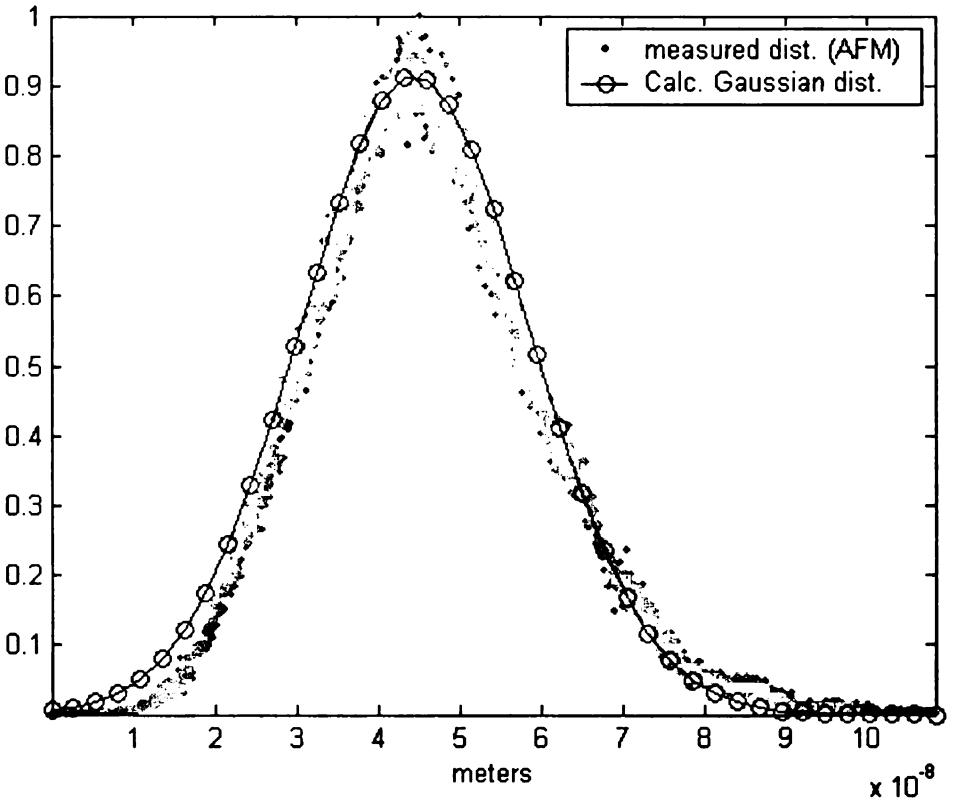

Figure 6.7 Distribution for AFM Image 1 from RB2K8.

For AFM Image 1, the measured mean is 46.373nm, and the measured standard deviation is 14.070nm. The measured skewness is 0.4424, and the measured kurtosis is 3.4155.

6.6.2 AFM Image 2: RB2K8-2

The image for AFM Image 2 is shown in Figure 6.1. The distribution measured from the image is shown below.

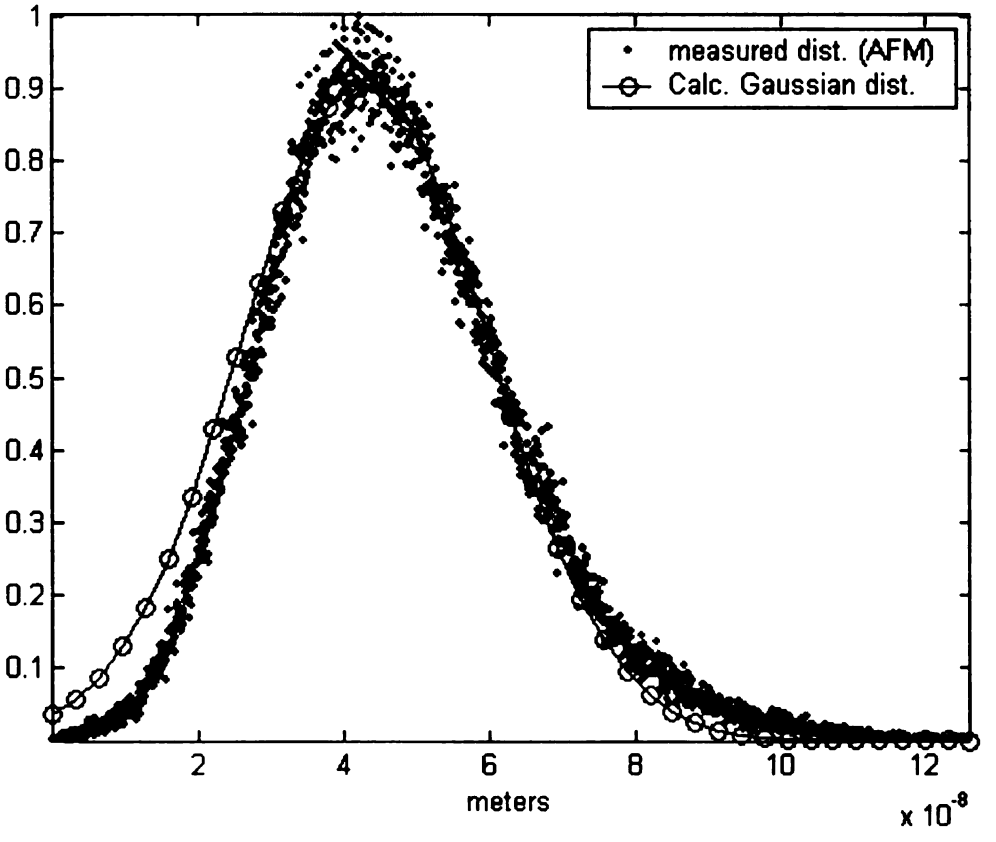

Figure 6.8 Distribution for AFM Image 2 from RB2K8.

For AFM Image 2, the measured mean is 46.668nm, the measured standard deviation is 16.882nm, the measured skewness is 0.5253, and the measured kurtosis is 3.4619.

6.6.3 AFM Image 3: RB2K8-3

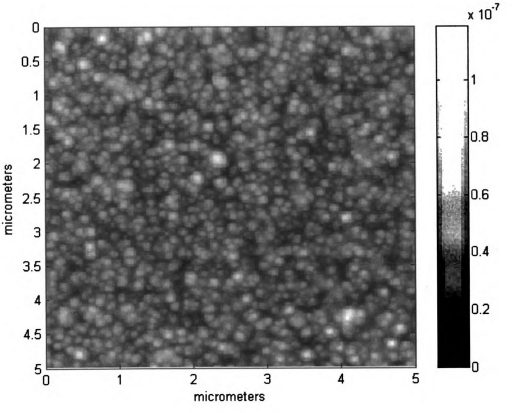

Figure 6.9 AFM Image 3.

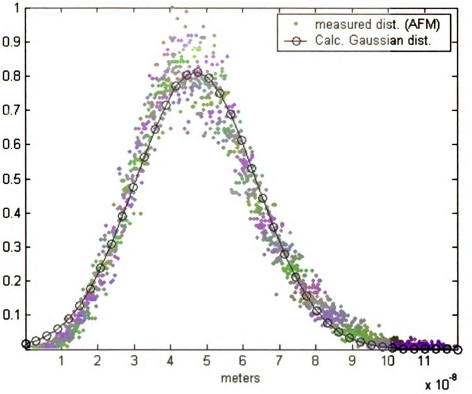

Figure 6.10 Distribution for AFM Image 3 from RB2K8.

For AFM Image 3, the measured mean is 48.166nm, the measured standard deviation is 16.727nm, the measured skewness is 0.4238, and the measured kurtosis is 3.1469.

6.6.4 AFM Image 4: FB26-1

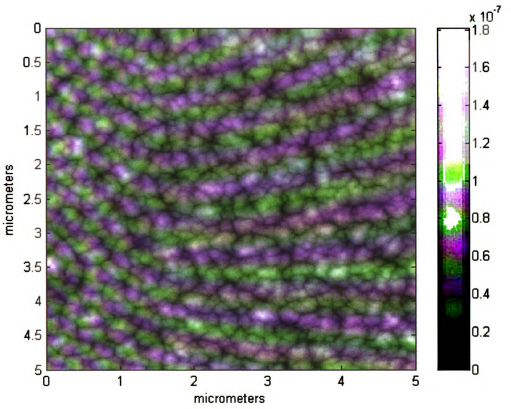

Figure 6.11 AFM Image 4.

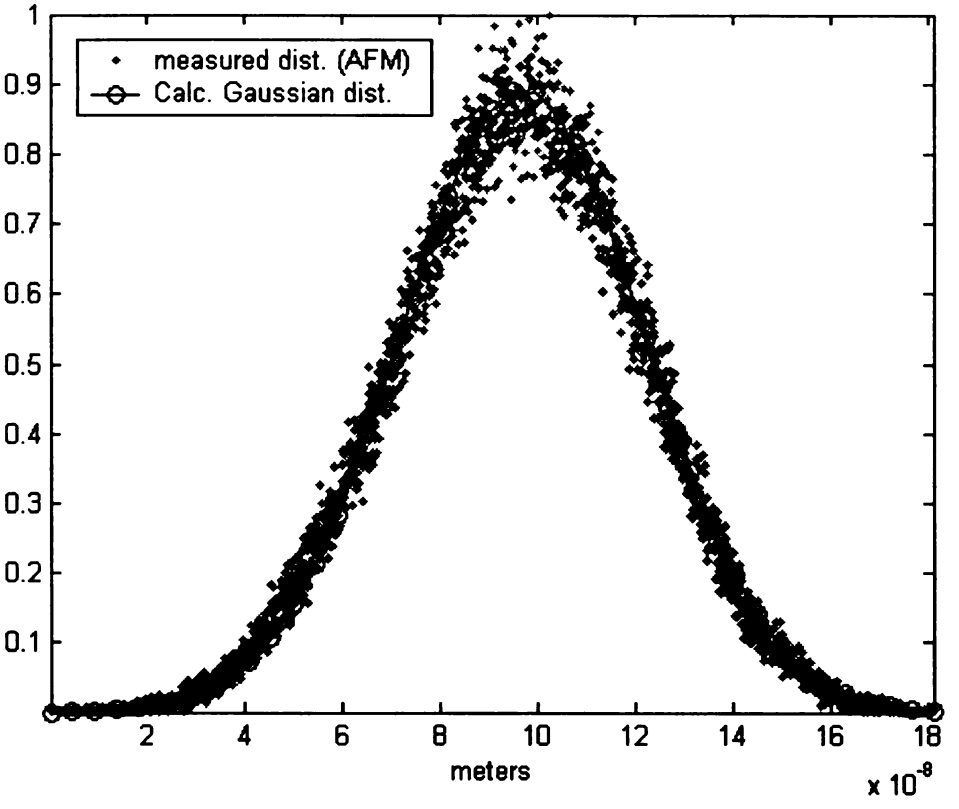

Figure 6.12 Distribution for AFM Image 4 from FB26.

For AFM Image 4, the measured mean is 95.870nm, the measured standard deviation is 25.068nm, the measured skewness is -0.0723, and the measured kurtosis is 2.8521.

6.6.5 AFM Image 5: FB26-2

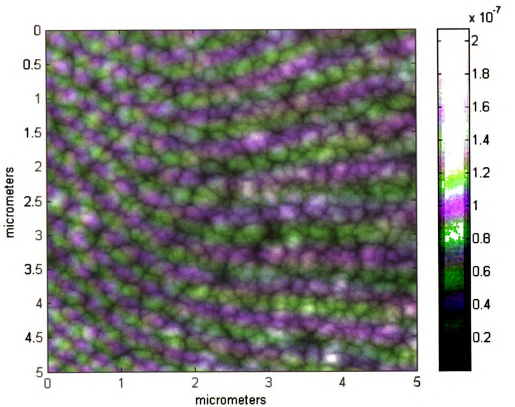

Figure 6.13 AFM Image 5.

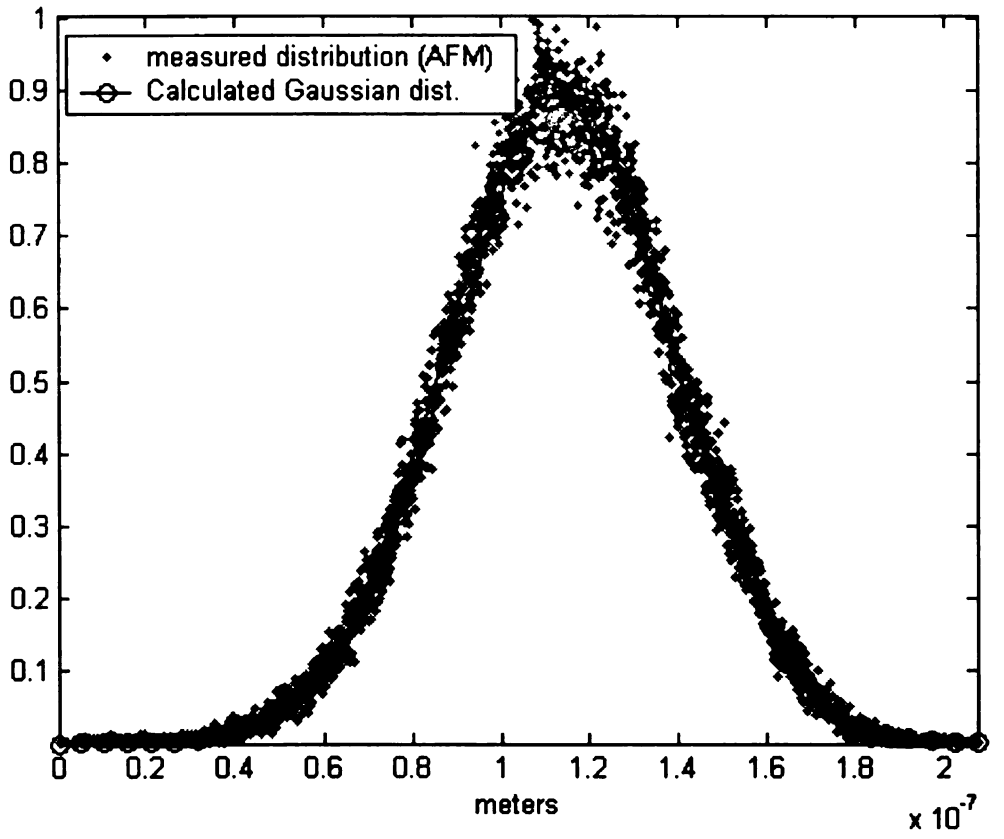

Figure 6.14 Distribution for AFM Image 5 from FB26.

For AFM Image 5, the measured mean is 113.22nm, the measured standard deviation is 25.592nm, the measured skewness is –0.0840, and the measured kurtosis is 2.9184.

6.6.6 AFM Image 6: FB26-3

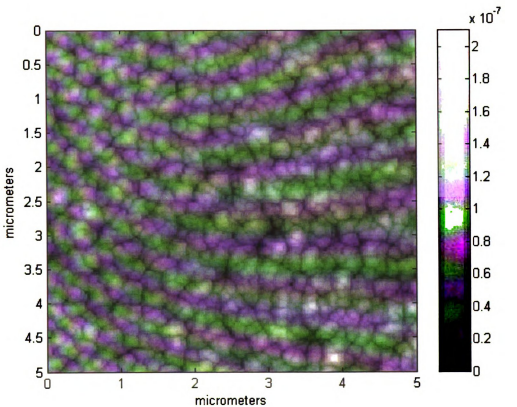

Figure 6.15 AFM Image 6.

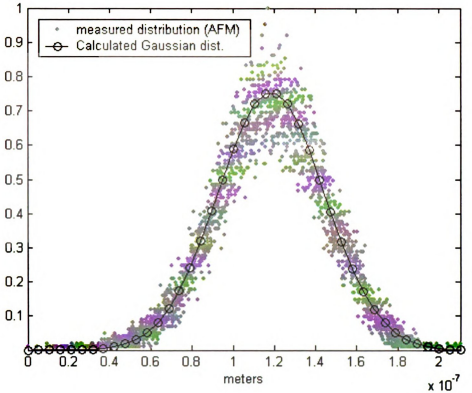

Figure 6.16 Distribution for AFM Image 6 from FB26.

For AFM Image 6, the measured mean is 118.39nm, the measured standard deviation is 26.061nm, the measured skewness is –0.1290, and the measured kurtosis is 2.9908.

6.6.7 AFM Image 7: FB26-4

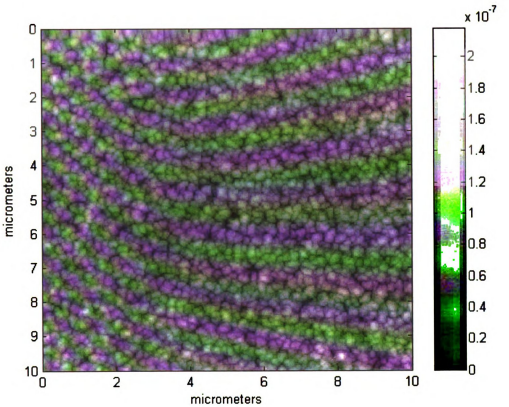

Figure 6.17 AFM Image 7.

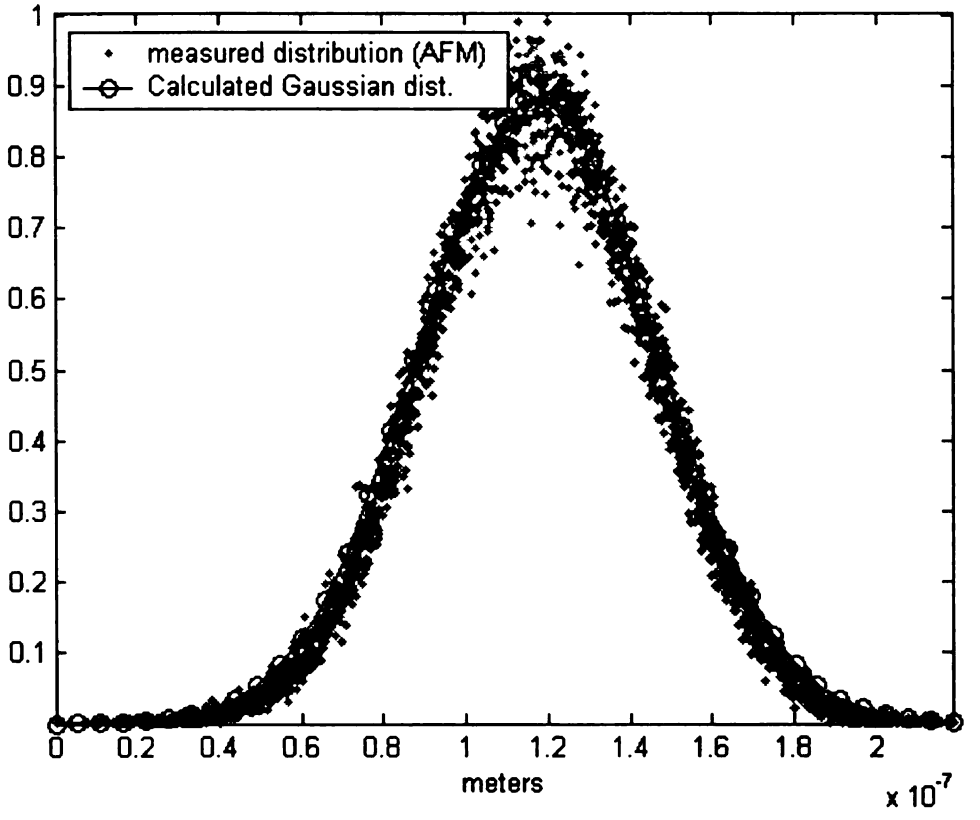

Figure 6.18 Distribution for AFM Image 7 from FB26.

For AFM Image 7, the measured mean is 117.57nm, the measured standard deviation is 28.930nm, the measured skewness is –0.0384, and the measured kurtosis is 2.8918.

6.6.8 AFM Image 8: FB26-5

AFM Image 8 is shown in Figure 6.2. The distribution calculated from the image is shown below.

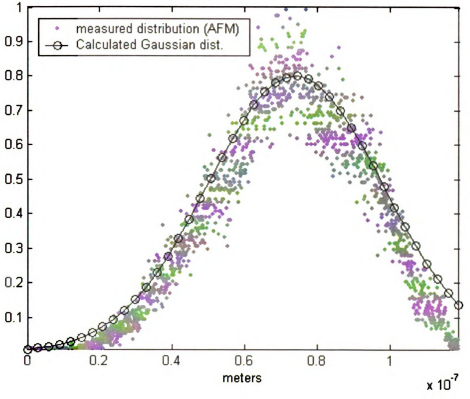

Figure 6.19 Distribution for AFM Image 8 from FB26.

For AFM Image 8, the measured mean is 72.428nm, the measured standard deviation is 24.106nm, the measured skewness is –0.1708, and the measured kurtosis is 2.5308. Since relatively few grains are shown in AFM Image 8, these statistics probably have somewhat less meaning than previous images of this sample.

6.6.9 AFM Image 9: FB26-6

AFM Image 9 is shown in Figure 6.3. The distribution calculated from this image is shown below.

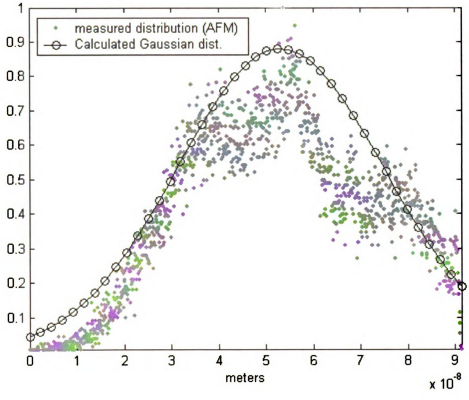

Figure 6.20 Distribution for AFM Image 9 from FB26.

For AFM Image 9, the measured mean is 53.024nm, the measured standard deviation is 21.762nm, the measured skewness is 0.0605, and the measured kurtosis is 2.2014. Again, since relatively few grains are shown in AFM Image 9, these statistics probably have somewhat less meaning than previous images of this sample.

6.6.10 AFM Image 10: RB2K9-1

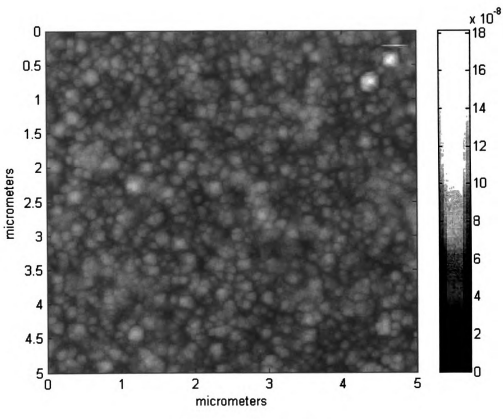

Figure 6.21 AFM Image 10.

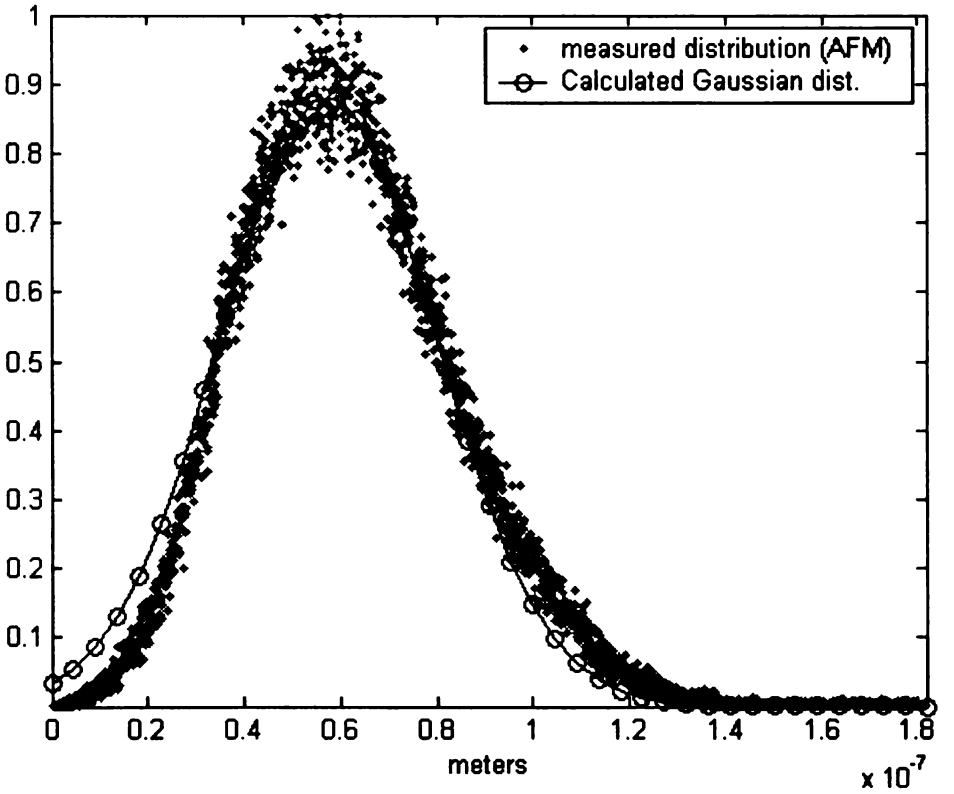

Figure 6.22 Distribution for AFM Image 10 from RB2K9.

For AFM Image 10, the measured mean is 81.598 nm, the measured standard deviation is 29.604 nm, the measured skewness is 0.4948, and the measured kurtosis is 3.5080.

6.6.11 AFM Image 11: RB2K9-2

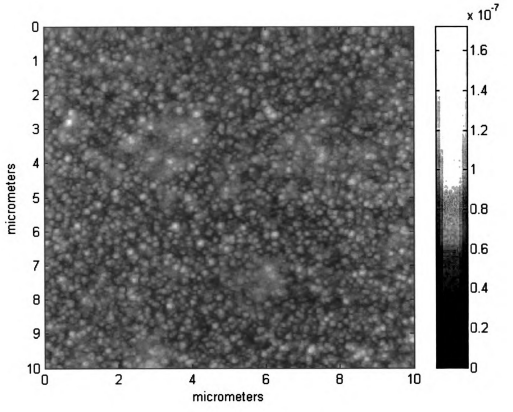

Figure 6.23 AFM Image 11.

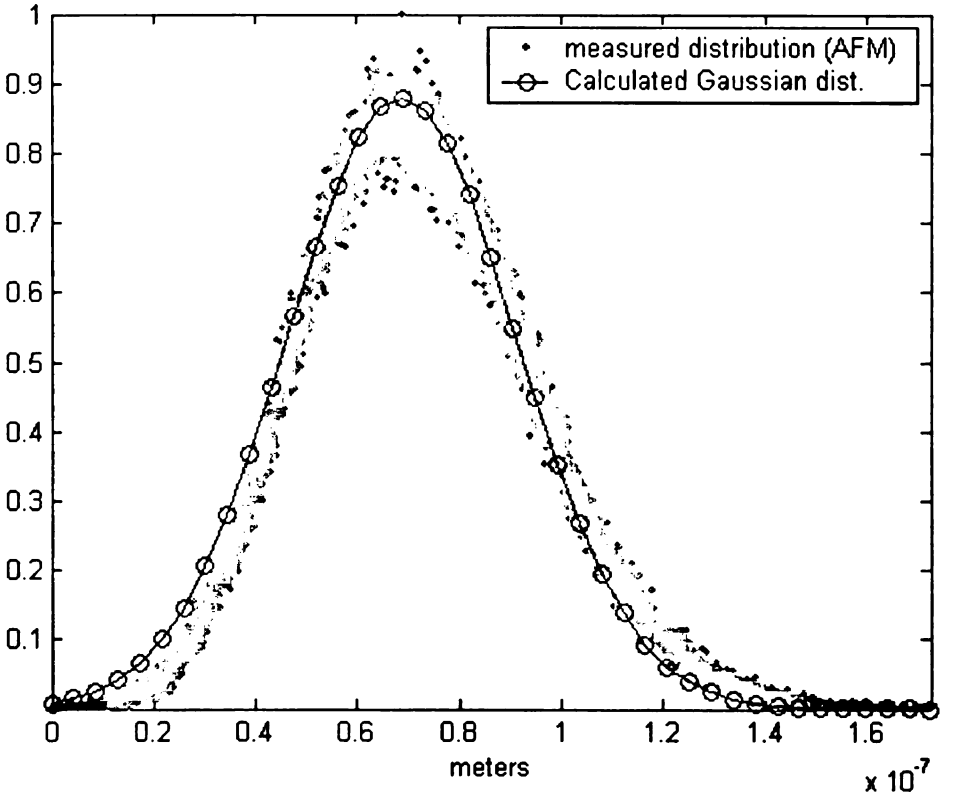

Figure 6.24 Distribution for AFM Image 11 from RB2K9.

For AFM Image 11, the measured mean is 84.198 nm, the measured standard deviation is 26.151 nm, the measured skewness is 0.3172, and the measured kurtosis is 3.0308.

6.6.12 AFM Image 12: RB2K9-3

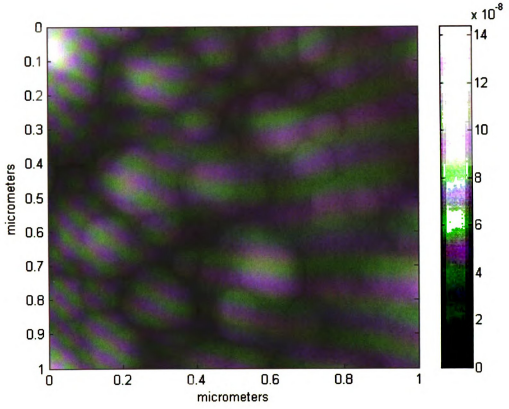

Figure 6.25 AFM Image 12.

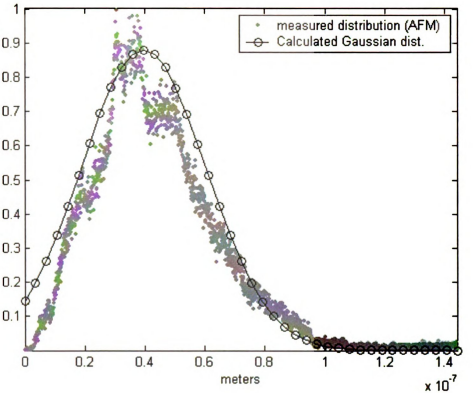

Figure 6.26 Distribution for AFM Image 12 from RB2K9.

For AFM Image 12, the measured mean is 61.117 nm, the measured standard deviation is 28.944 nm, the measured skewness is 0.9593, and the measured kurtosis is 4.8004. Since relatively few grains are shown in AFM Image 12, these statistics probably have somewhat less meaning than previous images of this sample.

6.6.13 AFM Image 13: RB2K9-4

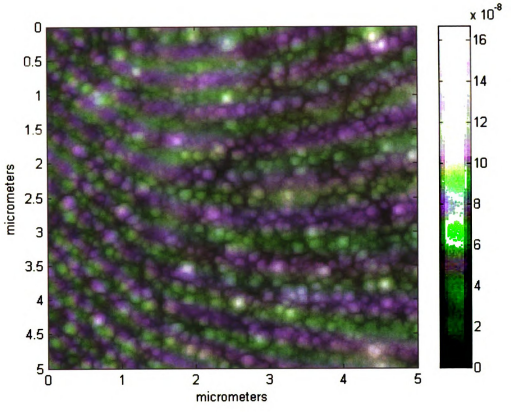

Figure 6.27 AFM Image 13.

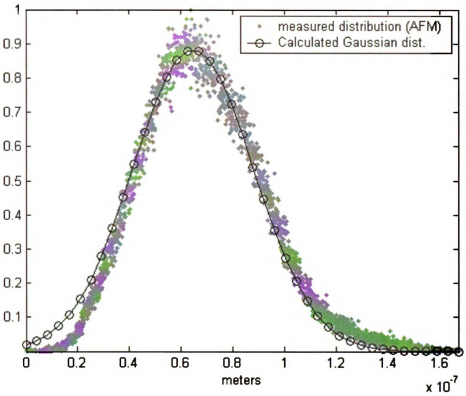

Figure 6.28 Distribution for AFM Image 13 from RB2K9.

For AFM Image 13, the measured mean is 81.004 nm, the measured standard deviation is 27.504 nm, the measured skewness is 0.4523, and the measured kurtosis is 3.2733.

6.6.14 AFM Image 14: RB2K9-5

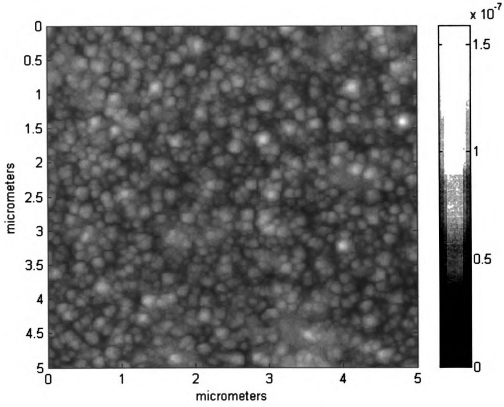

Figure 6.29 AFM Image 14.

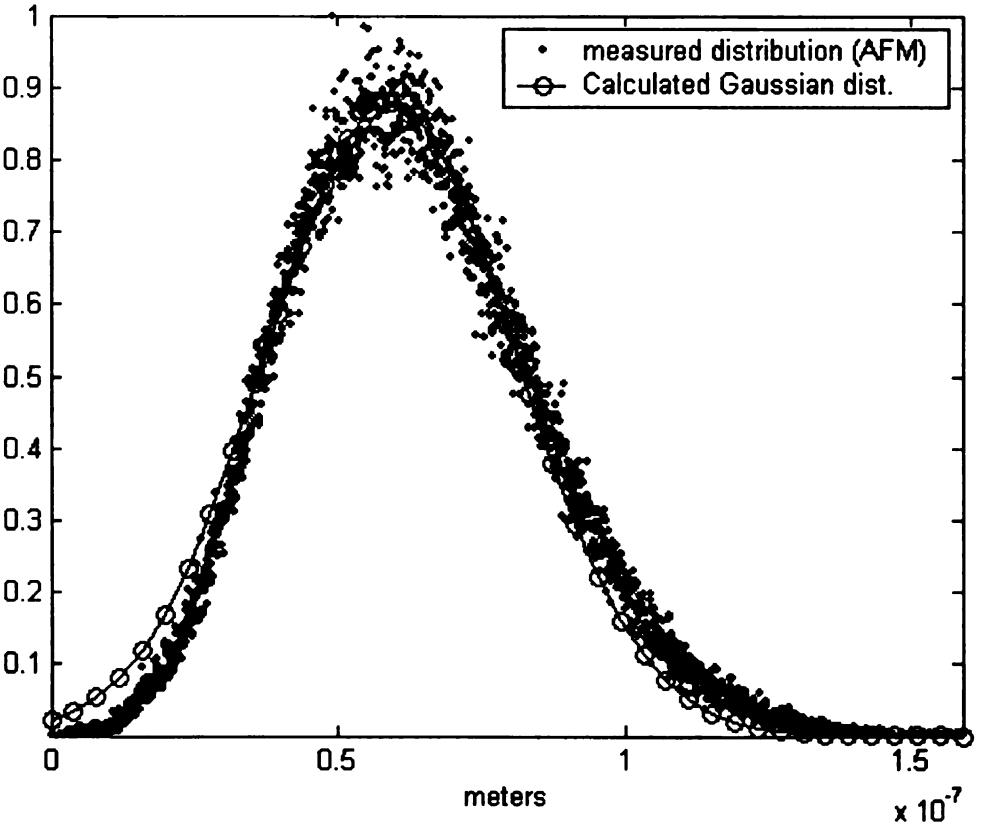

Figure 6.30 Distribution for AFM Image 14 from RB2K9.

For AFM Image 14, the measured mean is 76.164 nm, the measured standard deviation is 26.226 nm, the measured skewness is 0.3731, and the measured kurtosis is 3.0048.

6.6.15 AFM Image 15: RB2K9-6

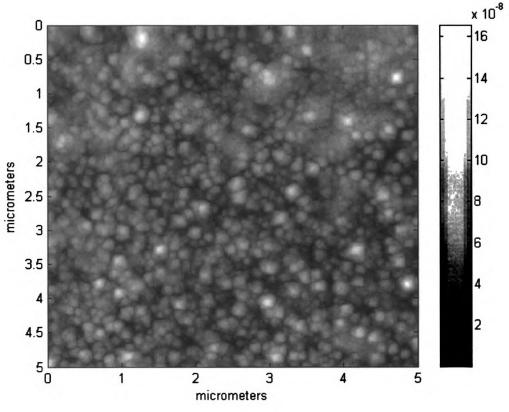

Figure 6.31 AFM Image 15.

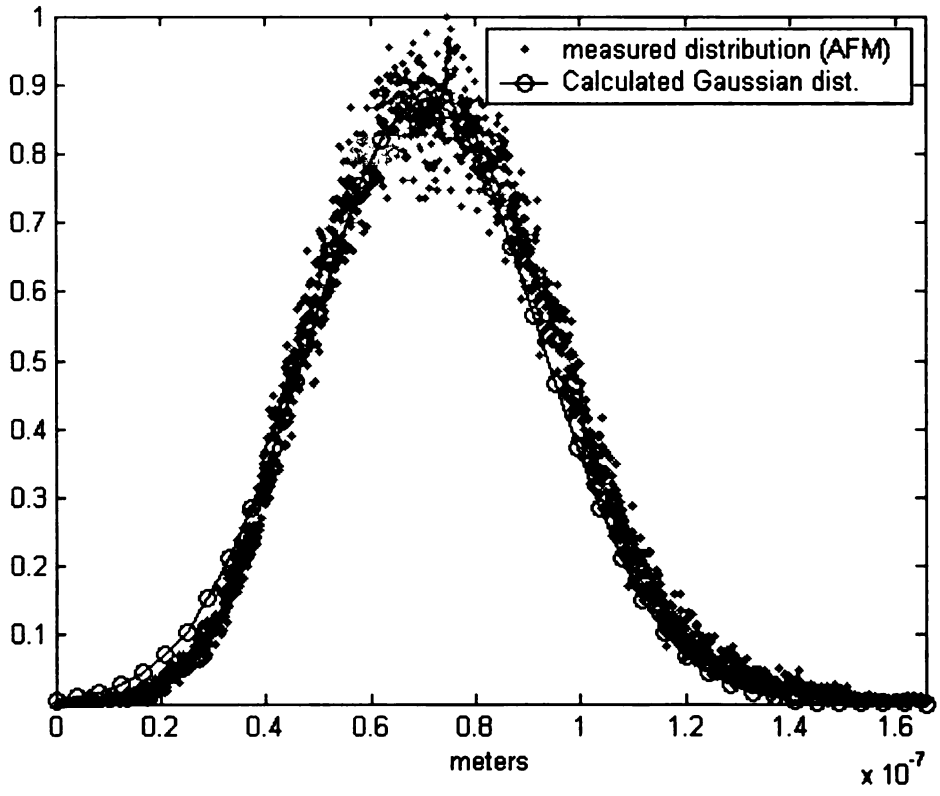

Figure 6.32 Distribution for AFM Image 15 from RB2K9.

For AFM Image 15, the measured mean is 81.842 nm, the measured standard deviation is 24.667 nm, the measured skewness is 0.2825, and the measured kurtosis is 3.0553.

6.6.16 Measurement Summary

Nine images have been shown and their distributions analyzed. A Table 6.1 summarizes the measurements of RB2K8. Recall that RB2K8 has a nominal thickness of 1.5μm, based on optical transmission measurements.

	RB2K8-1	RB2K8-2	RB2K8-3	Average
Mean (nm)	46.373	46.668	48.166	47.069
Std. Dev. (nm)	14.070	16.882	16.727	15.893
Skewness	0.4424	0.5253	0.4238	0.4638
Kurtosis	3.4155	3.4619	3.1469	3.3414

Table 6.1 Summary of RB2K8 AFM measurements.

Table 6.2 summarizes the measurements taken on FB26. FB26 has a nominal thickness of 1.4μm based on optical transmission measurements. Since images 5 and 6 contain significantly fewer grains than the first four images and their statistics may therefore be less meaningful, an average of the first four images only is also shown.

	FB26-1	FB26-2	FB26-3	FB26-4	FB26-5	FB26-6	Average	Average of first four
Mean (nm)	95.870	113.22	118.39	117.57	72.428	53.024	95.084	111.263
Std. Dev. (nm)	25.068	25.592	26.061	28.930	24.106	21.762	25.253	26.413
Skewness	-0.0723	-0.084	-0.129	-0.0384	-0.1708	0.0605	-0.0723	-0.08093
Kurtosis	2.8521	2.9184	2.9908	2.8918	2.5308	2.2014	2.7309	2.9133

Table 6.2 Summary of FB26 AFM measurements.

Table 6.3 summarizes the measurements taken on RB2K9. RB2K9 has a nominal thickness of about 0.9μm based on optical transmission measurements. Since image 3 from this series contains significantly fewer grains than the other images and its statistics may therefore be less meaningful, an average of the images not including image 3 is also shown.

	RB2K9-1	RB2K9-2	RB2K9-3	RB2K9-4	RB2K9-5	RB2K9-6	Average	Average of w/o RB2K9-3
Mean (nm)	61.761	72.639	43.989	68.715	63.049	73.349	63.917	67.903
Std. Dev. (nm)	22.407	22.561	20.812	23.332	21.710	22.107	22.155	22.423
Skewness	0.4948	0.3172	0.9593	0.4523	0.3731	0.2825	0.4799	0.3840
Kurtosis	3.5080	3.0308	4.8004	3.2733	3.0048	3.0553	3.4454	3.1744

Table 6.3 Summary of RB2K9 AFM measurements.

It should again be noted that the mean value is listed in these tables only for completeness, and it does not have any direct significance for purposes of this research.

It is interesting to observe that even though they were deposited under similar conditions, the films seem to have some noticeable differences in their statistics. First of all, FB26 appears to be much closer to an ideal Gaussian shape, since it's skewness and kurtosis are both very small in magnitude, while RB2K8 shows almost five times more skewness and kurtosis than FB26. RB2K9 shows greater surface roughness than RB2K8, but like FB26, it shows less skewness and kurtosis than RB2K8.

Also, FB26 is significantly rougher than RB2K8 and RB2K9, having an average standard deviation of around 26nm compared to RB2K8's 16nm average and RB2K9's 22nm average. It is also worth noting that RB2K8 appears to be slightly rougher when

extracting the roughness from optical measurements than when measured via AFM. The optical fit resulted in a surface roughness range of 19nm - 25nm, whereas the AFM range was 14 - 17nm. This may be due in part to the fact that the parameter extractions in Chapter 5 assumed a pure Gaussian and the "extra" roughness compensates for the lack of higher order moments in the distribution. Also, the optical measurements deal with two surfaces and other effects, such as inter-grain boundaries and absorption in the diamond film, which are not included in the AFM measurement. These effects may also lead to measuring "extra" surface roughness optically.

However, RB2K9 appears to be rougher when measured with the AFM than when extracting the roughness from optical measurements. This is may be due in part to the fact that the surface of RB2K9 appeared to have some impurities present at the time of the AFM measurement. The presence of these impurities is speculative, since the AFM, as it was used for collecting these images, is purely a topographical tool, and has no means of chemical or electrical analysis. The surface of the sample was cleaned with alcohol and a cotton tipped swap, but the apparent presence of foreign objects in the image remained nonetheless.

Whether or not the objects on the surface of the sample are impurities, it can be seen that excluding them in the surface roughness calculation leads to values similar to RB2K8.

6.7 Including Higher Order Moments in Optical Simulations

It is interesting to consider how the skewness and kurtosis of the distribution may influence the modeling of optical transmission through the device. Section 6.5 discussed how the mean, surface roughness, skewness and kurtosis were calculated from the surface height data measured by the AFM. This section shows how to reconstruct an analytical distribution given those parameters. The Pearson Type-IV distribution[5] allows one to specify skewness and kurtosis in addition to the mean and standard deviation and calculate a distribution based on those parameters. The non-normalized Pearson Type-IV distribution as a function of x is given by the following set of equations:

$$n(x) = \exp\left(A - B\tan^{-1} C\right) \qquad [6.5]$$

where A is:

$$A = \frac{\ln\left(b_0 + b_1(x - x_{mean}) + b_2(x - x_{mean})^2\right)}{2b_2} \qquad [6.6]$$

and B is:

$$B = \frac{b_1 + 2b_1 b_2}{\sqrt{4b_0 b_2^3 - b_1^2 b_2^2}} \qquad [6.7]$$

and C is:

$$C = \frac{2b_2(x - x_{mean}) + b_1}{\sqrt{4b_0 b_2 - b_1^2}} \qquad [6.8]$$

and b_0 is:

$$b_0 = -\frac{\sigma^2\left(4\beta - 3\gamma^2\right)}{10\beta - 12\gamma^2 - 18} \qquad [6.9]$$

and b_1 is:

$$b_0 = -\frac{\gamma\sigma(\beta+3)}{10\beta-12\gamma^2-18} \qquad [6.10]$$

and b_2 is:

$$b_2 = -\frac{2\beta-3\gamma^2-6}{10\beta-12\gamma^2-18} \qquad [6.11]$$

In these expressions, γ is the skewness, and β is the kurtosis. However, there are constraints upon the skewness and kurtosis for equation [6.5] to produce a real distribution. If the constraints are not met, equation [6.5] produces complex values which are not physically acceptable. The constraints on the skewness and kurtosis are[6]:

$$0 \prec \gamma^2 \prec 32 \qquad [6.12]$$

and,

$$\beta \succ \frac{39\gamma^2+48+6\cdot\left(\gamma^2+4\right)^{3/2}}{32-\gamma^2} \qquad [6.13]$$

The constraints should not be interpreted as meaning that values of skewness and kurtosis outside of these constraints are not physically possible, simply that equation [6.5] does not work when the constraints are not met. In order to present these constraints in a more intuitive manner, Figure 6.33 shows a plot of β_{min} as a function of γ.

Experimenting with MATLAB shows that the values of β_{min} calculated for Figure 6.33 are somewhat low, and typically about 3% extra must be added to β_{min} in order to avoid numerical issues in the calculation, which results in small imaginary parts being present in the calculated distribution.

However, Figure 6.33 does show that the Pearson Type-IV distribution should be useful for investigating the ranges of skewness and kurtosis found in the Fabry-Perot films for this research, although modeling using the exact statistics measured from the distributions may not be possible. Although RB2K8 has statistics that meet the constraints shown in Figure 6.33, FB26 shows a kurtosis of less than 3, which cannot be modeled by equation [6.5]. Also, RB2K9 shows skewness on the order of 0.4, but a kurtosis on the order of 3.2. A skewness on the order of 0.4 means that kurtosis should be at least 3.3 for equation [6.5] to be used, so the exact statistics extracted from measurements on RB2K9 are not within the acceptable range to be modeled with the distribution in this section. However, using values close to those extracted from the RB2K9 AFM measurements in the optical simulations can still provide some insight into this work.

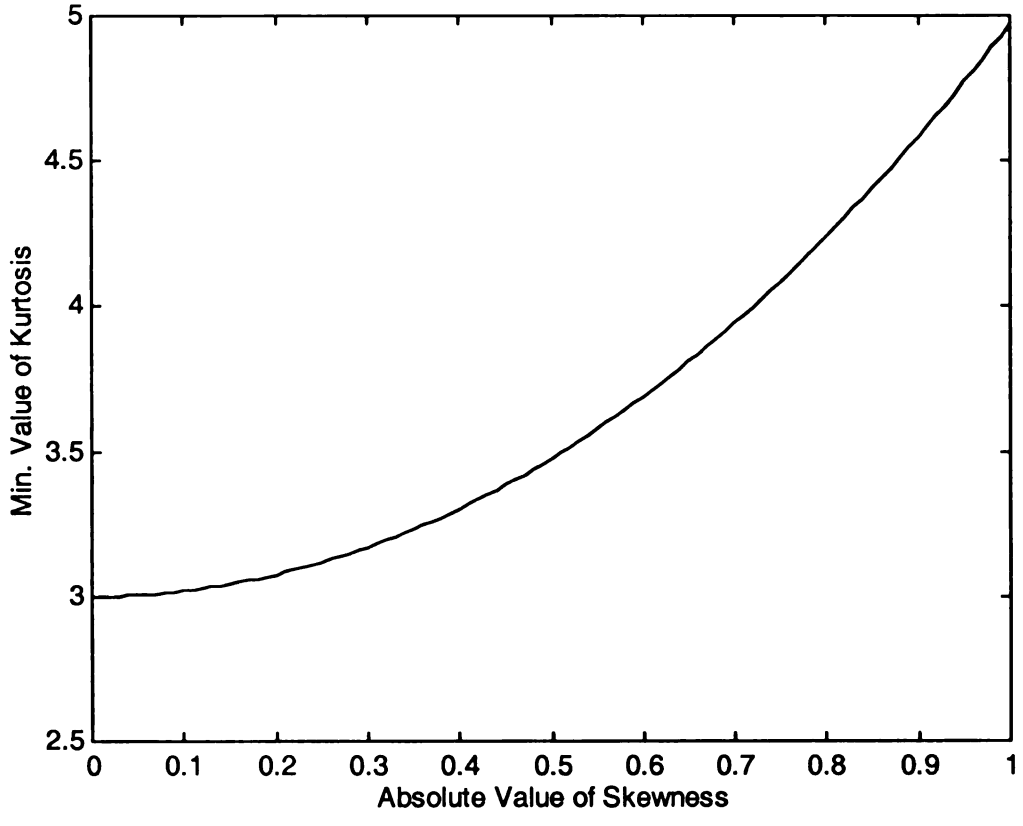

Figure 6.33 Plot of the constraint on Kurtosis as a function of Skewness for Equation [6.5].

Figures 5.9 and 5.12, which are measurements on diamond window 5, serve as a basis for the investigation into higher order moments. This film is on the RB2K9 wafer. Figure 6.34 shows a fit of the Pearson Type IV distribution to the measured distribution of Figure 6.24. The parameters used in this calculation are a mean value of 72nm, a standard deviation of 22.5nm, a skewness of 0.3172 and a kurtosis value of 3.75. The value for kurtosis is not exactly the same as the measured value of 3.0308 since the measured values of skewness and kurtosis do not fit the constraints on equation [6.5]. Notice, though, that the Pearson distribution fits the measurement much better than the Gaussian distribution in Figure 6.24.

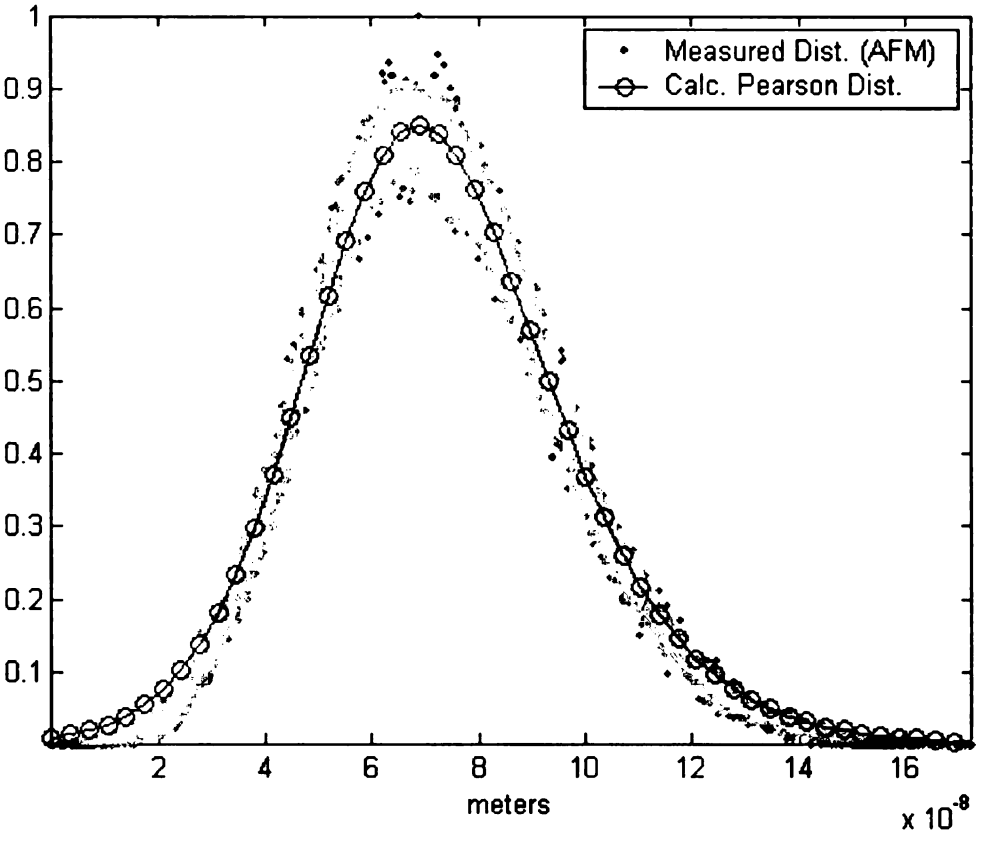

Figure 6.34 Measured distribution from AFM Image 11 compared to calculated Pearson Type-IV distribution.

Figure 6.35 shows the transmission through the diamond film alone, analogous to measurement and simulation shown in Figure 5.9. Using the pure Gaussian distribution in the simulation in Chapter 5, this film was determined to be 1.06μm thick, and have a surface roughness of 18nm RMS.

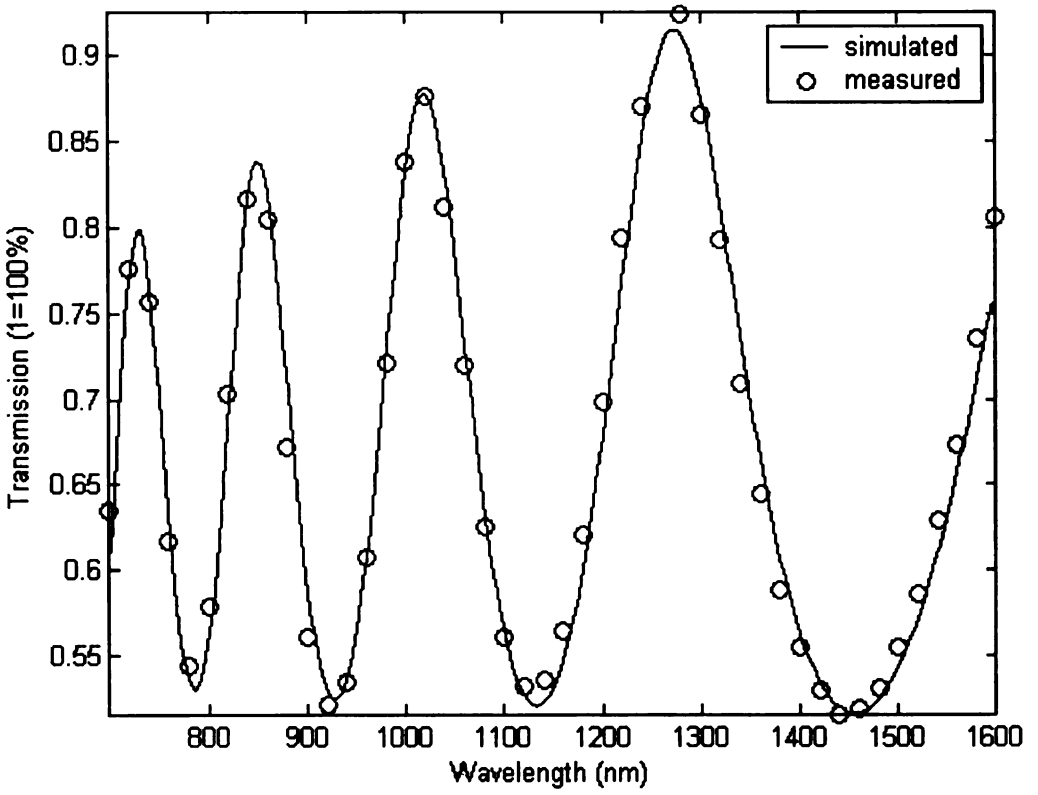

Figure 6.35 Measured and simulated transmission through a diamond window, simulation includes surface roughness, skewness, and kurtosis.

The simulation in Figure 6.35 shows uses a skewness of 0.38 and a kurtosis of 3.4. The skewness is the average of the measured values for RB2K9. The kurtosis is more than the measured value of 3.17, but it is the closest value which satisfies the constraints on equation [6.5]. Using these values of skewness and kurtosis in the simulation, the mean value is fit to be 1.069μm. The surface roughness, again, is 18nm RMS.

Figure 6.36 shows a measurement and simulation analogous to Figure 5.12. Here, the simulation includes the exact values of thickness, surface roughness, skewness and

kurtosis given in the preceding paragraph, but the simulation now has gold coatings included in the calculation.

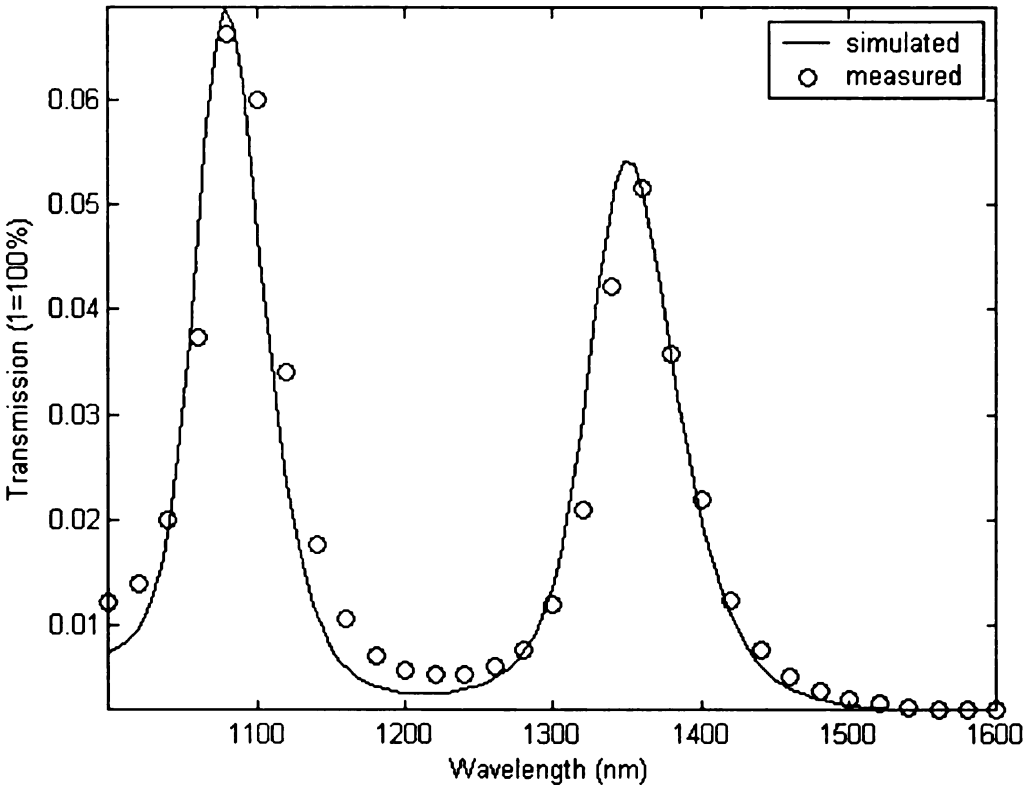

Figure 6.36 Measurement and simulation of a Fabry-Perot resonator, with surface roughness, skewness, and kurtosis considered.

The thicknesses of the gold films used in this simulation are 23nm and 27nm as they were in the simulation for Figure 5.12. The most notable difference between this calculation and that of Figure 5.12 is that the presence of the higher order moments in the distribution has shifted the mean value of the film thickness, and the peaks in the simulation now align better with the measurement than in the Chapter 5 simulation. The Q values are similar in this simulation to those in Figure 5.12, around 19 the longer

wavelength peak and 20 for the shorter wavelength peak, as compared to about 20 for each peak using a pure Gaussian distribution to model the surface roughness.

For comparison, Figure 6.37 shows both simulations for transmission, that is, using a pure Gaussian, and using a Pearson Type-IV distribution, with the skewness and kurtosis as mentioned above.

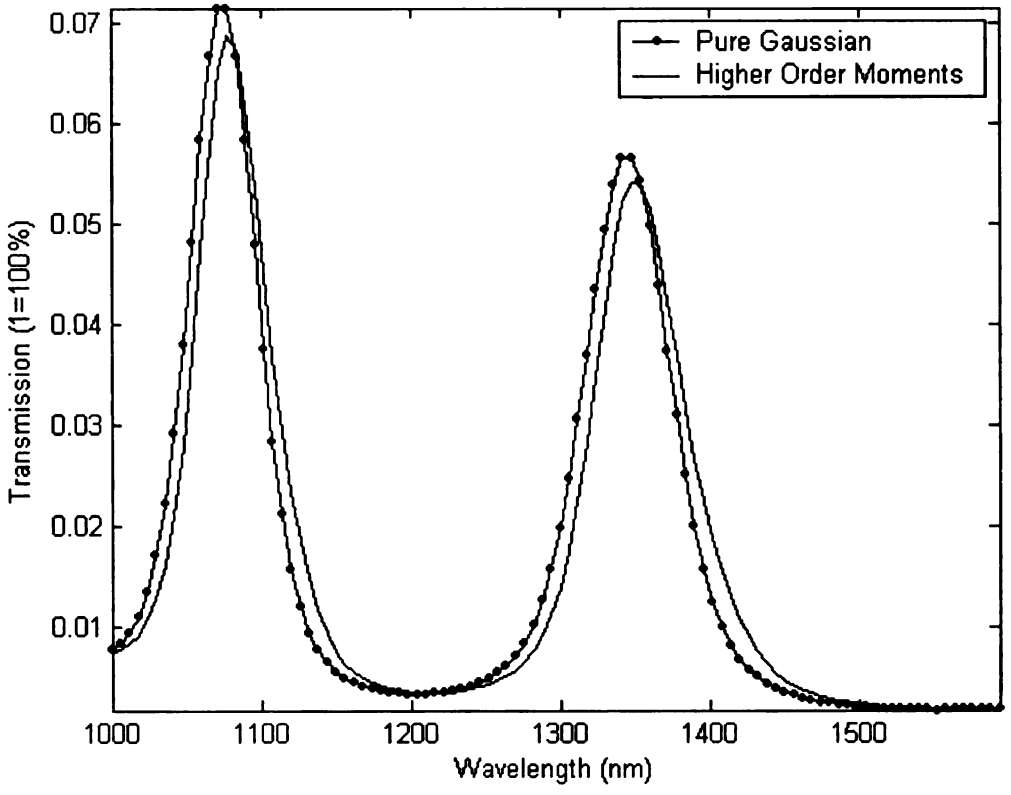

Figure 6.37 Comparison of simulations using a pure Gaussian, and a Pearson Type-IV distribution.

6.8 Conclusions

In this section, AFM was employed to directly measure the surface heights of the diamond films. From this surface height data, distributions can be calculated. Most of the measured distributions showed nearly ideal Gaussian behavior, although small

amounts of skewness and kurtosis were present in every measurement. Previous simulations had assumed pure Gaussian distributions in modeling the surface heights of the diamond film. In this chapter, a more advanced distribution was investigated which included higher order moments. It was found that the addition of the higher order moments weigh heavily upon the characteristics of the completed Fabry-Perot resonators, while affecting the optical transmission results of the uncoated diamond window to a much lesser extent. When fitting the pure Gaussian to the measured distributions, it is observed that a slightly smaller or larger mean must be used than is measured, depending upon the skewness of the distribution. The inclusion of skewness and kurtosis in the optical model results in the extraction of a different mean than the model employing a pure Gaussian does. The different mean results in a shift of the wavelength of the resonator, which can lead to an improved fit between simulation and measurement. Further AFM investigation of the RB2K9 sample may help improve modeling results, as the skewness and kurtosis of this sample cannot be modeled with the Pearson Type IV distribution as employed in this work.

References:

[1] *NIST/SEMATECH e-Handbook of Statistical Methods*, http://www.itl.nist.gov/div898/handbook/, 2003.

[2] J. F. Kenney and E. S. Keeping, Mathematics of Statistics 3rd Edition, D. Van Nostrand Company, Princeton, NJ, 1954.

[3] M. R. Spiegel, Schaum's Outline of Theory and Problems of Statistics, McGraw-Hill Book Company, New York, NY, 1961.

[4] J. K. Lindsey, Parametric Statistical Inference, Oxford University Press, Inc., New York, NY, 1996.

[5] See Chapter 3 Ref. 3 (Campbell).

[6] Plasun, Richard, Optimization of VLSI Semiconductor Devices, PhD Dissertation, Vienna University of Technology, 1999.

Chapter 7: Conclusions and Future Work

7.1 Conclusions

Many conclusions can be drawn from the present state of this research. The most challenging conclusion is from Chapter 5, where the modeling of the device shows that high Q values are not probable with the as-grown surface roughness of the diamond film. Since diamond is amongst the hardest materials known, polishing the film after the deposition is not a trivial undertaking and is beyond the scope of this work. However, it has been shown that polycrystalline diamond films can be polished to under 2nm RMS surface roughness[1], so this implies that the device presented in this thesis could achieve excellent Q values with the addition of some post-processing of the diamond film.

A second important conclusion is that the model presented in Chapter 4 is an improvement in accuracy over existing models in the literature. It was shown that present models in the literature improperly solve an integral which leads to a model that does not accurately track the phase of the wave inside the optical thin film. Additionally, the model in Chapter 4 allows the use of an arbitrary distribution, which is an improvement over models which build in the use of a Gaussian distribution. Chapter 6 makes use of this fact by using a Pearson Type-IV distribution to model the surface roughness, instead of a pure Gaussian.

In Chapter 3, the fabrication techniques presented lead to a functional Fabry-Perot device, and large-area, free-standing polycrystalline diamond films. This work is already leading to new applications, as the fabrication sequences of Chapter 3 were used to create even larger free-standing films, used as electron spalation foils in the MSU Cyclotron[2].

Chapter 6 shows an interesting result regarding the statistics of the distribution used to model the surface roughness of the diamond film. It is observed that the inclusion of skewness and kurtosis in the distribution used to model the surface roughness can improve the fit between the simulation and the optical measurement of the device.

7.2 Future Work

This work leaves many interesting avenues to be explored, both in the fabrication of the device and in the simulation of the optical performance of the device.

7.2.1 Future Fabrication Work

Several new technologies have become available at MSU since the beginning of this work, which could improve the performance and ease of manufacture of the device. Two systems are of particular interest, one is an electron beam PVD system with 2 sputtering sources, and the second system is a PECVD system capable of depositing oxides and nitrides.

The PECVD system is of interest because it offers a low temperature deposition method of coating the wafer with oxide. Also, this means that during the oxide etch, only the patterned side of the wafer would need to be etched. Additionally, the use of MEMS techniques or even a simple shadow mask means that the oxide-etch could possibly be eliminated altogether.

The PVD system is of interest because of its ability to coat the sample with many different materials, including dielectric materials. This opens up the possibility of using a material other than gold to form the partially transparent reflective layers on the sample. If the loss in the gold could be eliminated, the transmission of the device could be significantly improved. Additionally, it may be possible to use a stack of materials with alternating indices of refraction to form highly reflecting, but lossless mirrors. Although the surface roughness of the diamond film would still be a limiting factor, significant gains in performance may still be possible.

Another interesting avenue for exploration is the use of ultra-nano crystalline diamond films. These 10-100nm grain size films appear to be somewhat smoother than the ~250nm grain sized films used in this research. Additionally, these films appear to maintain small amounts of as-grown surface roughness independent of film thickness. By equation [2.5], the use of a thicker film directly increases Q for an ideal resonator. This appears to hold true for non-ideal resonators, as the two resonators studied in Chapter 5 follow this trend. The resonator in Figure 5.12 shows Q values almost double

those observed in Figure 5.11, and the film in Figure 5.12 is almost twice as thick as that in Figure 5.11.

Finally, as previously mentioned, polishing the diamond films to 5nm RMS surface roughness or less should result in excellent Q values according to Figure 5.13. Polishing the film combined with reflective coatings less absorbing than gold and thicker diamond films could lead to Q values many times higher than those achieved in this thesis.

7.2.2 Future Work with Modeling

Despite the inclusion of the higher order moments in the distribution representing the surface roughness in Chapter 6, the model developed in this thesis is still relatively simple. For example, it assumes zero correlation length in the distribution.

Some future avenues to explore with the modeling would be to include a non-zero correlation length in the simulation. Beckmann does this with a Gaussian distribution, although none of the references cited in this work for the Pearson Type IV distribution make any mention of correlation length.

Additionally, near field effects are neglected by this treatment of surface roughness. More sophisticated models, which incorporate near field effects, may improve the accuracy of the simulation presented here.

Another issue is that the diamond film is considered lossless by this treatment, although it is known that this is not strictly the case. At a minimum, grain boundaries exist within the diamond film which may contain sp^2 bonds. Other imperfections may well exist within the individual grains as discussed in Chapter 2. For example, small amounts of graphite or non-diamond carbon within grains, and the incorporation of small amounts of feed gasses into the diamond lattice are all possibilities which are not considered with the present model. The separation of the losses due to non-zero extinction coefficient and those losses due to scattering are also an important area for future research.

References:

[1] J.A. Weima, R. Job, W.R. Fahrner, G.C. Kosaca, N. Muller, and T. Fries, "Surface Analysis of ultraprecise polished chemical vapor deposited diamond films using spectroscopic and microscopic techniques", Journal of Applied Physics, Vol 89, No 4, Feb 2001

[2] D.K. Reinhard, M. Becker, R. A. Booth, T. P. Hoepfner, T. A. Grotjohn, J. Asmussen, "Fabrication and Properties of Ultra-nano, Nano, and Polycrystalline Diamond Membranes and Sheets", AVS 50th International Symposium, Baltimore, MD, USA, Nov 3rd -7th 2003

APPENDICES

Appendix A: MATLAB Programs

Below is the code for the 'modexamp.m' MatLab program. This program simulates transmission through a slab of diamond with one rough surface, using the MacLeod matrix method as discussed in Chapter 2.

```
clear

% enter the nominal thickness of the diamond in meters
dnom=1.0*10^-6;

% let the incident medium be air
n1=1;

% let the final medium also be air
n3=1;

% diamond will be the middle medium, and it's index of refraction
% will need to be calculated with the sellmeier equation on the fly

% set up the weighting scheme
%%%%%%%%%%%%%%%%%%%%%%%%%%%%%%%%%%%

% roughness of film (RMS) aka standard deviation
sigma=30*10^-9;

dstart=dnom-(4*sigma);
dstop=dnom+(4*sigma);

dpp=10;

incrp=(dstop-dstart)/dpp;
```

```
nm=0;

for n=1:dpp+1;
    d(n)=dstart+((n-1)*incrp);
    term1=((d(n)-dnom)^2)/(2*(sigma^2));
    dt(n)=exp((-1)*term1);
    nm=nm+dt(n);
end

dt=dt./nm;

hold off
figure(1)
plot(d,dt,'o')

%%%%%%%%%%%%%%%%%%%%%%%%%%%%%%%%%%%%%%%%%%%%%%%
% start the loop to calculate transmission

numpoints=400;

lamstart=400*10^-9;
lamstop=1600*10^-9;
incr=(lamstop-lamstart)/numpoints;

for n=1:numpoints+1;
    lam(n)=lamstart+(n-1)*incr;
    lamu(n)=lam(n)*1e6;
    trm1=(0.3306*(lamu(n))^2)/(((lamu(n))^2)-0.175*0.175);
    trm2=(4.3356*(lamu(n))^2)/(((lamu(n))^2)-0.106*0.106);
    n2(n)=sqrt(1+trm1+trm2);

    % now we need to do another loop...

    Tp(n)=0;
        for j=1:dpp;

            phiair(j)=(2*pi*n1*(d(dpp)-d(j)))/lam(n);
```

```
            air=[cos(phiair(j)) (i*sin(phiair(j)))/n1;
i*n1*sin(phiair(j)) cos(phiair(j))];

            phid(j)=(2*pi*n2(n)*d(j))/lam(n);
            D=[cos(phid(j)) (i*sin(phid(j)))/n2(n);
i*n2(n)*sin(phid(j)) cos(phid(j))];

            BC=air*D*[1;n3];
            B=BC(1);
            C=BC(2);
            t=(2*n1)/((n1*B)+C);
            Tp(n)=Tp(n)+(dt(j)*t);

        end
    Tr(n)=Tp(n)*conj(Tp(n));

end

figure(2)

% This will now plot the transmission
plot(lam,Tr,'r')

xlabel('Wavelength')
ylabel('Transmission')
title('modexamp.m')
```

Below is the code for the 'tranmat.m' MatLab program. This program simulates transmission through a slab of diamond with one rough surface using the transfer matrix method.

```
clear

% enter the nominal thickness of the diamond in meters
dnom=1.0*10^-6;

% let the incident medium be air
n1=1;

% let the final medium also be air
n3=1;

% diamond will be the middle medium, and it's index of refraction
% will need to be calculated with the sellmeier equation on the fly

% set up the weighting scheme

%%%%%%%%%%%%%%%%%%%%%%%%%%%%%%%%

% roughness of film (RMS) aka standard deviation

sigma=10*10^-9;

dstart=dnom-(4*sigma);
dstop=dnom+(4*sigma);

dpp=30;

incrp=(dstop-dstart)/dpp;
nm=0;

for n=1:dpp+1;
    d(n)=dstart+((n-1)*incrp);
    term1=((d(n)-dnom)^2)/(2*(sigma^2));
    dt(n)=exp((-1)*term1);
    nm=nm+dt(n);
end

dt=dt./nm;

hold off

% start the loop to calculate transmission

numpoints=100;

lamstart=1000*10^-9;
```

```
lamstop=1600*10^-9;

incr=(lamstop-lamstart)/numpoints;

for n=1:numpoints;
    lam(n)=lamstart+(n-1)*incr;
    lamu(n)=lam(n)*1e6;
    trm1=(.3306*(lamu(n))^2)/(((lamu(n))^2)-0.175*.175);
    trm2=(4.3356*(lamu(n))^2)/(((lamu(n))^2)-.106*.106);
    n2(n)=sqrt(1+trm1+trm2);

    r1R=(1-n2(n))/(1+n2(n));
    r1L=(n2(n)-1)/(1+n2(n));
    t1R=(2)/(n2(n)+1);
    t1L=(2*n2(n))/(n2(n)+1);

    W12=(1/t1R)*[1 -r1L;r1R t1R*t1L - r1R*r1L];

    r2R=((n2(n)-1)/(1+n2(n)));
    r2L=((1-n2(n))/(1+n2(n)));
    t2R=((2*n2(n))/(n2(n)+1));
    t2L=((2*1)/(n2(n)+1));

    W23=(1/t2R)*[1 -r2L;r2R t2R*t2L - r2R*r2L];

    Tmp(n)=0;

    Tmp2(n)=0;

        for j=1:dpp;

            phiair=(2*pi*n1*(d(dpp)-d(j)))/lam(n);

            U0=[exp(i*phiair) 0;0 exp(-i*phiair)];

            phid=(2*pi*n2(n)*d(j))/lam(n);

            U1=[exp(i*phid) 0;0 exp(-i*phid)];

            S=U0*W12*U1*W23;

            t=1/S(1,1);

            Tmp(n)=Tmp(n)+(dt(j)*t);

        end

   Tr(n)=abs(Tmp(n)*conj(Tmp(n)));

end

figure(1)
plot(lam,Tr,'^-')
xlabel('Wavelength')
ylabel('Transmission')
title('tranmat.m')
```

Appendix B: Sample Data

Below is a table summarizing most of the samples created in the process of this research. Additionally, a series of samples prefixed by "FB" are listed. These samples were deposited as part of a project to create electron spalation foils. The samples are listed here because one of the samples is referenced in Chapter 6 in regards to AFM measurements, while data from other FB samples are used in Chapter 5 as a plot of deposition temperature as a function of deposition pressure.

Name	Deposition Pressure (Torr)	Gas Flows ($H_2/CO_2/CH_4$)	Depostion Time (hours)	Weight Gain (mg)	Substrate Diameter (inches)	Comments
Rogdav01	9	200/0/5	20	14.0	3	0.1μm diamond powder, 53mm quartz ring
Rogdav02	7	200/0/5	20	8.8	3	0.1μm diamond powder, 53mm quartz ring
Rogdav03	7	200/0/5	20	7.2	3	0.1μm diamond powder, 55mm quartz ring
Rogdav04	7	200/0/5	40	21	4	0.1μm diamond powder, 55mm quartz ring
Rogdav05	7	200/0/5	20	9.3	4	0.1μm diamond powder, 55mm quartz ring
Rogdav06	7	200/0/5	20	8.2	4	0.25μm diamond powder, 55mm quartz ring
Rogdav07	7	200/8/3	40	5.9	4	0.1μm diamond powder, 55mm quartz ring
Rogdav08	7	200/0/5	20	13	3	0.25μm diamond powder, 55mm quartz ring

Name	Deposition Pressure (Torr)	Gas Flows ($H_2/CO_2/CH_4$)	Depostion Time (hours)	Weight Gain (mg)	Substrate Diameter (inches)	Comments
Rogdav09	7	200/0/5	20	4.2	3	0.25μm diamond powder, 55mm quartz ring, H_2 plasma pre-treatment for 2 hours.
Rogdav10	7	200/0/5	20		3	0.25μm diamond powder, 55mm quartz ring, sample broken when removed from system
Rogdav11	7	200/0/5	20	8.4	3	0.25μm diamond powder, 55mm quartz ring
Rogdav12	7	200/0/5	20		3	0.25μm diamond powder, 55mm quartz ring, bell jar broken during deposition
Rogdav13	7	200/0/5	20	9	3	0.25μm diamond powder, 55mm quartz ring
Rogdav14	7	200/0/5	20	9.1	3	0.25μm diamond powder, 55mm quartz ring
RB2K-2					2	Diamond on oxide, 59mm quartz ring
RB2K-3		No deposition			2	Fabricated oxide windows, 59mm quartz ring
RB2K-4				4.1	2	59mm quartz ring
RB2K-5	10	200/0/5	15	3.2	2	59mm quartz ring
RB2K-6	35	200/0/5	3	10.9	2	59mm quartz ring
RB2K-7	10	200/0/5	15	3.9	2	59mm quartz ring
RB2K-8	35	200/8/3	5.5	8.7	2	59mm quartz ring
RB2K-9	35	200/8/3	5.5	6.3	2	59mm quartz ring

Name	Deposition Pressure (Torr)	Gas Flows ($H_2/CO_2/CH_4$)	Depostion Time (hours)	Weight Gain (mg)	Substrate Diameter (inches)	Comments
RB2K-10	35	200/8/3	3	3.8	2	59mm quartz ring
RB2K-11	35	200/0/5	3	10.9	2	59mm quartz ring

Table B.1 List of samples created for this research.

Name	Deposition Pressure (Torr)	Gas Flows ($H_2/CO_2/CH_4$)	Depostion Time (hours)	Weight Gain (mg)	Substrate Diameter (inches)	Comments
FB-2	29	200/8/3	6	10.1	3	59mm quartz ring
FB-3	30	200/8/3	6	8.4	2	59mm quartz ring
FB-4	30	200/8/3	3	4.7	3	59mm quartz ring
FB-5	33	200/8/3	6		3	59mm quartz ring
FB-6	34	200/8/3	4	8.5	3	59mm quartz ring
FB-7	35	200/8/3	4.5	9.0	3	59mm quartz ring
FB-8	35	200/8/3	3		2	59mm quartz ring
FB-9	35	200/8/3	3		2	59mm quartz ring
FB-10	33	200/8/3	4		2	59mm quartz ring
FB-11	33	200/8/3	4		2	59mm quartz ring
FB-12	32	200/8/3			2	59mm quartz ring
FB-13	32	200/8/3	3.5		3	59mm quartz ring
FB-14	33	200/8/3	4			59mm quartz ring
FB-15	33	200/8/3	4			59mm quartz ring
FB-16	33	200/8/3	6			59mm quartz ring
FB-17	33	200/8/3	6			59mm quartz ring
FB-18	33	200/8/3	5			59mm quartz ring
FB-19	33	200/8/3	5			59mm quartz ring
FB-20	30	200/8/3	5			59mm quartz ring
FB-21	30	200/8/3	5.5			59mm quartz ring
FB-22	30	200/8/3	5			59mm quartz ring
FB-23	33	200/8/3	7			59mm quartz ring
FB-24	33	200/8/3	7			59mm quartz ring
FB-25	29	200/8/3	7			59mm quartz ring
FB-26	20	200/8/3	12		2	59mm quartz ring

Name	Deposition Pressure (Torr)	Gas Flows ($H_2/CO_2/CH_4$)	Depostion Time (hours)	Weight Gain (mg)	Substrate Diameter (inches)	Comments
FB-27	20	200/8/3	16		3	59mm quartz ring
FB-28	20	200/8/3	26		3	59mm quartz ring
FB-29	6	200/8/3	48		3	59mm quartz ring

Table B.2 List of FB samples.

Appendix C: Additional Measurements

This appendix contains the optical transmission measurements made on the various samples for this research that were not included in Chapter 5.

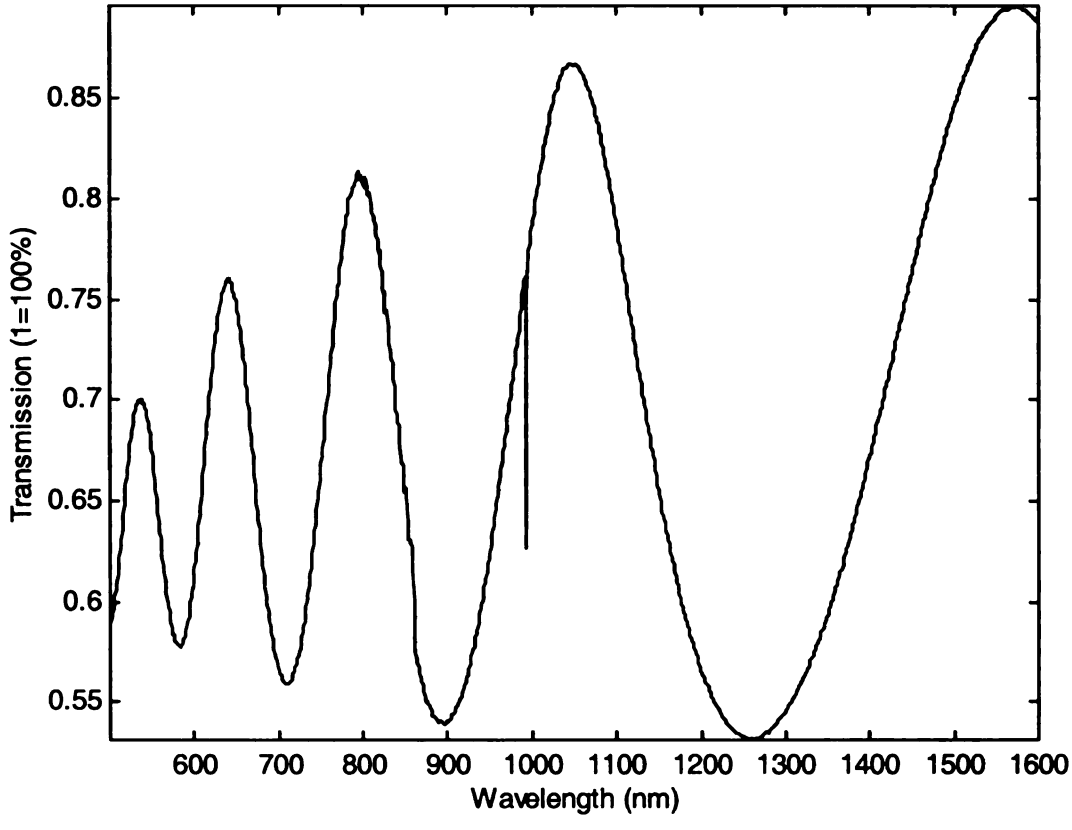

Figure C.1 Diamond window on the RB2K9 wafer measured with Perkin-Elmer UV-Vis system. 0.66μm thickness.

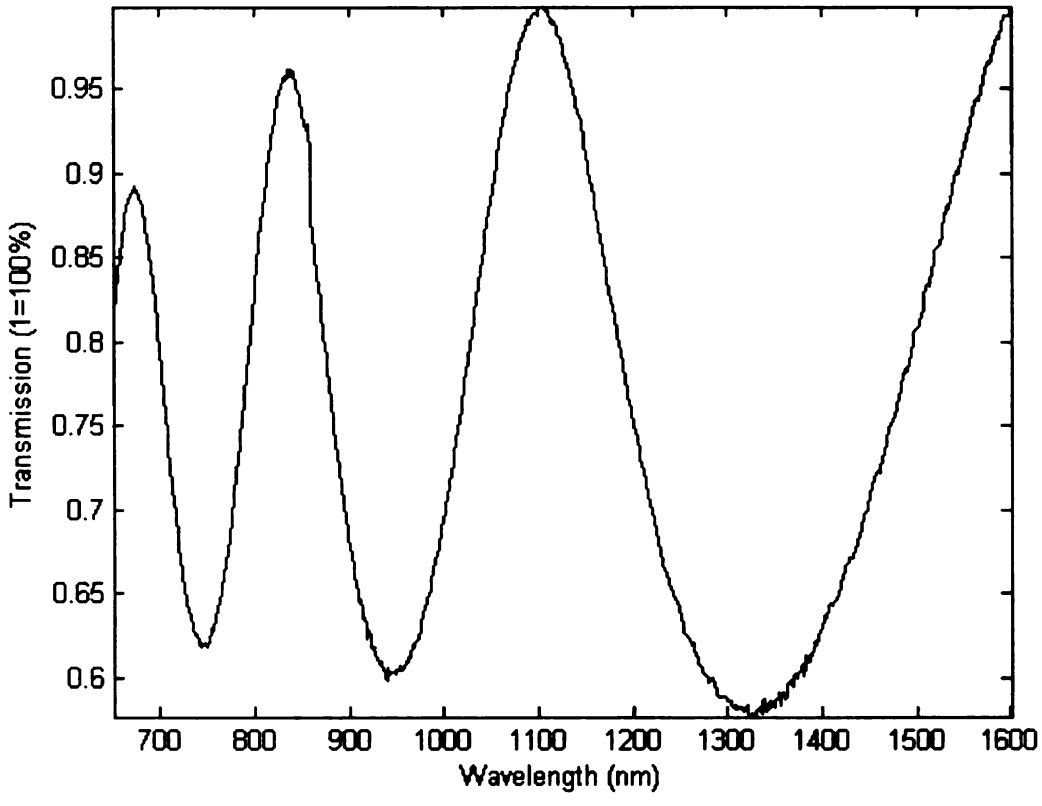

Figure C.2 Diamond window on RB2K9 measured with Perkin-Elmer UV-Vis system. 0.695μm thickness.

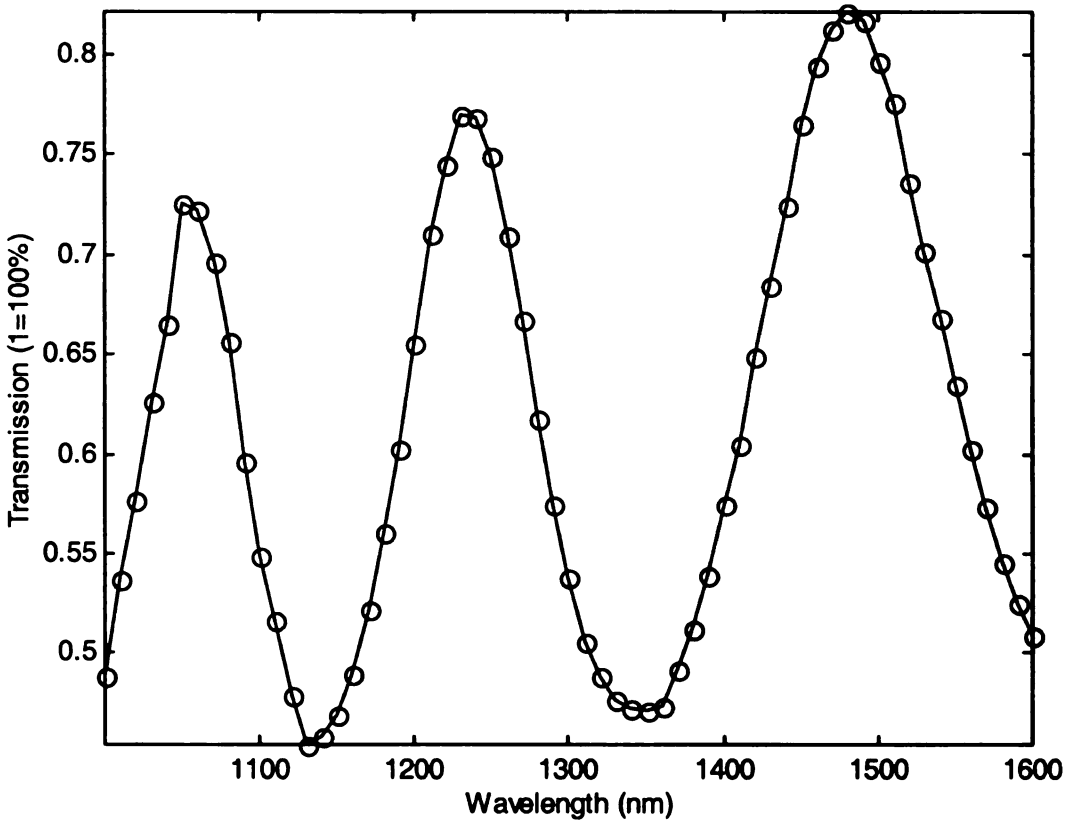

Figure C.3 Diamond window on RB2K8 measured with Bausch & Lomb system. Approximate thickness 1.55μm.

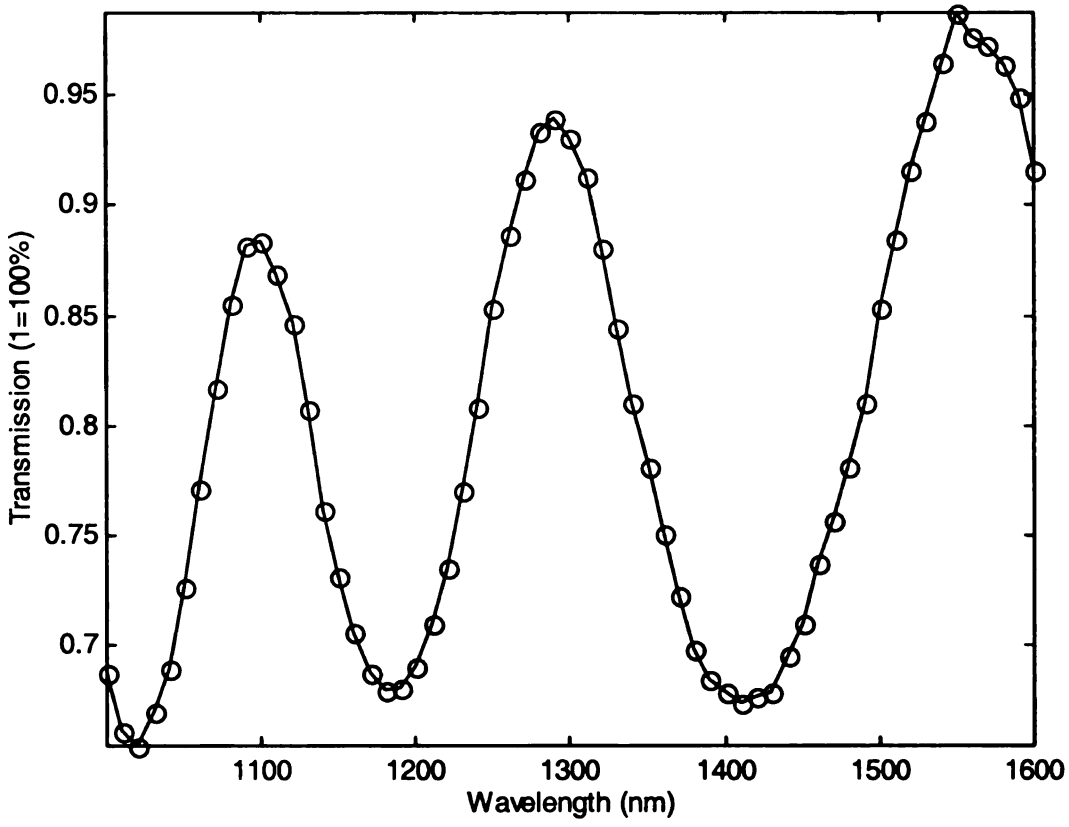

Figure C.4 Diamond window on RB2K8 measured with Bausch & Lomb system. Approximate thickness 1.62μm.

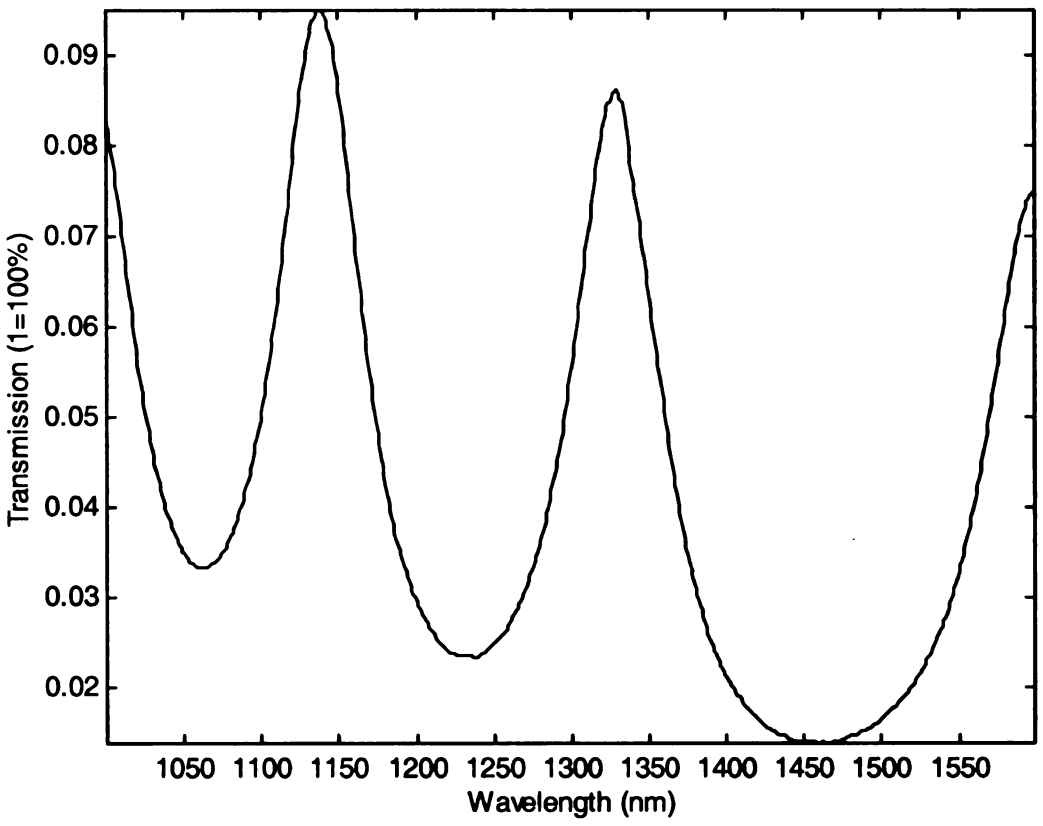

Figure C.5 FP Cavity on RB2K8 as measured with Perkin-Elmer UV-Vis system. Diamond film is 1.59μm thick, with 12nm and 20nm gold coatings.

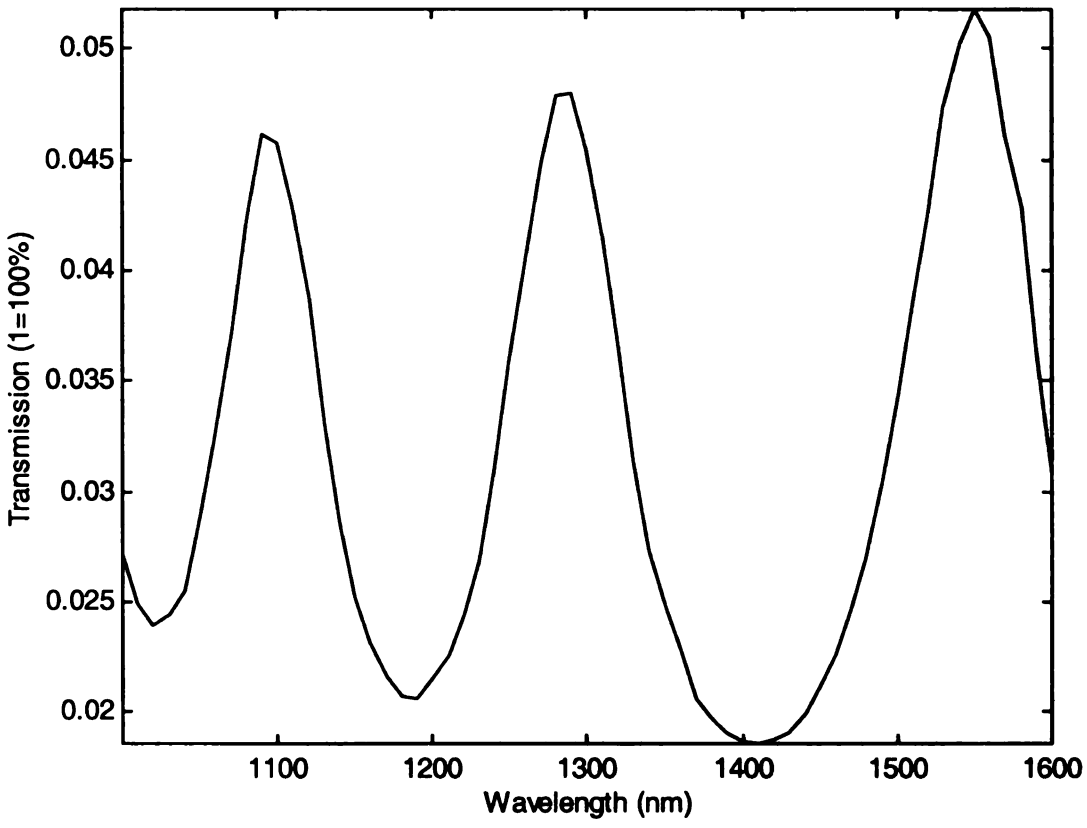

Figure C.6 FP Cavity on RB2K8 as measured with Perkin-Elmer UV-Vis system. Diamond film is 1.55μm thick, with 12nm and 25nm gold coatings.

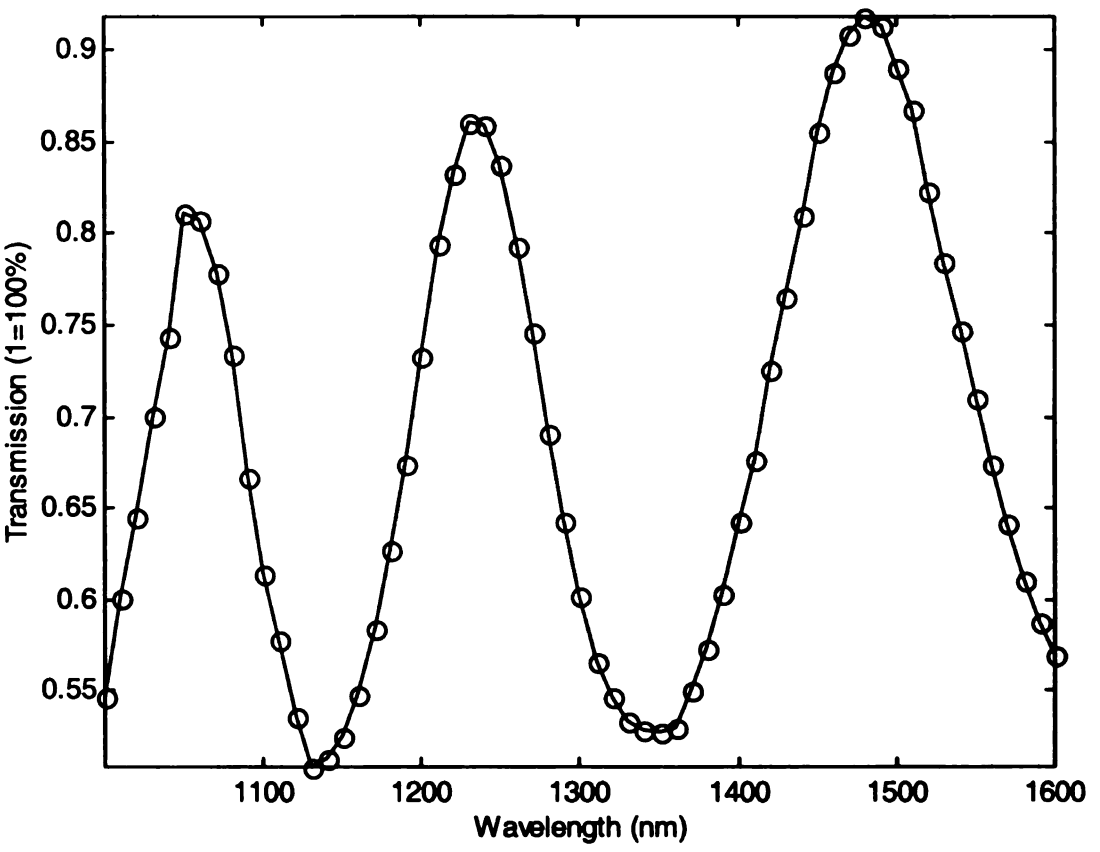

Figure C.7 Diamond window on RB2K8 measured with Bausch & Lomb system. Approximate thickness 1.55μm.

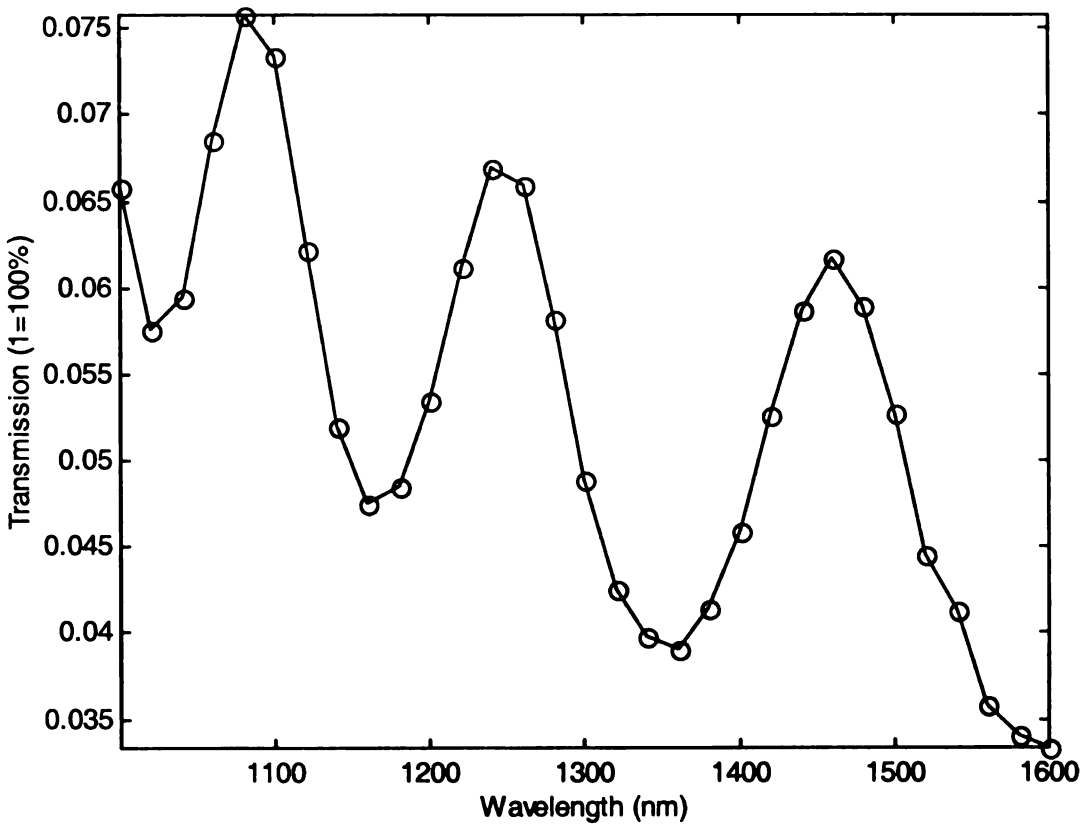

Figure C.8 FP Cavity on RB2K8 measured with Bausch & Lomb system. Approximate diamond thickness 1.75mm. Gold coatings approximately 12nm and 25nm thick.

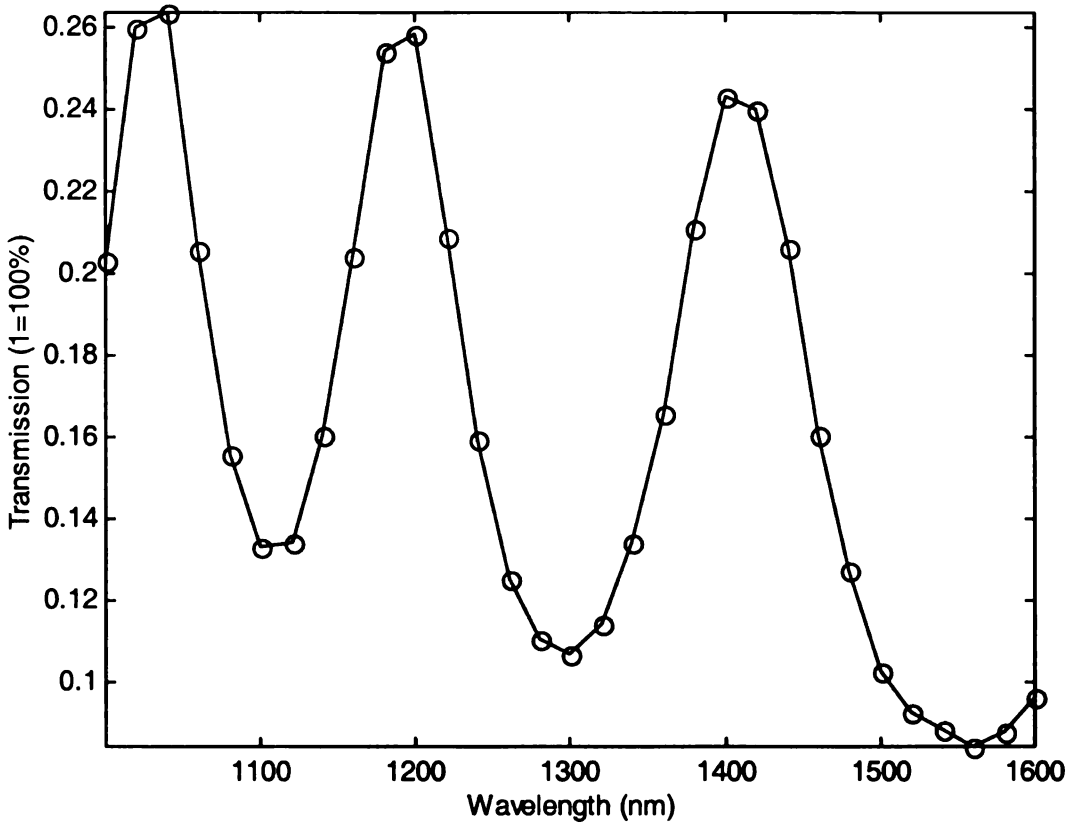

Figure C.9 FP Cavity on RB2K8 measured with Bausch & Lomb system. Approximate diamond thickness 1.57mm. Gold coatings approximately 0nm and 15nm thick.